EDGEWOOD
CHEMICAL BIOLOGICAL CENTER
U.S. ARMY SOLDIER AND BIOLOGICAL CHEMICAL COMMAND

ECBC-CR-047

FREQUENCY AGILE LASER AND CHEMICAL SENSOR

David B. Cohn
Louis F. Klaras
John R. Becker
Hans C. Marciniak

HUGHES AIRCRAFT COMPANY
El Segundo, CA 90245

August 2001

Aberdeen Proving Ground, MD 21010-5424

20011231 147

Disclaimer

The findings in this report are not to be construed as an official Department of the Army position unless so designated by other authorizing documents.

REPORT DOCUMENTATION PAGE

1. AGENCY USE ONLY (Leave blank)	2. REPORT DATE 2001 August	3. REPORT TYPE AND DATES COVERED Final; 90 Aug - 96 Jul

4. TITLE AND SUBTITLE Frequency Agile Laser and Chemical Sensor	5. FUNDING NUMBERS C-DAAA15-90-C-0024

6. AUTHORS
Cohn, David B. ; Klaras, Louis F. ; Becker, John R. ; and Marciniak, Hans C.

7. PERFORMING ORGANIZATION NAME(S) AND ADDRESS(ES) Hughes Aircraft Company, El Segundo, CA 90245	8. PERFORMING ORGANIZATION REPORT NUMBER ECBC-CR-047

9. SPONSORING/MONITORING AGENCY NAME(S) AND ADDRESS(ES) DIR, ECBC,* ATTN: AMSSB-RRT-DL, APG , MD 21010-5424	10. SPONSORING/MONITORING AGENCY REPORT NUMBER

11. SUPPLEMENTARY NOTES
COR: Cynthia R. Swim, AMSSB-RRT-DL, (410) 436-6630
*When this work was conducted, the U.S. Army Edgewood Chemical Biological Center (ECBC) was known as the
  U.S. Army Edgewood Research, Development and Engineering Center (ERDEC).

12a. DISTRIBUTION/AVAILABILITY STATEMENT Approved for public release, distribution is unlimited.	12b. DISTRIBUTION CODE

13. ABSTRACT (Maximum 200 words)

A compact, wavelength agile CO_2 TEA laser and sensor have been developed for remote chemical detection. The laser is computer-controlled, sealed with an internal catalyst, and has a maximum firing and wavelength shift rate of 200 Hz with 40% duty cycle. The wavelength shifter operates in repeating patterns and can access any of 60 lines in any order. Multimode output energy exceeds 125 mJ for all lines and the pulse is composed of a 120 nsec wide spike, followed by a 1.5 µsec tail that can be eliminated by an electro-optical modulator. Environmental testing was successful under a 3 G shock, 2 G sine wave vibration and a 0-40☐Gtemperature range. An operational lifetime exceeding 50 million shots was demonstrated with tests terminated by the operator, not by malfunction. The fully integrated laser weighs 100 lb, occupies 3 ft³, and requires a source of 28 VDC to operate. The laser was integrated with a sensor and was successful in three separate field trials. Measurements of canvas target reflectivity over the spectral range 9.3-10.7 µm were within 15% of the calibrated values, normalized signal percentage standard deviation was 1-2% for a 16 pulse average, measurement of atmospheric water vapor was within the accuracy of meteorological instruments, and concentration-path length measurements with a vapor cell were in agreement with calibrated values.

14. SUBJECT TERMS Remote detection Differential absorption LIDAR (DIAL) Infrared (IR) LIDAR Transversely Excited Atmospheric (TEA) laser Differential scatter (DISC) Carbon dioxide (CO_2) laser	15. NUMBER OF PAGES 139
	16. PRICE CODE

17. SECURITY CLASSIFICATION OF REPORT **UNCLASSIFIED**	18. SECURITY CLASSIFICATION OF THIS PAGE **UNCLASSIFIED**	19. SECURITY CLASSIFICATION OF ABSTRACT **UNCLASSIFIED**	20. LIMITATION OF ABSTRACT **UL**

Blank

PREFACE

The work described in this report was authorized under Contract No. DAAA15-90-C-0024. This work was started in August 1990 and completed in July 1996.

This report covers technical efforts, including design considerations; details of the mechanical, optical, and electronic components; details of test procedures and results; the hardware and software modifications that resulted from testing; and recommendations for further development. This report is in sufficient detail that it can be used as a guide for operation and diagnosis of the equipment.

In developing the equipment described in this report, numerous commercially available items were used. The use of either trade or manufacturers' names in this report does not constitute an official endorsement of any commercial products. This report may not be cited for purposes of advertisement.

This report has been approved for public release. Registered users should request additional copies from the Defense Technical Information Center; unregistered users should direct such requests to the National Technical Information Service.

Acknowledgments

CONTENTS

FIGURES

TABLES

Blank

ABBREVIATIONS AND ACRONYMS

A-D	Analog to digital
AES	Auger electron spectroscopy
AR	Antireflection
BS	Beam splitter
CBDC	Chemical and Biological Defense Command
CCD	Charge-coupled-device
CdTe	Cadmium Telluride crystal
DAC	Digital to analog converter
DIAL	Differential Absorption Lidar
DISC	Differential Scattering
DMC	Digital motion controller
EMI	Electromagnetic interference
ESCA	Electron spectroscopy for chemical analysis
FAL	Frequency Agile Laser
FOV	Field of view
Ge	Germanium
GPIB	General purpose interface bus, IEEE 488
HeNe	Helium Neon
HgCdTe	Mercury Cadmium Telluride
IR	Infrared
IR&D	Independent Research and Development
KRS-5	Thallium bromoiodide
LN_2	Liquid nitrogen
ND	Neutral density
PC	Personal computer
PC HgCdTe	Photoconductive Mercury Cadmium Telluride
PV HgCdTe	Photovoltaic Mercury Cadmium Telluride
Q.E.	Quantum efficiency
RAM	Random access memory
RS-232	Recommended standard, Electronics Industry Association
SCSI	Small computer system interface
Si	Silicon
TE	Thermoelectric
TEA	Transversely Excited Atmospheric
TEP	Triethylene phosphate
TV	Television
UPS	Uninterruptible power supply
ZnSe	Zinc Selenide

Blank

FREQUENCY AGILE LASER AND CHEMICAL SENSOR

1. SUMMARY

A prototype sealed, frequency agile laser (FAL) and testbed sensor have been developed for remote detection of chemicals by the differential absorption lidar (DIAL) and differential scattering (DISC) techniques. They are pictured in Figure 1. The laser is a computer-controlled, sealed, transversely excited atmospheric (TEA) CO_2 device with internal catalyst and transverse gas flow that operates at a maximum firing and wavelength shift rate of 200 Hz with 40% duty cycle. The wavelength shifter, composed of a fixed grating and galvanometer-mounted mirror, operates in repeating patterns with access to 60 lines in the CO_2 spectrum in any order. The shifter can store 15 patterns of 20 wavelengths each which are easily selected and modified by the operator through the computer. The laser multi-mode output energy exceeds 125 mJ for all lines (including the 9P44 line in particular). On strong lines, the multi-mode output energy is typically 250 mJ. The output pulse is composed of a 120 nsec wide gain-switched spike, followed by a 1.5 μsec tail. A tailchopper, developed for range-resolved aerosol measurements, is composed of an extra-cavity CdTe crystal (operating on the transverse electrooptic effect) and polarization analyzer combination. The fully integrated laser, including high voltage power supply, weighs 100 lb, and requires only a source of 28 Vdc and serial computer link to operate. No other support equipment is required.

(a)   (b)
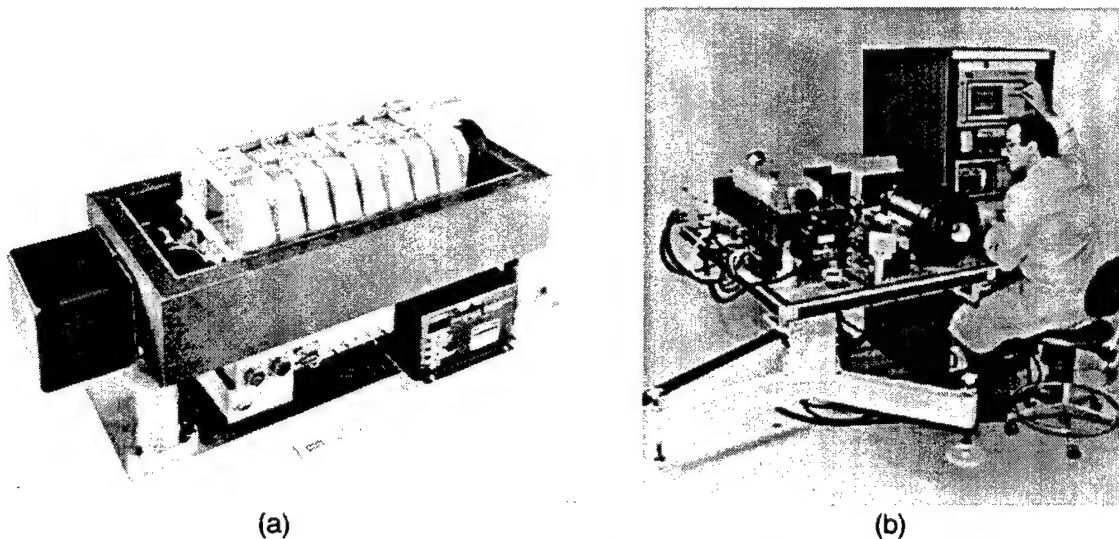
Figure 0-1. (a) Frequency Agile Laser and (b) chemical sensor.

The laser underwent environmental testing which included operational testing before and after the application of a 3 G shock, a 2 G sine wave vibration, and thermal cycling over a 0-40 °C temperature range. The sine wave vibration was particularly severe with excursions of several centimeters from 5 to 500 Hz. The thermal test involved full laser characterization at three test temperatures during thermal cycling. A firing lifetime exceeding 50 million shots was demonstrated with tests terminated by the operator, not by malfunction. Several critical components, including the discharge module, fan assembly, electronics, high voltage section, and wavelength shifter were further tested without failure to 80 million shots. The output coupler

and Brewster window optics were found to damage early in the lifetest, but subsequent redesign eliminated this failure mode. Therefore, life limiting mechanisms are not known and it is likely that the 10^8 shot design goal is achievable.

The sensor was developed primarily as a testbed for demonstrating chemical detection in the field with the high repetition rate FAL transmitter. In that respect, the design was guided by the need for easily modified components that were readily available and presented low schedule and technical risk. The design approach, therefore, did not favor size and weight reduction in relation to functionality and reliability, although efforts were made to produce as compact a system as possible. The resulting sensor is composed of a 40 in. x 44 in. aluminum optical table to which the laser and all sensor components are attached. The major optical components are the 10 in. diam Cassegrain telescope and the spectrum analyzer used to check laser output. The detection system is composed of a thermo-electrically-cooled, HgCdTe transmit waveform detector and a liquid nitrogen-cooled, HgCdTe receive pulse detector. The optical table is attached to a gimbal that allows for pointing in azimuth and elevation to an accuracy of 0.01 deg. The sensor without the gimbal attached weighs about 250 lb. The sensor is supported by a data acquisition system housed in a rack that uses an analog-digital (A-D) converter with 12 bit accuracy and 30 MHz sampling rate.

Several tests were performed to establish sensor performance. In order to qualify the sensor alignment and the transmit and receive optical trains, an absolute spectral reflectivity test was conducted with a calibrated canvas target at a range of 600 m. It was found that the sensor data were within 20% of the calibrated target reflectivity values over the wavelength range 9.2-10.7 μm. The short term sensor noise level was investigated by measuring the percentage standard deviation of normalized return signals. It was found that after a 16 pulse average, the percentage deviation was 1-2%. The test procedure also included measurement of atmospheric water vapor and comparison with local meteorological data. Typically, values of water vapor content measured with the sensor were on the order of 5 mbar and were within 10% of values determined from measurements of temperature and relative humidity.

The sensor participated in three field trials over the five year period of the program. Throughout field testing the sensor proved to be simple to set up. From a crated condition, it typically takes only two hours from uncrating through assembly and installation in the van, to the point where data can be acquired. A very important contributing factor to this ease of use was the fact that no laser adjustment nor sensor optical realignment were required after transportation or storage. The sensor participated in 100% of the tests. Typically, a four week test period resulted in several million laser firings and collection of about 1 GB of data using a digital oscilloscope or about 5 GB of data using a digitizer card. Although the number of data runs and the resulting amount of data was prodigious, the sensor was easily operated by one person. The task of data analysis was undertaken by personnel of the U.S. Army Chemical and Biological Defense Command (CBDC) and will be available in agency reports and professional journals.

Several recommendations for improvement of the system have resulted from the field experience. The laser uses an air-cooled heat exchanger which is difficult to construct and is prone to vacuum leaks. It requires the use of a high speed fan for cooling which produces high frequency noise. For these reasons, a water cooled heat exchanger is suggested. Furthermore, a

reduction in the size and weight of the laser and sensor have been sought. Significant initial reductions can be achieved with modest effort having to do with removal of a laser total energy meter and spectrum analyzer to an auxiliary table and the rearrangement of the remaining optical components. In the area of functionality, modifications to the wavelength shifter mechanism and its control software are required. This would involve primarily development of a non-resonant galvanometer as opposed to the pseudo-resonant device presently in use. Furthermore, certain software modifications have been suggested to further automate sensor setup and data acquisition which would involve integration of disparate segments of code developed independently to operate the wavelength shifter, gimbal, and A-D card. Finally, sensor set up can be made more straightforward by redesigning the power and signal cable sets.

Blank

2. INTRODUCTION

The detection and quantification of chemicals in clouds by the techniques of differential absorption lidar (DIAL) and differential scattering (DISC) have been well established. In that prior work, the high pressure, pulsed CO_2 laser has proven most useful. The impetus for the work reported here arose out of the need to reduce size and weight and increase the effectiveness of conventional remote chemical sensors that had employed multiple, low energy CO_2 lasers operating at relatively low repetition rates, on the order of 10 Hz. Certain operational requirements related to fast moving platforms or moving and dispersing targets dictated a significant increase in data rates and output energy to 200 Hz and 100 mJ, respectively; and with the capability of shifting wavelengths at high rates. In addition to enhancing laser output characteristics, it was also found necessary to significantly advance the state-of-the-art in high repetition rate laser reliability and operational lifetime while maintaining an integrated and compact device. These needs for increased capability led to the specifications for the FAL and to the testbed sensor which was developed to prove the effectiveness of the transmitter and the data acquisition approach.

The objectives of the FAL program were to develop three prototype lasers, to perform extensive life and operational tests on one of them, and to develop a sensor testbed integrated with one laser. It was also required that the lasers and sensor meet certain environmental specifications that would guarantee operational capability under field conditions without undue operator intervention. The resulting FAL program dealt with the laser prototype and sensor proof-of-principle phases of development. Development of the laser beyond the prototype level and development of a prototype sensor will necessarily be undertaken in a subsequent program.

This report includes details of laser and sensor component design, fabrication, and testing, as well as comments on design tradeoffs for certain critical components. In that respect, the areas that received special attention are the laser gas catalyst, optics, and pulsed power. Also included are details of the extensive efforts in system-level testing of the laser and the sensor in the laboratory and in the field. Recommendations are included for improving the laser and sensor as a consequence of the multiple field test sessions. This document was intended not only to report the results of device development but to also serve as a user's manual. To that extent it includes details for aligning, setting up, and operating the laser and sensor and for performing diagnostic tests.

The body of the report begins with Section 3 which contains details of laser development. This includes in subsection 3.1 a description of the laser, a comparison of the laser requirements and performance, and details of subsystems and components. At the subsystem level are the pressure vessel and gas flow system, pulsed power and discharge module, electronics, optics, wavelength selector, tailchopper, and catalyst. The final section of laser development contains the laser operating procedure which integrates the steps of laser turn-on, operation, and turn-off. Subsection 3.2 of laser development contains a detailed description of the laser test effort. This includes the test approach and diagnostics followed by results of the qualification test, the environmental test, and the life test. Section 4 of the report on sensor

5

development parallels the presentation approach used in the description of laser development. Subsection 4.1 contains the sensor description including the optics, detection, electronics, and data acquisition subsystems, as well as a description of the alignment procedure. The subsection closes with a description of the sensor operating procedure. Subsection 4.2 contains the results of the sensor calibration and field testing efforts. The report concludes with the major technical findings in Section 5 and recommendations for improvement in Section 6.

3. LASER DEVELOPMENT

Development of the FAL was based on a proof-of-concept model that was built and tested under a Hughes IR&D effort. As a result of that effort, key operating parameters were established prior to the FAL design. These included discharge volume, gas mixture and pressure, input and output energy, pulse temporal profile, catalyst operation, and initial specifications of several critical components. However, it was found that in order to meet the program requirements of reliability and lifetime, it was necessary that the FAL design depart significantly from that of the IR&D model. Therefore, the FAL program contained parallel efforts in component development and design verification in addition to the baseline tasks of laser fabrication and testing. In that respect, important modifications were made to the design in the course of the program, primarily in the areas of optics and pulsed power.

The three major subsections that follow deal with (1) development of the laser and components; (2) a description of the qualification, environmental, and life testing; and (3) the operating procedure that developed from the qualification testing and experience in the field. Laser field test results are discussed in Section 4.2.2 dealing with the parallel activity of sensor field testing.

3.1 LASER DESCRIPTION

This section contains first a summary of the FAL characteristics and a description of its subsystems. In the main body of the section, the major components are described in detail, including the implications of environmental and lifetesting on their designs. Laser performance parameters and the results of testing the fully integrated laser are contained in Section 3.2.

3.1.1 Introduction

The FAL is of the Transversely Excited Atmospheric (TEA) type, wherein the high speed gas flow direction, the optical axis, and the discharge electric field are orthogonal. The laser discharge is defined by two opposing electrodes of small width to length ratio; and the gas is excited by a fast, high current discharge. For operation at high pulse repetition rates from about 3 to 200 Hz, it is necessary after each discharge to remove the gas from the inter-electrode region prior to the next pulse in order to avoid arcing. This is accomplished by a tangential fan which circulates the gas at high speed through the electrode region and also moves it through a parallel heat exchanger and catalyst module. The internal catalyst module is required to reconstitute the CO_2 decomposed in the discharge process. The optical mode cross-section is defined by the discharge height and width which in the case of the FAL is a 1 cm square. The output temporal profile is a typical gain-switched spike of about 200 nsec duration, followed by a 1-2 μsec long, low intensity tail. For certain applications involving range-resolved measurements with aerosols, it is necessary to eliminate the tail and this is accomplished with a transverse, electrooptic amplitude modulator composed of CdTe crystals and a Brewster plate polarizer. Finally,

wavelength shifting of the laser output is accomplished at all pulse repetition rates up to 200 Hz with a module composed of a fixed grating and a mirror attached to a galvanometer. The wavelength shifter also provides all laser firing timing pulses and interfaces to a computer from which wavelength patterns and firing rates are established and downloaded.

A photograph of the integrated FAL is shown in Figure 3-1. Note the 15 cm long scale. The ribbed structure at the top is the section of the pressure vessel housing the air-cooled heat exchanger, catalyst module, and internal fan. Surrounding this section of the vessel is a rectangular graphite-epoxy composite optical bench to which are attached the wavelength shifter and the output coupler assembly. These components are optically coupled through Brewster windows attached to the vessel. Beneath the optical bench and pressure vessel are located the fire control electronics and high voltage power supply. The laser is sealed and completely self contained as shown and requires only a source of 28 Vdc and an RS-232 link to the computer to operate. A schematic view of the FAL is shown in Figure 3-2 for orientation.
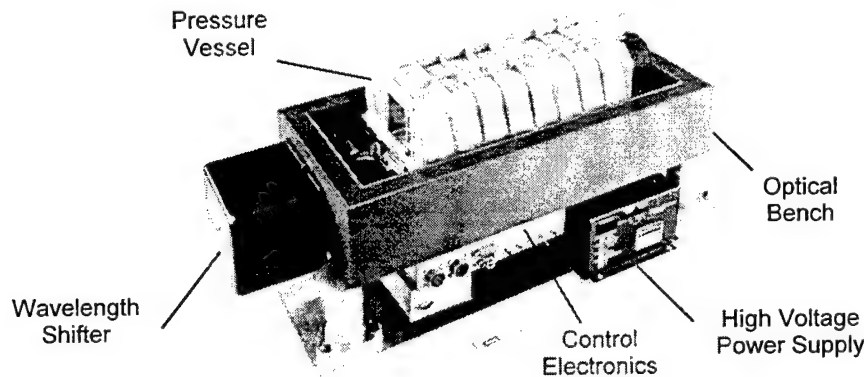
Figure 3-1. Integrated FAL.
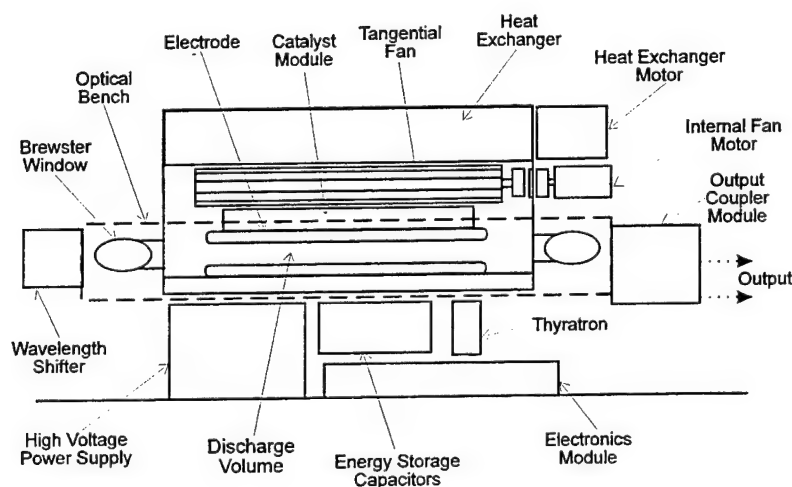
Figure 3-2. FAL schematic view.

8

The various subassemblies described above are each composed of several components. For purposes of organizing the discussion, the subassemblies, their components, and the section in which they are discussed are shown in Table 3-1.

Table 3-1. Laser subassemblies and components.

Subassembly	Component/Topic	Section
Pressure Vessel	-Chamber -Discharge module/top -Fan and bearings -Heat exchanger	3.1.2
High Voltage Section	-Capacitors -Switch -Power supply	3.1.3
Electronics	-Laser fire control module -Power supply module -Interfaces	3.1.4
Optics	-Bench -Brewster windows -Output coupler -Intracavity expander -Optical damage	3.1.5
Wavelength Shifter	-Alignment -Software -Menus -Operating procedure	3.1.6
Tailchopper	-Crystals and holders -Pulser -Test results	3.1.7
Catalyst	-Test procedure -Activation -Test results	3.1.8

The objective of the FAL program was to meet a number of physical constraints and functional requirements. These program requirements and the achieved FAL values are shown in Table 3-2.

It can be seen that the FAL achieved all functional requirements and some with margin. In particular, the output energy on all lines exceeded the requirement. In addition, it was found that the laser could access additional weak lines beyond the required limits down to rotational J values of 4-6 and up to J values of 44 for the four bands. The firing lifetime was achieved in tests that showed no failure to 53 million shots for the integrated laser and to 80 million shots for several critical components. Optics were found to damage early in the lifetest; however, redesign of these components have shown that damage can been eliminated. Therefore, life limiting mechanisms are not known and it is likely that the 10^8 shot design point is achievable. These points are discussed in Sections 3.1.5 and 3.2.5.

The pulse shape requirement was addressed in the design through use of the tailchopper. A device using two CdTe crystals has shown about a 10 dB reduction in the tail; whereas, a three crystal device has shown about 20 dB attenuation. The latter level is at the limit of the dynamic range of the instrumentation.

Table 3-2. Program requirements and FAL performance.

Characteristic	Requirement	FAL	Comments
Lifetime	Design for 10^8 shots Test to 5×10^7 shots	Yes	Optics failure in lifetest-eliminated in redesign, no other failures noted
Output Energy	>100 mJ, all lines	Yes	$\geq$115 mJ at 40 ^{o}C $\geq$140 mJ at 25 ^{o}C
Pulselength	70% energy in 250 nsec, Tail=60 dB down at 1 μsec	70% energy in 250 nsec, Tail=20 dB down at 1 μsec	3 crystal chopper 20 dB limit of diagnostic resolution
Wavelength Tuning	1-16 lines at 200 Hz rate, 40 % duty cycle	Yes	1-20 lines possible
	55 lines: 9P10-9P44, 9R10-9R30, 10P8-10P32, 10R8-10R32	>65 lines	All bands range J (6-38), Galvo span limits 9R and 10P max
Transverse Modes	>3 modes	10	Inferred from divergence
	<15% spatial energy distribution variation in far field	Yes	Inferred from infrared camera measurements
Temp Range	0 ^{o}C to 40 ^{o}C	Yes	Operating
Start-up Time	<20 min.	Yes	
Input Voltage	28 Vdc $\pm$20%	Yes	
Power Supplies	Provide 28 Vdc	Yes	
Input Power	< 1 kW	560 W	Standard burst mode
Vibration	$\pm$2 G, 5-500 Hz, 3 axes	Yes	Non operating
Shock	3 $\pm$ 0.3 G, 11 $\pm$1.1 msec half sine, 3 axes	Yes	Non operating
Size	<2 ft^3	3 ft^3	Height increase due to modified capacitors
Weight	<50 lb	100 lb	See Table 3-3
Sealing	Hard seals	Yes	Original design all hard seals, NaCl Brewster window mod not hard sealed
Pulse Forming Network	Modular, easy to replace	Yes	
Shelf Life	$\geq$ 1 year	Unknown	Tested to 6 mo., no limiting effects known
Interlock	Provide room interlock	Yes	
Failsafe	Avoid charge storage when in standby	Yes	
Alarm	Muted sound/lights at capacitor bank charge	Yes	Connection supplied, alarms user-supplied

The size and weight requirements were not met. This was due to modifications to several components that were not foreseen at the beginning of the program and that were later dictated by the need to meet lifetime or functional requirements and to minimize cost. In that respect, the components of most importance are the high voltage power supply, energy storage capacitors, electronics packaging, and laser alignment and support hardware.

The laser component weights are shown in Table 3-3 with an estimate of the savings in weight if straightforward design changes are implemented. These changes involve no technical risk and could be made through common design practices. However, initial studies have shown that more advanced modifications involving use of different materials and designs could reduce total weight to 30-40 lb. Such advanced approaches would include redesigning the pressure vessel to serve as the optical bench, thereby eliminating the bench; use of stiff, lightweight composite materials for the pressure vessel and all structural members now made of aluminum; elimination of the Brewster window assemblies and hermetically sealing the intracavity beam expander and wavelength shifter with the pressure vessel; and general parts reduction by use of integrated modules. These advanced approaches involve technical risk and would require validation in laser functional and environmental testing before final design.

In addition to weight reduction, conceptual approaches to reducing the size of the laser have also been formulated. These include eliminating the independent vessel and bench supports, reconfiguring the capacitor bank, development of a compact wavelength shifter, and electronics miniaturization. All of these approaches are of relatively low risk. The net reduction in size is estimated to be 30% giving a total laser volume of about 2 ft^3.

Table 3-3. FAL component weight and weight reduction approaches.

Component	Current Weight (lb)	Reduced Weight (lb)	Low Risk Weight Reduction Approach
Top/disch module	16.4	12	Machine lightening cutouts
Pressure vessel -Catalyst module -Fan and coupler -Heat exchanger -Windows	17.8	14	Machine lightening cutouts
Ext heat exch motor	1.8	0	Use water cooling
Internal fan motor	2.2	2.2	
Capacitors	10.2	8	Selective potting
Power supply	17.6	10	Lighten power bus and transformer case
Thyratron	0.4	0.4	
Electronics	8.4	4	Lightweight enclosure custom power supplies
Supports	5.7	3	Machining lightening cutouts
Base plate	6.2	0	Eliminate, attach laser directly to optical table
Optical bench	5.6	4	Reduce material
Intracavity expander	3.6	2.5	Reduce material
Wavelength shifter	4.3	4.3	
Total	100.2	64.4	

3.1.2 Pressure Vessel and Gas Flow

This section describes the pressure vessel, its internal components, and the gas flow system. The discharge module and pulsed power elements are discussed in Section 3.1.3.

A cross-sectional view of the pressure vessel is shown in Figure 3-3. In operation, the tangential fan circulates the laser gas across the electrodes and through the catalyst module and heat exchanger. Flow velocity is determined primarily by the need to flush the electrode region of discharge products between firings. The pressure vessel and gas system design and operating parameters are summarized in Table 3-4.
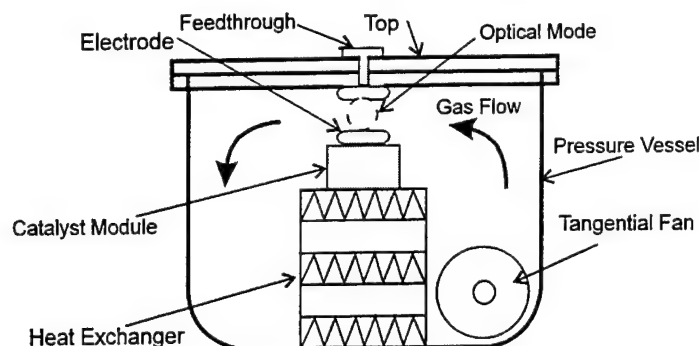
Figure 3-3. Pressure vessel cross-section schematic.

Table 3-4. Pressure vessel and gas system characteristics.

Characteristic	Value
Laser gas mixture	$He/N_2/CO_2=3/1/1$
Laser gas pressure	1 atm
Laser gas volume	7 liters
Discharge flow velocity	10 m/sec
Discharge flush factor (200 Hz, 1.7 cm discharge)	3
Tangential fan speed	5,000 rpm
Heat exchanger fan speed	20,000 rpm
Maximum catalyst temperature	100 $^{\circ}$C
Catalyst volume	<200 cm^3
Catalyst volumetric flow rate	10% of total

The pressure vessel is composed basically of two sections. These are (1) the top, to which is attached the discharge module, and (2) the large volume bottom section that houses the heat exchanger, catalyst module, and tangential fan. Additional components that comprise the bottom of the pressure vessel, and are mounted external to it, include the heat exchanger fan and tangential fan motor. The relative orientation of these components is shown more clearly in Figure 3-2. Finally, optical access through the ends of the pressure vessel is made through Brewster windows, discussed more fully in Section 3.1.5.

The top and bottom sections of the pressure vessel are joined along the edge of a rectangular perimeter that is sealed with a metal gasket. Similarly, the high voltage feedthrough and tangential fan magnetic coupler are also sealed to the vessel with metal gaskets. In the case where ZnSe Brewster windows were used, these were either fritted to their flanges or attached directly with O-ring seals for preliminary testing. In the case of NaCl windows, O-rings were used. Therefore, aside from the case of NaCl windows, the FAL was entirely sealed with metal. This

approach was taken to achieve a greater than one year shelf life while providing for ease of assembly and access to the laser internal systems in the process of development.

The heat exchanger was made integral with the bottom section of the pressure vessel and is of the cross-flow type. The laser gas flows through several plates in the form of a fin structure composed of low pressure drop corrugations. These plates are alternated with similar plates that allow for external air flow at right angles to the laser gas flow direction. The two series of plates exchange heat through thin walls that form the vacuum seal. An external fan, rotating at 20,000 rpm, drives cooling air over the heat exchanger external fins. Thermal control with this system is such that the laser can operate over an ambient temperature range of 0 °C to 40 °C as discussed in Section 3.2.4.

The catalyst module extends the full length of the discharge electrodes and has a volume sufficient to hold 200 cm^3 of catalyst, although 100 cm^3 was typically used. The module incorporated an upstream wire heater that preheated the gas flow into it, thereby heating the catalyst itself. In this way, the catalyst temperature could be regulated up to 100 °C. It was found that a catalyst heater was necessary to elevate the catalyst temperature to achieve adequate activity prior to operation of the discharge. After the start of high repetition rate discharges, the catalyst heater was still necessary to maintain temperature, but at reduced power. The catalyst bed effectiveness was determined also by gas flow velocity through it and this flow was regulated by the relative pressure drop through the parallel catalyst bed and heat exchanger. Gas flow through the catalyst was approximately 10% of the total flow volume.

3.1.3 Pulsed Power and Discharge

The discharge module and pulsed power system shown in Figure 3-4 were designed as integrated units in order to minimize circuit inductance and electromagnetic interference effects. This also allowed for development and testing of the assembly in various test chambers where discharge uniformity and the effects of CO_2 decomposition could be observed.

Figure 3-4. Pulsed power system.

The discharge module is composed of the electrodes that define the high current discharge, preionization discharge elements, high voltage holdoff ceramics, and alignment

fixtures. The module was fabricated as a mechanically independent unit that attached to the top of the pressure vessel. In this way, possible thermal distortions of the pressure vessel were prevented from misaligning the electrodes or imposing stress on the ceramics. Electrode alignment tolerance was 0.001 in. over their 25 cm length. The preionization discharge is of the corona type with a high voltage electrode embedded in ceramic and with the assembly placed adjacent to the grounded, main discharge anode. The preionization electrode is attached to the main discharge cathode from which it derives the small amount of power for the corona discharge. Because of this direct connection, discharge timing is automatic, with the preionization discharge preceding the main discharge by about 25 nsec. Main discharge ignition occurrs at about 18 kV in the voltage rise after switch closure. The main discharge current pulse is in the form of a 200 nsec wide, half-sine wave with a peak amplitude of 2 kA. The discharge module design is such that no failures were noted for about 80 million shots. In contrast, prior experiments with the alternative spark discharge preionization scheme showed that electrode erosion and insulator high voltage breakdown limited life to about 5 million shots. The discharge module parameters are summarized in Table 3-5.

Table 3-5. Discharge module and pulsed power parameters.

Characteristic	Value
Discharge dimensions	1x1x25 cm^3
Storage capacitance	20 nF
Charge voltage	20-25 kV, variable shot-to-shot
Current peak	2 kA
Input energy	4-6 J
Specific input energy	240 J/liter-atm
Repetition rate/duty cycle	200 Hz, 40%

The pulsed power system was a conventional capacitive discharge type composed of a command charge power supply, energy storage capacitor, and high voltage switch. Timing pulses for the charging and switch firing sequence were generated by electronics contained in the wavelength shifter and routed to the laser electronics module described in Section 3.1.4. The electronics module generated the final charge command and high voltage trigger for the switch.

A compact command charge power supply was developed that operated with an input of 28 Vdc and charged the energy storage capacitor bank to 20-25 kV in 4.5 msec at a rate of 1200 J/sec with a constant current waveform.[1] The charge voltage was variable from shot-to-shot at a 200 Hz rate, allowing for a variation of discharge input energy from 4 J to 6 J. This was found helpful in reducing the variation of laser output energy from strong to weak lines. For the weak lines, the capacitor bank was charged to the higher voltages.

The power supply was designed with emphasis on its functional characteristics rather than on minimizing size and weight; nonetheless, it is still fairly compact, measuring 5 x 5 x 14 in^3 and weighing 17.6 lb. Although one of the three power supplies delivered under the program demonstrated a fairly long life, it was characteristic of these supplies that electromagnetic interference (EMI) disrupted the control circuitry leading to failure of the transistor input to the high

voltage transformer. Further work is required in this area to develop protection circuitry. Finally, it should be noted that the 28 Vdc input requires the use of heavy cabling to carry the high peak currents (up to 80 A) while maintaining acceptably low resistive losses. The cable weight exceeds the power supply weight in its present 50 ft long configuration for field use.

For reasons of reliability, more robust commercial power supplies were routinely used in the laboratory and the field. These alternative power supplies included a large rack-mountable type and a compact model that could be mounted adjacent to the laser (on the sensor optical table).[2] Both types require an input of 208 Vac and offer variable voltage output, controlled through the digital link to the wavelength shifter. The compact model has a volume of 4 x 5 x 14 in^3 and weighs 15 lb.

A variety of energy storage capacitors were tested, including reconstituted mica types and ceramic capacitors with strontium titanate dielectric. The mica variety was desirable for its low relative weight and compactness; however, it was found that lifetime was only about one million shots when the construction was such that the capacitor internal inductance was kept within acceptable limits. Ceramic capacitors were therefore chosen for FAL because of their superior lifetimes. No capacitor failures have been noted in 80 million shots. The penalty with ceramic capacitors is greatly increased size and weight, roughly a factor of three over the mica variety. Finally, ceramic capacitors experience a capacitance derating with voltage; however, for the types used in FAL, the derating was below about 10%. The capacitor bank for FAL is composed of eight capacitors of 2.7 nF each, contained in a potted package measuring 3 in. wide, 4 in. high, and 6 in. long. [3]

In order to meet the laser lifetime design goal of 10^8 shots, two long life switches were tested. These included the crossatron, developed by the Hughes Research Laboratories, and the hydrogen thyratron.[4] The crossatron makes use of a low pressure plasma discharge in a crossed electric and magnetic field. The crossed fields induce a spiral motion of the ionizing electrons that is superimposed on a basic circumferential trajectory around the tube perimeter. The result is that the inherent long mean free path for ionization is contained inside a reasonably sized envelope. The switch tested on FAL was approximately 4 in. in diameter and weighed 4 lb. Smaller and lighter varieties became available later, but were not available at the time of FAL testing. The attributes of the crossatron are the elimination of a hot cathode (and its power consumption), extremely long life (on the order of 10^{10} shots), and immunity to damage caused by current reversal. Although initial testing gave some encouraging results, concerns with size and weight, problems with fine tuning of the reservoir power and trigger waveform, and certain issues related to quality control suggested the use of the alternative thyratron switch.

A thyratron switch was developed with the intention of minimizing the cathode and reservoir heater power while providing a lifetime of greater than 10^8 shots. The final tube design gave an acceptable total heater input power of 60 W and a warm-up time of 5 min. Various circuits were considered that had the potential of reducing warm-up time to 40 sec by application of large initial currents, followed by lower level plateaus; but these were not implemented on FAL. Rather, laser warm-up time was found to be limited by the catalyst heater. Testing of the switch under conditions similar to the FAL application showed a lifetime exceeding 10^8 shots, as required. A lifetime of 70 million shots was demonstrated with FAL and in other tests involving severe arcing. No switch failure has been noted.

3.1.4 Electronics

This section describes the functional characteristics of the modules that comprise the laser control electronics, including the rack-mounted power and signal module, fire control modules assembled under the laser pressure vessel, and the computer interface. The specific controls layouts are described in detail in Section 3.1.9, Laser Operating Procedure, and in the various sections detailing operation of the individual components.

Module descriptions

The modules are shown in the block diagram of Figure 3-5 with the power and signal connections. The physical arrangement of the modules is shown in Figure 3-6.

The Laser Power/Signal Module is a rack-mounted unit normally placed remotely from the laser. It takes 220 Vac power and the RS-232 input from the computer which can be an IBM-compatible Laptop type or personal computer (PC). Cable outputs from this unit include an 80 A, 28 Vdc line connected directly to the high voltage power supply; a low current, 28 Vdc line that powers the control electronics, and a signal cable that provides for a computer and diagnostics link. The Laser Power/Signal Module incorporates a commercial power supply that can accept inputs of 187-265 Vac at 47-440 Hz or 260-370 Vdc and has an output of 28 Vdc at 80 A. Therefore, a variety of input power types can be accommodated in a laboratory or field setting. The module also includes buffered diagnostic signal output ports and trigger outputs as detailed in Section 3.1.9. The module was intended to act as a laboratory diagnostics unit and the laser can operate without it, in which case the 28 Vdc and RS-232 computer links can be made directly to the Laser Control Electronics Module.
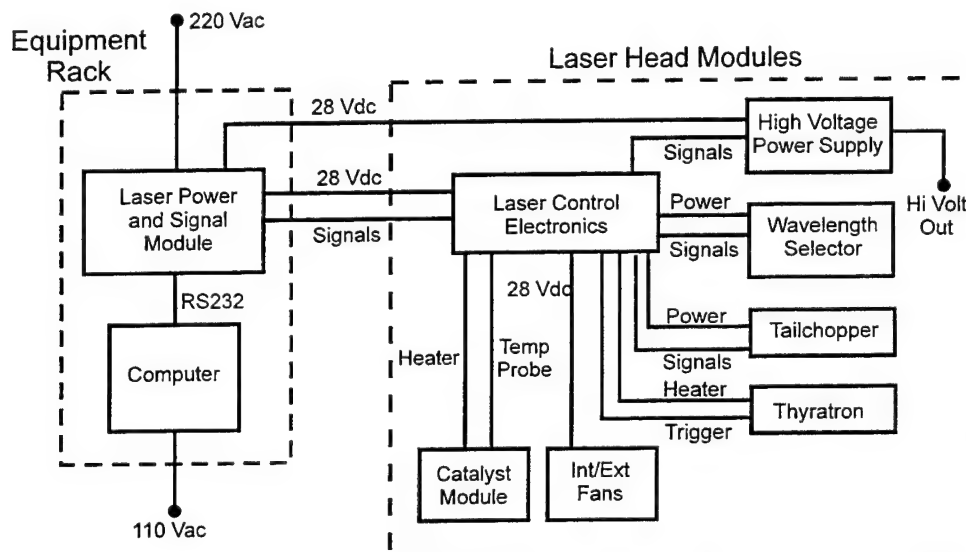
Figure 3-5. Laser electronics modules, power and signal distribution.
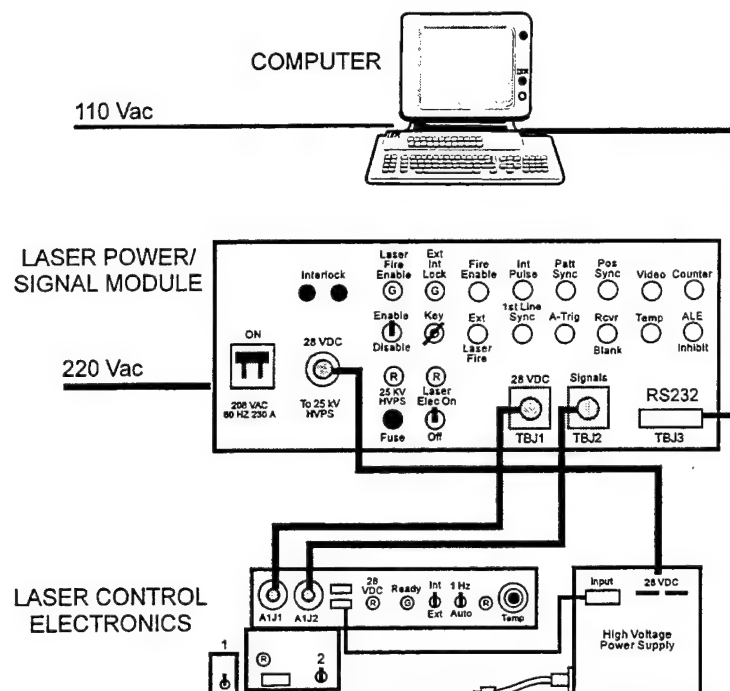
Figure 3-6. Electronic module arrangement.

All of the units shown within the dotted line of Figure 3-5 are placed adjacent to the laser head. The Laser Control/Electronics Module provides power to all subunits; it supplies the high voltage trigger for the thyratron switch, a trigger for the tailchopper high voltage pulser, and acts as a pass-through for RS-232 signals between the wavelength shifter and computer. This module also incorporates the feedback-controlled power supply for the catalyst heater. Catalyst temperature is controlled by a combination of pulse width modulation of the input power and turn on/off of the external cooling fan attached to the heat exchanger. In the warm-up mode, power is supplied to the embedded catalyst heater without modulation and with the external fan turned off until a nominal catalyst temperature of 55 $^{\circ}$C is reached. At that point, the external heat exchanger fan is turned on at constant speed and the input power is regulated through the closed loop controller to maintain the catalyst temperature at its set point.

Input power

Baseline laser power consumption is determined by the components shown within the Laser Head Modules block of Figure 3-5. The items shown within the Equipment Rack block are not included in the power calculation because of their peripheral nature. As noted previously, the Laser Power/Signal Module was intended to be used for laboratory diagnostics and power conditioning and the laser could operate without it. Furthermore, the computer could take many forms, including a Laptop and a rack-mounted PC.

The baseline laser head input power is shown in Table 3-6 for the standard burst mode defined in Section 3.2.2, consisting of a 16 line pattern and 4 Hz burst rate. Note that the catalyst heater dissipates 200 W during warm-up; but the power reduces to about 50 W once the

operating temperature is reached and before the discharge is turned on. With operation of the discharge and its high heat load, the catalyst input power drops further to about 20 W. The discharge input power to the gas is 276 W for a 16 line pattern and 4 Hz burst rate, assuming 12 strong lines requiring a 20 kV discharge voltage and 4 lines requiring 25 kV. However, the catalyst drop in power to 20 W is not instantaneous with discharge turn-on. Considering these factors, the catalyst input power is taken as 20 W during discharge operation and it is during discharge operation that the largest power draw is experienced. Finally, the high voltage power supply efficiency is estimated to be 90%.

Table 3-6. Laser input power.

Component	Input Power (W)
Internal fan motor	35
External heat exch motor	25
Catalyst heater	20
Thyratron	60
High voltage power supply	320
Tailchopper	10
Wavelength selector	60
Laser control electronics	30
Total	560

Signal timing

Fire control timing, as well as all wavelength pattern parameters, are determined by the wavelength selector which provides signals for the start of command charge of the high voltage power supply, thyratron switch fire command (laser discharge), and delayed trigger for the tailchopper voltage pulser. The timing signals are shown schematically in Figures 3-7 and 3-8 and should be compared to the diagnostics signals available from the wavelength shifter detailed in Section 3.1.6, under the subsection Diagnostics and test results. A pattern of four laser wavelengths is shown where details of nonfiring lines and skipped patterns required for the pseudo-resonant galvanometer to achieve a certain burst repetition rate have been ignored.
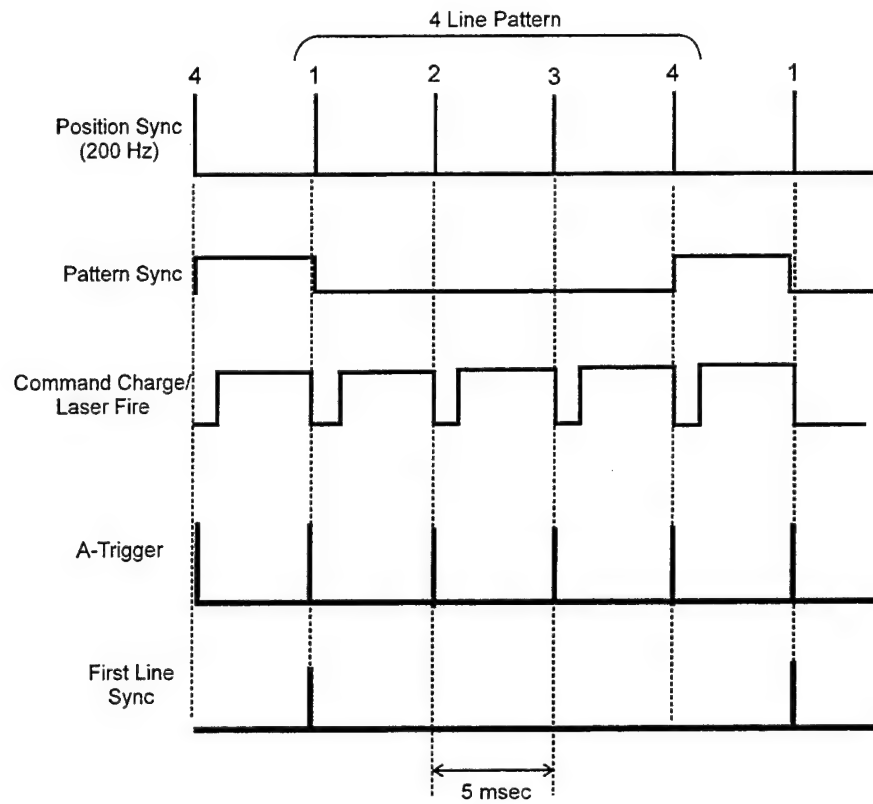
Figure 3-7. Laser fire control timing signals - coarse scale
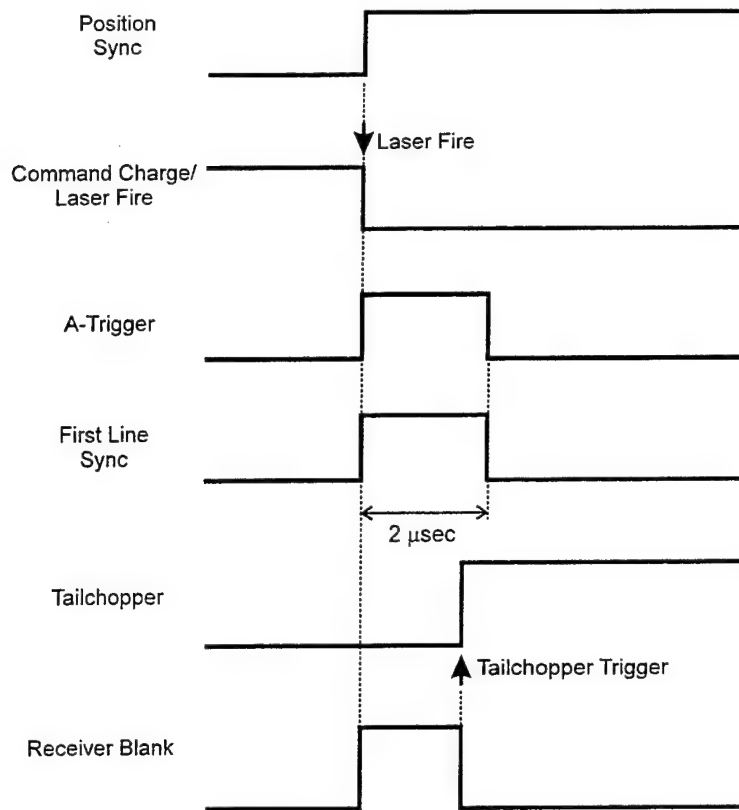
Figure 3-8. Laser fire control timing - fine scale.

The various signals are summarized in Table 3-7. The wavelength shifter issues the position sync which occurs at the galvanometer resonance rate of 200 Hz (5 msec period). The wavelength shifter also issues pattern sync (which occurs at the beginning of each pattern) and it issues the command charge signal which is sent to the high voltage power supply. About 4.5 msec is required to charge the capacitor bank after which the laser fire command is issued. After a delay determined by the computer for each line, the tailchopper trigger is sent to the CdTe crystal high voltage pulser. The first line sync and receiver blank pulses are generated for the purpose of interfacing with the sensor data acquisition system. As detailed in Section 4.1.5, on the sensor data acquisition system, first line sync initiates the data acquisition sequence for each burst and A-trigger initiates the acquisition for each segment within a burst.

Table 3-7. Summary of timing signals.

Signal	Characteristic
Position sync	Generated by wavelength shifter, 16 μsec width
Pattern sync	Generated by wavelength shifter, 5 msec width
Command charge/laser fire	Generated by wavelength shifter, 4.5 msec width
A-trigger	Coincident with laser fire, thyratron trigger
First line sync	Coincident with first line of each pattern
Tailchopper	Computer-controlled delay for crystal pulser
Receiver blank	Starts at A-trigger, ends at tailchopper pulse

20

3.1.5 Optics

The two optical systems used on FAL are illustrated schematically in Figure 3-9, with the first embodiment shown in (a) and the later, improved design shown in (b). These are top views with the exception that the beam expander in (b) has been rotated 90 deg for clarity. In both cases (a) and (b), the optical system is composed of a wavelength selector, output coupler assembly, and intervening Brewster windows that seal the pressure vessel. The wavelength selector and coupler assembly are attached to either end of an optical bench. The wavelength selector is discussed in detail in Section 3.1.6. The design in (a) is based on a conventional output coupler with a mode diameter of 1 cm at the output aperture. Coupler optical damage problems experienced during life testing with this design led to the redesigned version in (b), wherein the conventional coupler was replaced with a 3-fold beam expander that was successful in eliminating damage. Finally, optical damage was also experienced during life testing with the original ZnSe Brewster windows, but was eliminated with the use of NaCl windows. The optical design parameters are shown in Table 3-8.

(a)

(b)
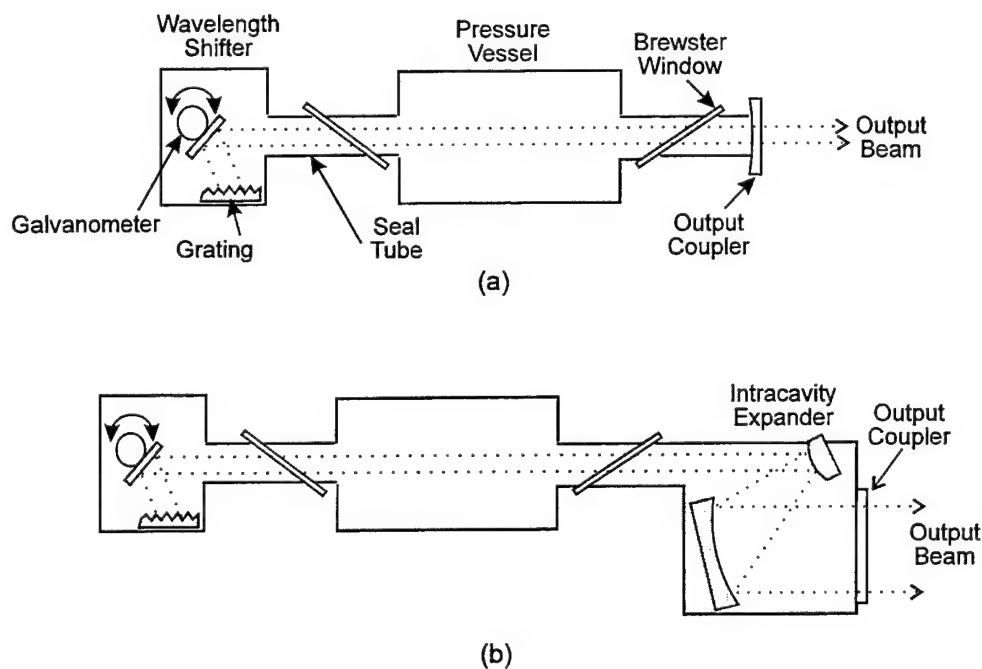
Figure 3-9. (a) Conventional optical system and (b) with expander.

Table 3-8. Optical system parameters.

Characteristic	Value
Conventional coupler	
Coupler material	ZnSe
Resonator length	61 cm
Intracavity mode size	1x1 cm
Coupler radius of curvature	20 m
Output coupler reflectivity	86%
Intracavity flux at coupler	7 MW/cm^2
Intracavity expander/coupler	
Expansion factor	3
Resonator length	80 cm
Coupler material	ZnSe
Intracavity mode size at coupler	3x3 cm
Coupler radius of curvature	20 m
Output coupler reflectivity	90 %
Intracavity flux at coupler	1 MW/cm^2
Brewster windows	
Original material	ZnSe
Redesign material	NaCl
Mode size at window	1x1 cm
Flux at window	2.7 MW/cm^2

Optical bench

The optical bench was designed with the assumption that it would experience temperature differentials of 20 °C over each major dimension. The assumption was made that the most severe differential, either along or across the bench, could be from room temperature to either 0 °C or 40 °C. In separate tests it was established that an alignment accuracy of ± 10 μrad would be required between the output coupler assembly and the wavelength shifter. In addition, it was necessary that the bench have sufficient rigidity and that the mechanical resonance be high enough that it would meet the requirements on shock and vibration. Finally, it was necessary to minimize the weight of the bench in order to meet the total weight requirement.

A number of alternative designs were analyzed, including thermally insulated aluminum benches, aluminum benches with active thermal control, invar material, and various composite materials. It was found that only the graphite-epoxy composite bench could provide a cost-effective, low risk approach. In that respect, the final design process accounted for the inertia of various components attached to the bench and included a structural and thermal analysis using various graphite-epoxy composite material thicknesses, construction techniques, and support web geometries. A schematic top and side view of the bench are shown to the correct scale in Figure 3-10 with the improved output coupler assembly (employing an intracavity expander) and the wavelength shifter shown in their proper orientations.

Top View

Side View
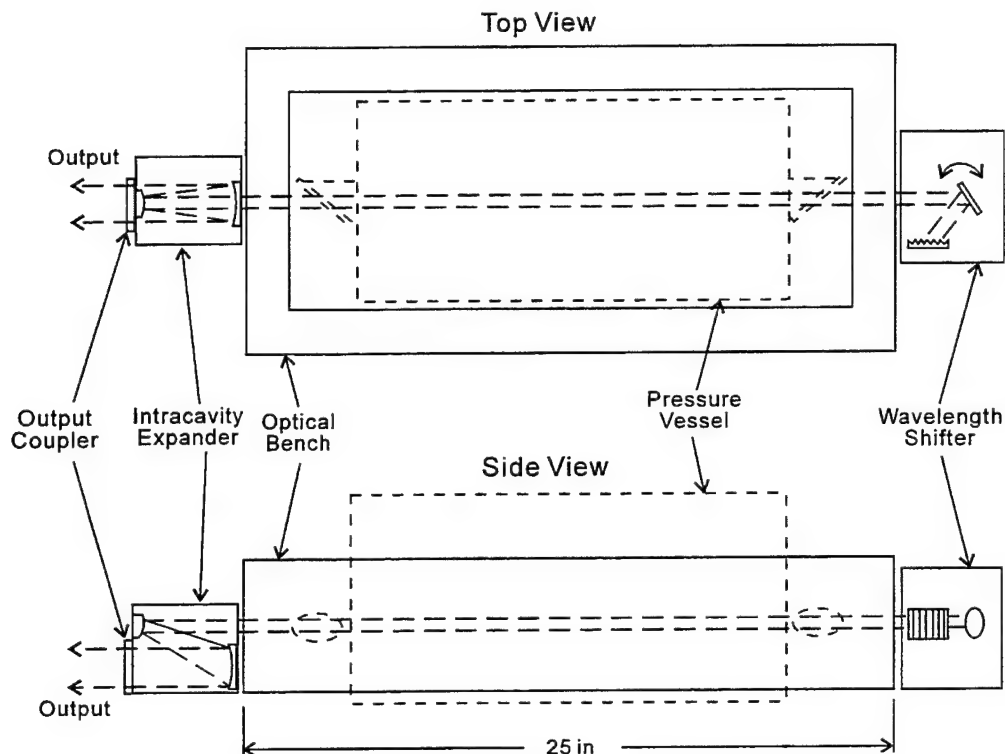
Figure 3-10. Optical bench schematic.

The composite bench was constructed from 0.060 in. thick material material with a 4-ply weave to achieve a "zero" coefficient of thermal expansion over the temperature range of 0-40 $^\circ$C. The optimized method of construction called for flat face sheets along all outside surfaces with internal composite webs. Invar inserts with composite reinforcing webs were used to attach the various components to the bench. A modal frequency analysis using the MSC/NASTRAN finite element analysis code showed the lowest resonant frequency was 452 Hz. The bench specifications are shown in Table 3-9.

Table 3-9. Optical bench characteristics.

Characteristic	Value
Material	Graphite-epoxy composite, 4-ply, 0.060 in. thick
Construction	Flat face sheets, internal webs, invar inserts
Coefficient of thermal expansion	0
Resonance frequencies	452 Hz, 612 Hz, and 615 Hz
Dimensions	5 in.x11.5 in.x25 in.
Weight	5.6 lb

The bench was tested indirectly in parallel with the integrated laser as detailed in Section 3.2.4. The bench did not experience any failure under the 3 G shock test or the 2 G sine wave vibration test. Although the vibration test conditions included the 452 Hz resonant frequency, no

structural problems were observed; therefore, it is likely that the actual resonance frequency was higher than that calculated. In addition, it was found in thermal testing that the output mode pattern did not experience any major shifts for which bench misalignment would have been suspected; and output energy variation was attributable to other effects. Finally, field testing under various conditions did not show laser misalignment problems.

Test results and design modifications

The laser was tested with the conventional resonator design of Figure 3-9(a) for a lifetime of 50 million shots over a period of about 27 days as described in Section 3.2.5. It was found early in the life test, after about 3 million shots, that the ZnSe output coupler became damaged to the extent that laser output was compromised. After about 5 million shots, both ZnSe Brewster windows both showed damage as well, but of a nature different from that of the output coupler. These two findings were repeated in further tests. In all cases, the laser was operated in the standard burst mode which consisted of a 200 Hz firing and wavelength shift rate, 40% duty cycle, and 16 wavelengths in a pattern spanning the 9 μm and 10 μm bands (see Section 3.2.2). Charge voltage and discharge energy were fixed at 20 kV and 3.8 J, respectively; and maximum intracavity flux density averaged over the mode with this condition was 5 MW/cm^2 at the coupler and 2 MW/cm^2 at the windows.

Since optical damage of the couplers and windows was thought to be directly related to intracavity intensity, the laser beam was diagnosed for mode structure in order to determine peak intensity across the mode. In that regard, beam profiles were obtained in both the near and far fields (see Section 3.2.4). It was found that the profiles contained peaks that exceeded the average intensity by only about 15%, suggesting that the intracavity intensities mentioned above should be a good estimate of the levels that led to the coupler and window damage.

The output coupler damage was characteristic of that observed on many different partial reflectors and under many different laser conditions. That is, widespread pitting could be observed by the naked eye across the mode cross-section on the partially reflecting side of the optic. Under microscopic examination, these pits resembled characteristic craters edged with fused material. Based on the results of an optical damage program carried out at Hughes, it is thought that the pitting is due to ablation of the coating and adjacent substrate, initiated by laser light absorption at a coating flaw or particulate contaminant. The particular vendor's optical substrate and coating were evaluated in the prior damage program and were found to have the highest damage threshold available. Therefore, it was determined that output coupler survival could be accomplished only by reducing the intracavity flux. This led to intracavity beam expansion at the output coupler to reduce the flux as shown in Figure 3-9(b). An alternative method using a three-mirror resonator was not found to be acceptable, because of damage incurred on the third intracavity optic.

The output coupler was modified to incorporate an intracavity beam expander in the form of a Dall-Kirkham telescope with a magnification of three. This geometry incorporates total reflecting aspheric primary and spherical secondary copper mirrors. These mirrors have been shown to have high damage thresholds consistent with shot lifetimes on the order of 50-100x10^6. The output beam was expanded from 1x1 cm to 3x3 cm and the flux on the output coupler was

reduced by a geometric factor of nine. Near field profile measurements showed that the flux was uniform and no damage has been observed for about 5 million shots; therefore, it is believed that the output coupler will not damage for the 50-100 million shots required.

Brewster window damage was in the form of reddish spots that formed both on the air and laser gas sides. Spots on the laser gas side were generally found to be more widespread and larger than those on the air side in repeated testing. The spots were found to grow with the number of shots until they covered a large portion of the beam cross-section. Because of the disparity between the damage on the air and gas sides of the windows, chemical reaction on the laser gas side was suspected; therefore, electron spectroscopy for chemical analysis (ESCA) and Auger electron spectroscopy (AES) were performed.[5]

On the laser gas side of the window, spectral peaks due to ZnSe, elemental Se, SeO_2, and some form of Zn and/or Se carbonate were found. These are not unexpected since it is likely that window damage was initiated by ablation of a surface contaminant, such as dust, or by ablation at a surface flaw, such as a scratch developed during polishing. Both contaminants and flaws are likely to be highly absorbing at 10 μm and to ignite to form hot, dense plasmas in contact with the optical surface. Such phenomena are visually apparent in both high power cw and pulsed lasers. Decomposition of the ZnSe window material would be expected under these conditions. In addition, C, CO, O, O_2 , and excited species are produced in the laser discharge so that production of oxides and carbonates based on the elemental window compounds would not be unexpected. The reddish color is likely due to an amorphous Se elemental phase.

On the air side of the window, ZnSe was found to be the dominant species present as a free contaminant and SeO_2 was found in much smaller amounts than on the laser gas side of the window. No carbonates were present. These results indicate the presence of an abundance of chemical reactions at the laser gas side leading to a variety of compounds that do not occur on the air side.

Repeated testing of the ZnSe Brewster windows using various preparation techniques did not alleviate the damage, nor did purging of the window area with a recirculating pump and filter system. As a result, alternative materials were considered. It was found that the group at the Societe' Anonyme de Telecommunications (S.A.T.) had used NaCl windows with good results to lifetimes of 20 million shots under conditions similar to the FAL.[6] Subsequent testing in the FAL to 10 million shots with NaCl windows showed no damage either. The FAL was retrofitted with NaCl Brewster windows and the intracavity path was hermetically sealed to prevent window degradation by water vapor. Finally, the use of NaCl did not allow hard sealing of the window to the mounting flange as had been the case with the ZnSe windows. The NaCl windows were sealed with O-rings.

3.1.6 Wavelength Selector

The wavelength selector performs the functions of wavelength selection and laser fire control.[7] It provides the means to shift wavelengths at a 200 Hz rate by use of a stationary grating and a copper mirror attached to a reciprocating galvanometer. The various wavelength patterns, firing rates, and voltage levels for each wavelength are stored in the wavelength selector

non-volatile random access memory (RAM). Because the shifter is a pseudo-resonant device, all other laser timing functions are slaved to its resonant frequency to achieve synchronization of the laser fire commands with the galvanometer position. Therefore, the wavelength selector also provides all laser fire timing signals, including command charge of the high voltage power supply, logic signal to set and initiate charge voltage, trigger for the thyratron high voltage switch, and trigger for the tailchopper high voltage pulser. These functions are shown in the block diagram of Figure 3-11. The wavelength selector is connected by an RS-232 interface to the computer from which wavelength patterns and laser firing parameters are downloaded. Signal connection to the laser electronics module is made through an RS-422 link. Both signal connections and power connections are contained in a single cable that connects to the selector housing through a 26-pin, high density, microminiature, D shell connector. Further details of the electronics interface are discussed in Section 3.1.4.
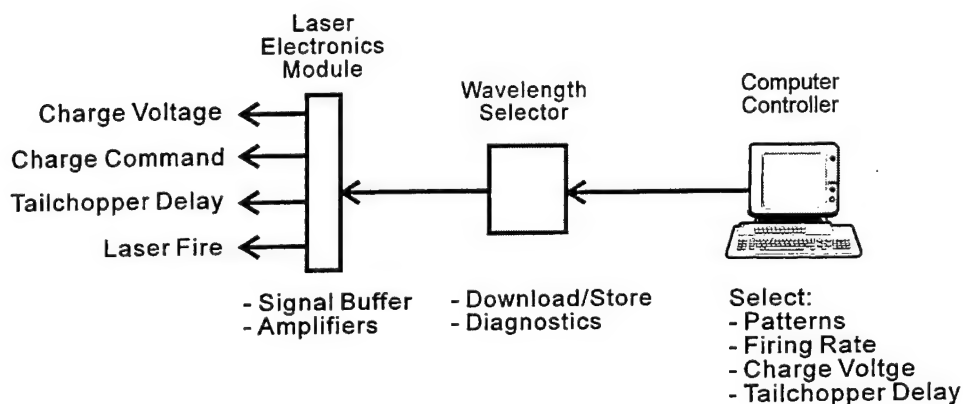
Figure 3-11. Wavelength selector interface.

Basic operation and characteristics

An outline of the wavelength shifter is shown in Figure 3-12 and a picture of the device with the cover removed is shown in Figure 3-13. The wavelength selector operates in the basic Littrow configuration. A copper mirror is attached to the reciprocating galvanometer which directs the laser beam onto the fixed grating at different angles. Laser output occurs for those angles that are both retroreflecting and which match a laser emission wavelength. In order to access the 9 and 10 µm branches, the beam must impinge on the grating with an angle that varies over 10 deg and this requires a 5 deg angular rotation of the galvanometer. In operation, the galvanometer performs a repeating pattern where the angular motion is reversed at the turning points. Although the galvanometer motion has a resonant character, the motion stops at those points in the travel (specific wavelengths) at which the laser is required to fire. Therefore, this type of operation is termed pseudo-resonant. Also shown in Figure 3-12 is the position sensor. A mirror is attached to the end of the galvanometer opposite the copper turn mirror and a laser diode with a linear charge-coupled device (CCD) detector array are used to sense galvanometer rotational position. The position sensor is shown reflecting off of the copper mirror for illustration only. The position accuracy is within ± 10 µrad and is achieved in this relatively small package by frequency division and galvanometer position control is achieved by feedback. This method of position control, and

26

the pseudo-resonant nature of the galvanometer, are in contrast to the conventional galvanometer approach wherein the galvanometer is entirely non-resonant and is directed to an angular position where it stops until laser fire.
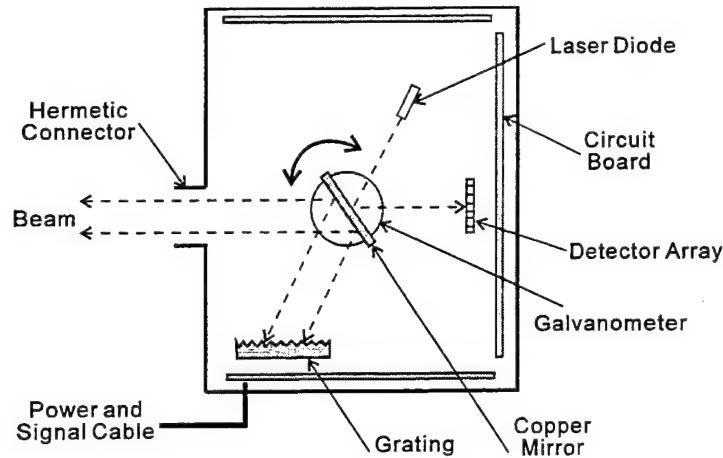
Figure 3-12. Wavelength selector outline view.
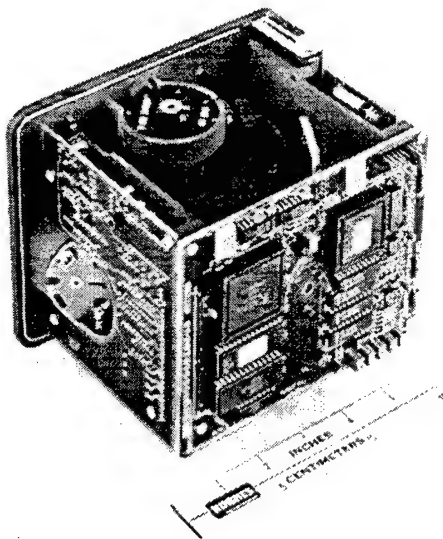
Figure 3-13. Picture of wavelength selector.

The specifications of the wavelength selector are shown in Table 3-10. In the present software configuration, it can accommodate 16 different patterns with 20 wavelengths each; but in principle, any number of wavelengths per pattern could be made available with an increase in the shifter memory size. The wavelengths can be chosen from among any of the 65 wavelengths available in the 9 and 10 μm bands and in any order. For each of the wavelengths in the pattern, the charge voltage and timing delay of the tailchopper can be designated. Charge voltage specification is useful when switching between strong and weak lines, because the variation in output can be controlled to some extent by decreasing input energy for the strong lines and increasing it for the weaker ones. Tailchopper delay control is important because the emission of strong lines is typically delayed by about 700 nsec from the time of the discharge current pulse;

27

whereas, it is delayed by about 800 nsec for weak lines. Therefore, the timing of the tailchopper must be tailored to the line strength if similar pulse shapes are to be obtained for all lines.

Table 3-10. Wavelength selector specifications.

Characteristic	Value
Beam size	$1 \times 1 \ cm^2$
Resonance frequency	200 Hz
Max wavelength shift rate	200 Hz
Max wavelengths in pattern	20
Max patterns	15
Resolution	10 μrad
Optical access angle	10 deg
Wavelength access	9R32 to 10P32
Grating period	150 lines/mm
Size	6 in. wide, 5 in. high, 5 in. along optic axis
Power	± 15 Vdc, 1.6 A + 5 Vdc, 0.4 A
Interface	RS-232, RS-422
Weight	4.3 lb

The laser can fire at a maximum repetition rate of 200 Hz, but only for short bursts with a duty cycle of 40%, giving a maximum average repetition rate of 80 Hz. The maximum average repetition rate is limited by the amount of gas processed by the catalyst module. In that respect, the repetition rate or duty cycle could be increased by further development of the FAL flow system. Furthermore, because of the pseudo-resonant nature of the galvanometer, certain firing rates and burst rates are "forbidden", depending upon the number of wavelengths in the pattern. Finally, certain wavelength selector software and firmware characteristics limit the choice of maximum repetition rate to 200 Hz, 100 Hz, 68 Hz, and 50 Hz. These are achieved by simply turning off the laser discharge for certain wavelengths among the 20 available in a pattern. As a result of these constraints, the available firing rates are restricted to those shown in Table 3-11. Although the choice of rates is not continuous (as it would be for a non-resonant galvanometer), it is sufficiently wide to give a very broad choice of operating conditions. The table shows the maximum burst rates available (and the corresponding average repetition rate) for each of the four values of peak repetition rate within a burst. The column designated single wavelength repetition rates gives the repetition rates available for continuous firing of a single wavelength in a pattern.

Table 3-11. Available firing and burst rates.

Wavelengths in Pattern	Max Burst Rate (Hz)/Ave Rep Rate (Hz)				Single Wavelength Rep Rates (Hz)
	Peak Rep Rate 200 Hz	Peak RepRate 100 Hz	Peak Rep Rate 68 Hz	Peak Rep Rate 50 Hz	
1	66.7/66.7	66.7/66.7	66.7/66.7	40/40	1
2	40/80	40/80	28.6/57.1	22.2/44.4	2
3	22.2/66.7	22.2/66.7	22.2/66.7	15.4/46.2	3
4	20/80	18.2/72.7	15.4/61.5	11.8/47.1	4
5	15.4/76.9	15.4/76.9	13.3/66.7	10/50	5
6	13.3/80	13.3/80	10.5/63.2		5.9
7	11.1/77.8	11.8/82.4			6.9
8	9.1/72.7	5.9/47.1			8
9	9.1/81.8	5.3/47.4			8.7
10	7.7/76.9	5/50			10
11	6.7/73.3				10.5
12	6.7/80				11.8
13	5.9/76.5				12.5
14	5.9/82.4				13.3
15	5.3/78.9				14.3
16	3.9/62.7				15.4
17	3.9/66.7				16.7
18	3.5/63.2				18.2
19	3.5/66.7				20
20	3.3/66.7				22.2
					25
					28.6
					33.3
					40
					50
					66.7

Software

The wavelength selector software provides for user-specification of all wavelength selector and laser firing parameters. Basically, there are four screens available, three of which branch off the main screen as shown in Figure 3-14. The three branch screens contain the Line Peaking menu, selectable by the L key; the Calibrate menu, selectable by the C key, and a two page screen that holds the roster of patterns and positions, selectable by the Page Down key. The various screens are only accessible through the main screen.
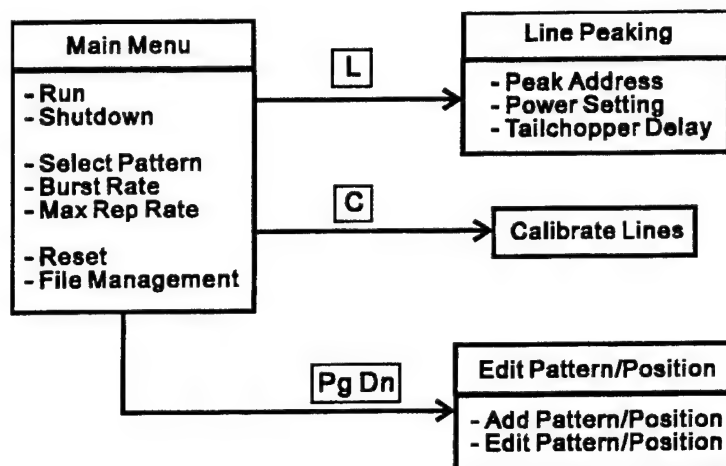
Figure 3-14. Wavelength selector menu options.

The Main Screen of Figure 3-15 provides a basic user-selectable operations menu shown in the Commands window which includes laser run/shutdown, selection of the wavelength pattern to be run, and management of the wavelength pattern files. Two other windows contained in the Main Screen show status and the pattern to be run. The Status window indicates the burst rate and average repetition rate derived from the entries of Table 3-10. In operation, the user specifies a desired maximum repetition rate (M key), burst rate (B key), and lines in the pattern. Because of the pseudo-resonant nature of the galvanometer, the burst rate is treated as a dependent variable and is calculated in software. The burst rate value nearest to that desired is determined and displayed. The Status window also indicates the appropriate error messages in the event of selector malfunction, but it does not show any error messages related specifically to operation of the laser head. The Pattern window shows the sequence of selected wavelengths with their spectroscopic notation.

Figure 3-15. Wavelength selector main screen.

The selection of wavelengths for each pattern and the editing of those wavelengths and patterns is achieved through the Edit Pattern/Position screen shown in Figure 3-16 and accessed by the Page Down key. Two pages of patterns are available (through successive strokes of the Page Down key), allowing for storage of 15 patterns with up to 20 wavelengths per pattern. The run/shutdown, and pattern selection functions are also available through the Edit Pattern/Position screen. By choice of the menu item Add Pat/Pos in the Edit Pattern/Position screen, a secondary screen appears, shown in Figure 3-17, which contains the entire roster of wavelengths and from which the actual pattern-building is accomplished. The user is guided through the choice of wavelengths by an on-screen prompt.

```
     PAT C      PAT 1      PAT 2      PAT 3   PAT 4   PAT 5   PAT 6   PAT 7  ┌──── AGILE TUNER ────┐
BR  3.9        1          2.9                                              │
                                                                          │ A-ADD PAT/POS
0   9R30       10P20      10P20                                            │ E-EDIT POSITION
1   9R20                  10P12                                            │ C-DEL POSITION
2   9R10                  10P04                                            │
3   9P10                  10P42                                            │ D-DELETE PATTERN
4   9P16                  10R36                                            │ B-PAT BURST RATE
5   9P20                  10R26                                            │ V-VIEW PATTERN
6   9P30                  10R20                                            │ G-EDIT/UPDATE
7   9P44                                                                   │    RUNNING PATTERN
8   10R32                                                                  │
9   10R20                                                                  │
10  10R10                                                                  │ R-RUN
11  10R08                                                                  │ S-SHUT DOWN
12  10P08                                                                  │ P-SELECT PATTERN
13  10P10                                                                  │
14  10P20                                                                  └──────────────────────┘
15  10P32
16                                                                        ┌ PG UP-MAIN MENU  ┐
17                                                                          PG DN-PATS (8-15)
18
19

SELECT COMMAND _
```

Figure 3-16. Wavelength selector pattern and position edit screen.

```
     LINE       WAVE#        PATTERN 1
0    9R28                                 10P32   10R14   9P34   9R10
1    9R10                                 10P30   10R16   9P32   9R12
2    9P20                                 10P28   10R18   9P30   9R14
3    9P44                                 10P26   10R20   9P28   9R16
4                                         10P24   10R22   9P26   9R18
5                                         10P22   10R24   9P24   9R20
6                                         10P20   10R26   9P22   9R22
7                                         10P18   10R28   9P20   9R24
8                                         10P16   10R30   9P18   9R26
9                                         10P14   10R32   9P16   9R28
10                                        10P12   10R34   9P14   9R30
11                                        10P10   10R36   HN15
12                                        10P08   10R38   9P12
13                                        10P06   10R40   9P10
14                                        10P04   HN16    9P08
15                                        10R04   9P44    9P06
16                                        10R06   9P42    9P04
17                                        10R08   9P40    9R04
18                                        10R10   9P38    9R06
19                                        10R12   9P36    9R08


PRESS ENTER TO SELECT
OR TYPE IN LINE NAME    _
```

Figure 3-17. Pattern formulation screen.

31

The Line Peaking screen shown in Figure 3-18 is accessed by the L key from the main menu. In this screen the user can (1) tune the position of a line to achieve maximum output energy while the laser is firing, (2) specify the charge voltage and output energy per line, and (3) specify the tailchopper delay to tailor the output pulse profile. These functions are accessed by the indicated F keys and the values are incremented with the up/down arrow keys. In the line tuning mode, the galvanometer position is updated as the arrow keys are pressed and the last value is stored in memory with the Esc key. The charge voltage is designated by levels 1-4 with level 4 being the highest voltage of 25 kV. The tailchopper delay can be specified from 1-12, where 12 represents the longest delay of 4 μsec (no chopping) and 6-7 is typical of a 1 μsec tail.

```
       LINE    WAVE#           ADDRESS    PWR    Q-SWITCH         ┌═══╡ PEAK PATTERN ╞═══┐
  0    9R30    1084.63514549   219        3      7                │                       │
  1    9R20    1078.59064423   706        1      6                │       LINE- 9R30      │
  2    9R10    1071.88376618   1259       3      7                │      ADDRESS- 219     │
  3    9P10    1055.62506805   2647       2      7                │       POWER- 3        │
  4                                                               │      Q-SWITCH- 7      │
  5                                                               │                       │
  6                                                               ├───────────────────────┤
  7                                                               │  PEAKING POSITION-0   │
  8                                                               └───────────────────────┘
  9
 10                                                               ┌───────────────────────┐
 11                                                               │ F5-PEAK ADDRESS       │
 12                                                               │ F6-PEAK POWER SETTING │
 13                                                               │ F7-PEAK Q-SWITCH SETTING
 14                                                               ├───────────────────────┤
 15                                                               │  ▲-INCREMENT          │
 16                                                               │  ▼-DECREMENT          │
 17                                                               ├───────────────────────┤
 18                                                               │  INCR/DECR AMOUNT     │
 19                                                               │       F1-1            │
                                                                  │       F2-5            │
                                                                  │       F3-10           │
                                                                  │       F4-20           │
                                                                  ├───────────────────────┤
                                                                  │ ESC-EXIT/UPDATE POSITION
                                                                  └───────────────────────┘
```

Figure 3-18. Wavelength selector line peaking screen.

During alignment of the laser resonator, it is necessary to make a coarse adjustment of the wavelength shifter position to guarantee access to the far ends of the spectrum, including the lines 9R30 (9.22 μm) and 10P32 (10.72 μm). This is accomplished with metal shims at the shifter attach points and a check is made with a spectrometer. The next step is to precisely measure the positions of as many lines as possible in all branches in order to establish an accurate look-up table from which all patterns can be formulated. Normally, the position of every other line is measured and an interpolation scheme in the shifter software is used to interpolate between the measured lines.

The pattern spectral look-up table is shown in Figure 3-19. In this screen, all lines for which positions have been measured are indicated by an asterisk and are taken as calibration points by the interpolation algorithm. In addition, the input power and tailchopper delays can be specified for each line; however, these data are usually specified through the line peaking screen. Once the peak positions for all lines have been established in the calibration screen, they can be used to form the 15 available patterns. Further position, peak power, or tailchopper delay tuning can be done for each pattern but will not be reflected in the calibration screen.

```
LINE    WAVE#           ADDRESS  CAL  PWR  Q-SWITCH
10P32   932.96042043    16134     *    1     12
10P30   934.89449550    15886          1     12
10P28   936.80374726    15624     *    2     12
10P26   938.68825692    15367          1     06
10P24   940.54809793    15115          1     12
10P22   942.38333608    14869     *    1     06
10P20   944.19402961    14628          1     12
10P18   945.98022931    14393          4     12
10P16   947.74197860    14162     *    3     12
10P14   949.47931361    13936          2     12
10P12   951.19226324    13715          1     12
10P10   952.88084927    13498     *    1     12
10P08   954.54508632    13286          1     12
10P06   956.18498202    13079          1     12
10P04   957.80053691    12876     *    1     12
10R04   964.76898140    12016          1     12
10R06   966.25036076    11836          1     12
10R08   967.70723331    11660     *    1     12
10R10   969.13954739    11489          1     12
10R12   970.54724435    11321          1     12
10R14   971.93025845    11157     *    1     12
```

```
┌────────── LINE CALIBRATOR ──────────┐
│                                      │
│            LINE- 10P14               │
│         ADDRESS- 13936               │
│           POWER- 2                   │
│        Q-SWITCH- 12                  │
└──────────────────────────────────────┘

F5-PEAK ADDRESS
F6-PEAK POWER SETTING
F7-PEAK Q-SWITCH SETTING

    ∧ -INCREMENT
    ∨ -DECREMENT

  INCR/DECR AMOUNT
       F1-1
       F2-5
       F3-10
       F4-20

F8-ACCEPT AS CAL POINT
F9-ACCEPT W/O CAL POINT
ESC-EXIT WITHOUT UPDATE
```

Figure 3-19. Wavelength calibration screen.

Diagnostics and test results

Various diagnostic signals are available at the laser power supply panel described in Section 3.1.4. These are summarized in Table 3-12 and include a galvanometer position synchronization signal operating at a fixed 200 Hz repetition rate, a pattern synchronization signal emitted at each repetition of the wavelength pattern, a galvanometer position alignment signal window termed Int, and a video pulse that is intended to fit inside the Int window to indicate alignment accuracy. The video pulse is actually the output of the position sensing laser diode as it appears on the linear CCD sensor array. The timing of these various waveforms is shown in Figure 3-20.

Table 3-12. Wavelength selector diagnostic signals.

Signal	Type	Amplitude (V)	Duration	Period	Comments
Position Sync	Square Wave	4.5	16 µsec	5 msec	Runs during shutdown
Pattern Sync	Square Wave	4.5	5 msec	-85 msec, 16 lines, 3.9 Hz burst rate -25 msec, 5 lines, 5 Hz burst rate	Period depends on pattern
Int	Square Wave	4.5	8 µsec	Same as Pattern sync, 1 msec delay	Galvo alignment window
Video	Gaussian	1.25	3 µsec	Same as Int	Within Int window

The top illustration of Figure 3-20 shows the angular excursion of the galvanometer to the position of wavelengths in the pattern as a function of time. The vertical bars indicate the specific angles of the selected wavelengths where the galvanometer stops and the laser is able to fire. In order to achieve the proper burst rate, the software inserts nonfiring positions (indicated by the * in the figure) and skips a fixed number of patterns (no firing lines). These nonfiring positions and pattern skips are not visible to the user. The particular example is for a five wavelength pattern, firing at a maximum repetition rate of 200 Hz and burst rate of 8 Hz. The position sync pulse runs at a 200 Hz repetition rate and occurs at each position whether or not a particular line fires and the pattern sync pulse appears at the beginning of each pattern whether it is skipped (nonfiring) or not.
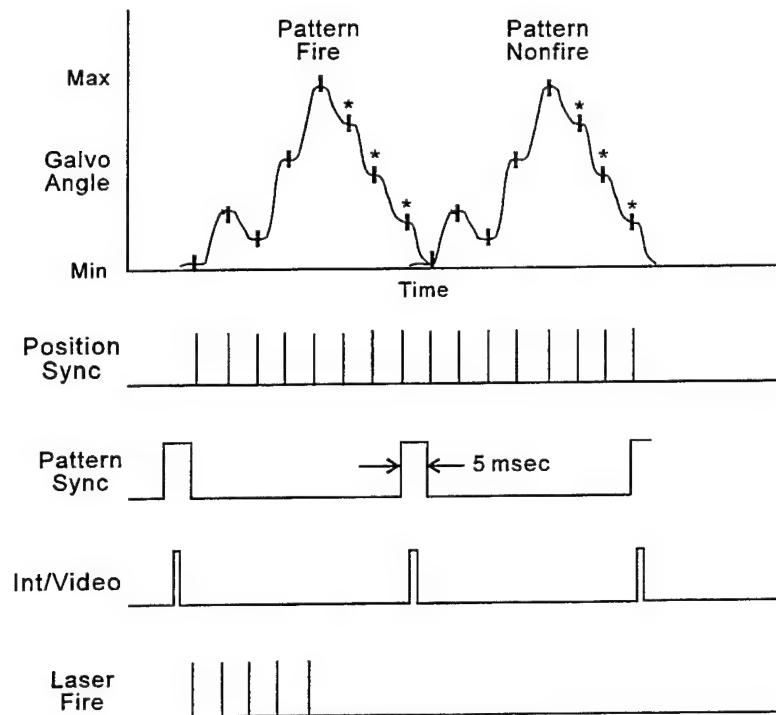

Figure 3-20. Diagnostic waveform timing.

For diagnostic purposes, the Int/Video pulses are of the most interest. The Video pulse is actually the profile of the laser diode position sensor and the Int signal is the timing pulse. Typical traces are shown in Figure 3-21 where the time base is 2 μsec/Div. Under normal conditions, the Video pulse resides at about the center of the Int window from shot-to-shot and the maximum voltage levels are about 1.5 V and 3 V, respectively. Maximum wander is a small fraction of the width of the central peak and the Video amplitude is relatively constant. Because the CCD array is fairly coarse over the laser diode beam cross-section, there will be some amplitude fluctuation of the "staircase" Video pulse shape, but the position centroid will be constant. However, the position accuracy of the wavelength selector can be affected by degradation of the position sensing components and severe environmental factors, including vibration and EMI generated by the laser. Under these conditions, the Video pulse may wander over 30% of the Int window and may fall outside the window at times, indicating that the wavelength selector stability is unacceptable. The FAL design precludes these problems.
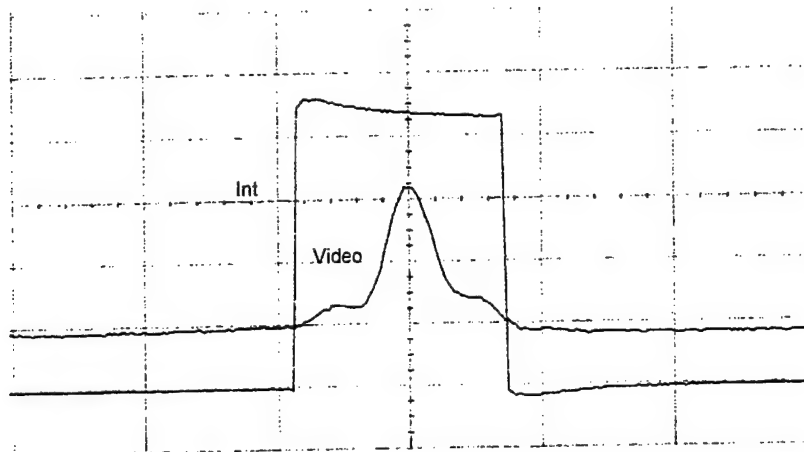
Figure 3-21. Typical diagnostic pulses.

The wavelength selector was tested for lifetime and environmental effects in parallel with the laser as discussed in Section 3. In addition, it was tested in the field with the integrated sensor as described in Section 4.2. The results of these tests are summarized in Table 3-13.

Table 3-13. Wavelength selector test results.

Test	Results	Comments
Temperature 0-40 °C	-Reliable operation -No misalignment of peak position noted	-Reduced output energy at 40 °C due to lower laser gain
Shock 3 G	-Reliable operation after shock along each axis	-Malfunction reported for operation during shock
Vibration 2 G	-Reliable operation after vibration along each axis	-Malfunction reported for operation during vibration
Lifetime	-Reliable electronics and position repeatability -Copper mirror degradation after 20 million shots	-Original copper mirror incorrectly fabricated -Predicted life with new mirror ~ 5×10^7 shots -Degraded mirror reflectivity may lead to reduced wavelength selectivity
Field operation	-Reliable operation	-Original I/O board susceptible to EMI. -Modified I/O board shows no effects -Reduced wavelength selectivity due to degraded mirror or beam expander

In general, reliability of the wavelength selector was good after elimination of the effects of EMI on the Input/Output circuit. Importantly, the selector was found to hold alignment under the 0-40 °C temperature excursion. In addition, alignment was also found to be good over several days of operation under field test conditions. Stability over the long term could not be tested, but there is no indication that this should be a problem. Any minor adjustments required under the various test conditions may well have been due to misalignment of other components, including the output coupler assembly and optical bench. It was found, however, that wavelength selectivity of the laser resonator degraded after about 20 million shots. This was particularly noticeable on the 9R branch of the spectrum where line separation is the smallest. It is suspected that the loss of

35

selectivity could have been due to increased scattering from the degraded wavelength selector copper mirror surface. The copper mirror was not fabricated from the specified materials nor was it polished to the specification and this probably led to its poor damage resistance. Experience has shown that a correctly fabricated mirror would have a lifetime far exceeding 20 million shots, but tests with the FAL in that regard were not performed.

3.1.7 Pulse Profile and Tailchopper

The FAL output pulse is composed of a gain-switched spike, followed by a low intensity tail. A typical temporal profile is shown in Figure 3-22. The trace designated "integral" is the integral of the intensity profile and therefore represents total output energy as a function of time. In this example which is characteristic of a strong line, the output pulse has the following characteristics:

Total energy:	200 mJ
Spike energy:	80 mJ, 40% of total
Spike FWHM:	110 nsec
Spike FW:	230 nsec
Tail at 1 μsec:	6 dB down from spike

For certain applications involving range-resolved measurements of aerosols, it is necessary to tailor the output pulse by eliminating the tail. In that respect, it was required in the FAL program to further reduce the tail amplitude at 1 μsec into the pulse from its natural value of 6 dB down to 60 dB, compared to the peak of the spike. Initial testing with extra-cavity CdTe electrooptic modulators showed that it was possible to reduce the 1 μsec tail amplitude by greater than 20 dB, the limit of resolution of the diagnostics.
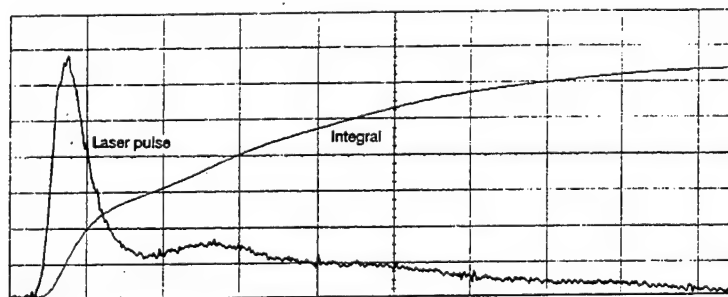

Figure 3-22. Output pulse shape, timebase 200 nsec/Div.

The tailchopper, shown schematically in Figure 3-23, is based on the transverse electrooptic effect using CdTe crystals. The tailchopper consists of several crystals in series, followed by a stack of six Brewster plates for polarization discrimination. The crystal ordinary and extraordinary axes are oriented at 45° to the laser field vector as shown in the bottom illustration of the Figure. In operation, the incoming laser electric field vector, **E**, is oriented parallel to the

crystal electrode surfaces; and with no voltage applied to the crystal, it remains in its original plane, passing through the Brewster plate stack unimpeded. With the half-wave voltage applied to the crystals, the field vector is rotated by 90° and the beam is completely reflected out of the transmit path by the Brewster plates. To achieve tailchopping, the half-wave voltage is applied at the time in the output laser pulse where it is desired to eliminate the following tail. The crystals and polarization discriminators are located extracavity, outside the laser resonator. The alternative case of placing the crystals intracavity, inside the laser resonator, and relying on the laser Brewster windows for polarization discrimination was precluded due to damage of the crystal anti-reflection coatings by the high intracavity flux.
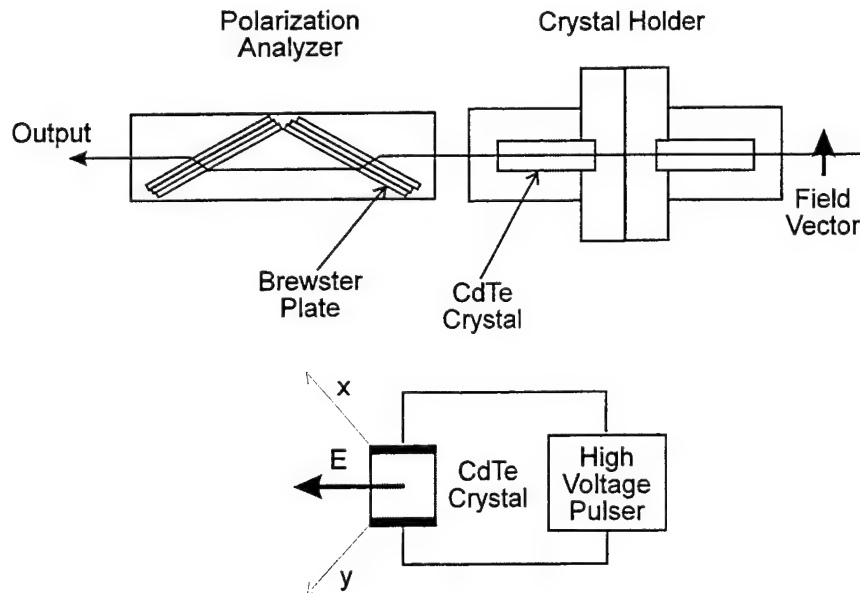

Figure 3-23. Tailchopper schematic view.

In practice, the CdTe crystals do not achieve a pure rotation of the field vector as described above when the half-wave voltage is applied. Due to birefringence caused by crystal flaws, pressure from the crystal mount, or piezoelectric effects from the voltage pulse, elliptical polarization of very high aspect ratio was produced. The field component in the plane of the original field vector is transmitted through the Brewster stack and may reduce the depth of modulation in the tail. Note that the depth of modulation in this case is not directly related to the usual extinction ratio quoted for Brewster plate polarizers which is the ratio of transmission for field vectors parallel and perpendicular to the plane of incidence.

Two basic designs were investigated, using two and three crystals in series and the parameters for each are summarized in Table 3-14. The first approach was based on using two crystals rather than three because of their expense and was designed with the assumption of a 12 kV pulser and a crystal length of 24 mm. However, it was found that the pulser could not develop the desired maximum voltage and that the supplied crystals were shorter than specified due to repeated polishing and anti-reflection coating by the vendor . The result was that the half-wave voltage could not be reached and the achievable attenuation was only 10 dB. In any case, the 2-crystal tailchopper was integrated with the laser and sensor and exposed to laser flux at a 200 Hz

37

repetition rate and various duty cycles for about 10 million shots without any trace of optical damage. The ultimate lifetime is not known.

Because of limitations with the 2-crystal tailchopper, a three-crystal device was designed in order to gain an operating margin. In addition, the polarization discriminator material was changed from ZnSe to Ge to increase the extinction ratio from 1000 to greater than 3000.

Table 3-14. Tailchopper characteristics.

Characteristic	Design 1	Design 2
No of crystals	2	3
Crystal size	12x12x21.5 mm	12x12x30 mm
Net half-wave voltage	12.6 kV	6 kV
Brewster plates (6)	ZnSe	Ge
Pulser max voltage	10 kV	10 kV
Pulser risetime	200 nsec	200 nsec
Pulser 1/e time	270 μsec	270 μsec
Attenuation	10 dB	>20 dB
Lifetime	>10^7 shots	>10^7 shots

A picture of the assembled three-crystal tailchopper and a view in one end are shown in Figures 3-24 (a) and (b), respectively. The housing for the three crystals is shown on the left of Figure 3-24 (a) with the high voltage leads protruding out the top and with the high voltage pulser at the base. The polarization discriminator with a large angle adjustment collar is shown to the right. In Figure 3-24 (b), the crystal can be seen located in the center and sandwiched between ceramic pieces at the sides with the electrodes at the top and bottom. The internal structure has a pulsed voltage hold-off value of about 12 kV.

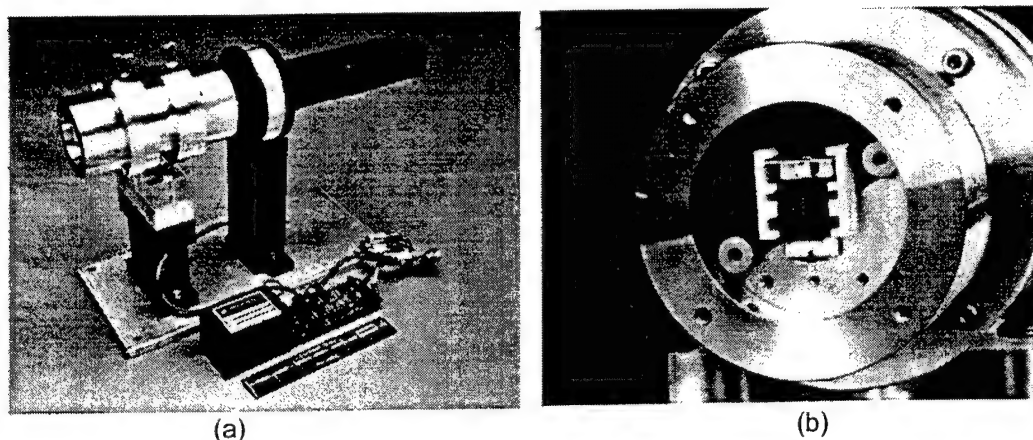(a)   (b)

Figure 3-24. Assembled tailchopper.

A typical output pulse profile and its integral are shown in Figure 3-25 for a strong line. The tail has been accentuated in this case by changing the resonator optics in order to illustrate the tailchopping effect. A typical trace with tailchopping at about 1 μsec into the pulse is shown in Figure 3-26. The pulse voltage trace indicates that the tailchopper half-wave voltage of 6 kV was achieved with a 200 ns risetime and a plateau much longer than the unchopped pulse. The plateau is necessary to prevent laser output late in the pulse which could be the case for a short high voltage pulse obtained from typical capacitive discharge circuits. The pulser in this case was

38

based on a pulse transformer design. The trace of Figure 3-27 shows a high resolution view of the pulse tail at the point of chopping to obtain a measurement of the extinction ratio. The gain of the oscilloscope was increased in this case, saturating the laser spike; however, tests with calibrated optical attenuators verified that the gain was still linear in the region of interest. Note that the trace after application of the voltage pulse is at the noise level. The exact value of attenuation in this case could not be determined, but values of 20 dB were measured with this technique in other experiments. Finally, Figure 3-28 shows the result of chopping the pulse immediately after the gain-switched spike. The tail suppression in this instance is not nearly as complete as for the case of chopping at 1 µsec. It was found through other experiments that the depth of modulation was dependent upon the optical flux at the point of voltage application. That is, clipping of lower laser intensities produced larger extinction ratios. In addition, it was found that the extinction ratio degraded as the tailchopper was used. The degradation was from greater than 20 dB to about 14 dB after 100 k shots. This may be related to migration effects in the crystal due to the very long high voltage pulse. Efforts to investigate these problems and improve tailchopper performance were not undertaken.
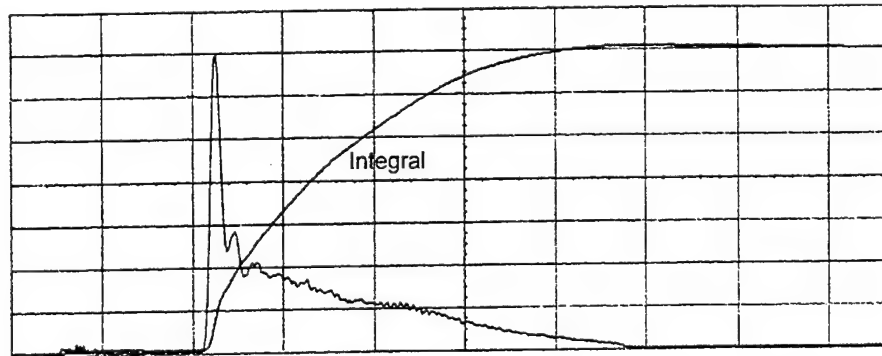

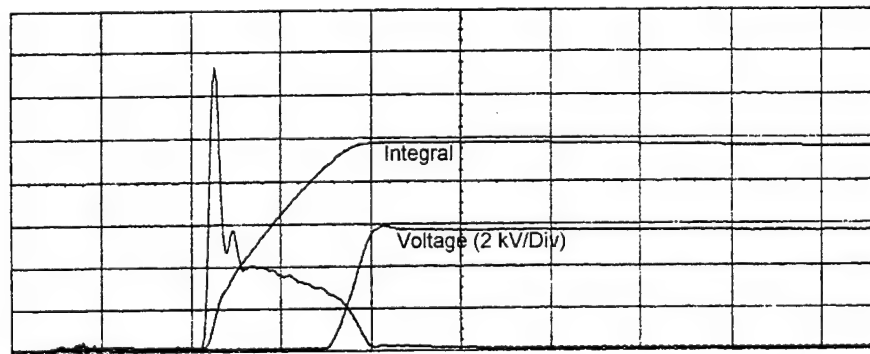Figure 3-25. Typical output pulse profile, timebase 500 nsec/Div.

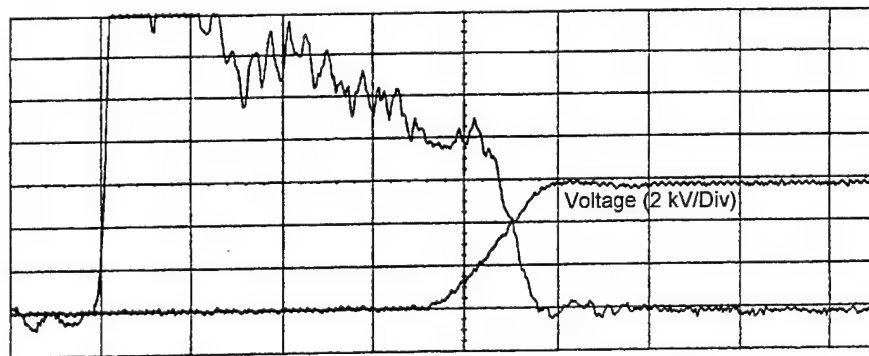Figure 3-26. Output pulse with tailchopping, timebase 500 nsec/Div.

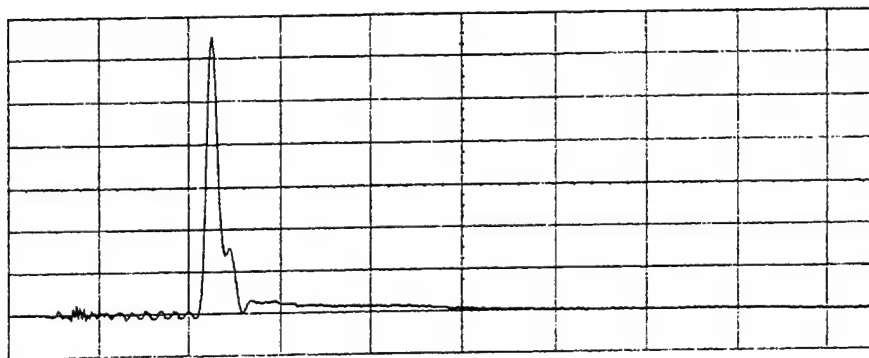Figure 3-27. Chopped pulse with high resolution, timebase 200 nsec/Div.

Figure 3-28. Chopped pulse with spike only, timebase 500 nsec/Div.

3.1.8 Catalyst

This section contains a description of the FAL catalyst system, including design approach and test results. The design was based on work previously conducted under a Hughes Independent Research and Development program in which a catalyst preparation, activation, and test station was developed; a simple engineering model was formulated relating catalyst parameters to the net CO_2 recombination rate; and in which the model was verified in a testbed laser. These efforts are also summarized as they relate to FAL.

In TEA lasers, the discharge decomposes CO_2 by electron bombardment, generating CO and O_2 among many other products. If allowed to build up to an appreciable extent, these products lead to discharge arcing; and output power is reduced due to loss of the CO_2 lasing species. For the FAL, it was found essential to have a catalyst module located directly within the primary laser gas flow to maintain an arc-free discharge and stable output pulse energy at high repetition rates. In the absence of a module, the discharge remained stable for about 4 sec at a 200 Hz repetition rate with 40 % duty cycle; however, with a module, the discharge remained stable for 30 hours of continuous running, with testing terminated by the operator not by discharge degradation. In other tests, an external catalyst module contained in an auxiliary flow loop was not found to be effective in controlling gas chemistry at high pulse repetition rates.

Design and diagnostics

The catalyst module is shown schematically in Figure 3-29 in relation to the heat exchanger to which it is attached. The primary gas flow is partitioned between the heat exchanger and catalyst module by the relative parallel pressure drops they present to the flow, and this was adjusted so that approximately 10% of the flow passed through the catalyst. The module extended the full length of the discharge electrodes and could accommodate 300 cm^3 of catalyst, although 200 cm^3 was typically used. The primary type of catalyst was in the form of 0.1 in diameter by 0.2 in. long pellets, but a secondary type in the form of 0.15 in. diameter spheres was also used.[8] An upstream nichrome wire heater was incorporated into the catalyst module to aid in activation of the catalyst within the laser and to elevate the catalyst temperature during laser operation. It was found necessary to operate the catalyst at temperatures around 40-65 °C in order to achieve the necessary net activity levels.
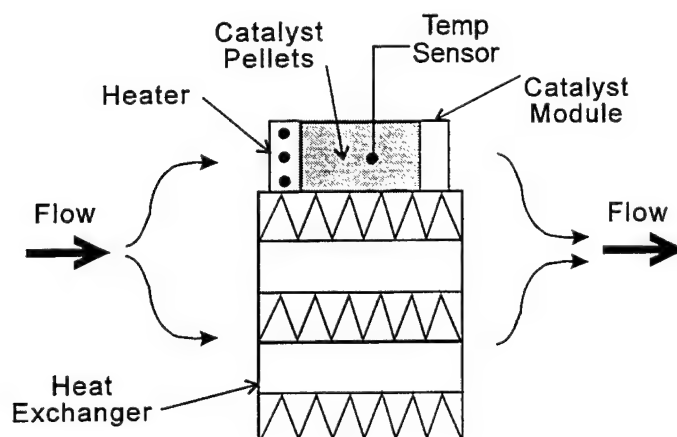

Figure 3-29. Catalyst module schematic.

The diagnostic setup is shown in Figure 3-30 and consisted of a CO monitor and temperature monitor with signals feeding into a two-channel chart recorder. The CO monitor consisted of a Beckman Industrial Model 880, infrared transmission instrument and stainless steel bellows pump. The pump circulated gas at a low rate from the laser to the monitor in a sealed flow loop constructed entirely of metal and glass to eliminate contamination. The sample gas flow rate and instrument sample period were such that the CO measurement risetime was on the order of 1 sec. Catalyst temperature was measured with a platinum resistance thermal detector (RTD) embedded in the catalyst volume. Temperature measurements were made through a connection to the basic laser power module with the buffered output to the chart recorder.
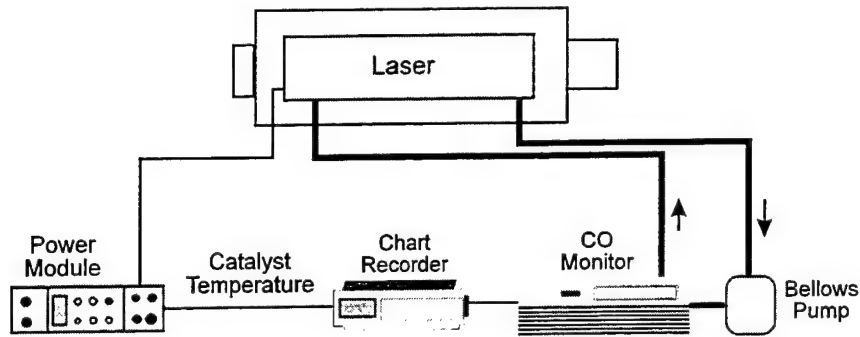
Figure 3-30. Catalyst diagnostics.

Model and test results

A catalyst engineering model was used to establish basic design parameters including catalyst volume, temperature, and gas flow rate. The model basically relates the time-dependent CO and O_2 concentrations to laser operating conditions. The CO and O_2 concentrations are desirable observables because of their experimental accessibility by standard diagnostics and suggestions from earlier work.[9] The relationship of concentration to catalyst parameters was established through classic analysis, verified by measurement and the relationship of concentration to laser performance was made empirically by determination of their relationship to arcing frequency.

The model is based on first order kinetics as determined from fundamental measurements using a flow-through reactor.[10] In that work, a carrier gas of known initial concentration was used and the CO and CO_2 levels were measured at the entrance and exit of a catalyst test cell as a function of flow rate through the cell and cell temperature. It was found that the usual plot of input and output CO concentrations versus flow rate showed a close fit to first order kinetic behavior for a one decade variation in flow rate. The first order kinetic equation relates the CO concentration ratio into and out of the catalyst module through the basic equation

$$x_2 = x_1 \exp(-k_1 V_c / Q_2) \tag{3-1}$$

where,

$x_1 =$ Mole fraction of CO entering catalyst module
$x_2 =$ Mole fraction of CO exiting catalyst module
$k_1 =$ First order kinetic rate
$V_c =$ Catalyst volume
$Q_2 =$ Flow rate through the catalyst

Temperature enters the formulation through the Arrhenius equation for the rate constant given by

$$k_1 = A \exp(-E_1 / kT) \tag{3-2}$$

42

where, E_1 is the activation energy and kT is the thermal energy at temperature T. Equation 3-1 is useful to show functional dependencies of the recombination rate on temperature. For purposes of calculation, experimental values for k_1 were used.

Two other equations are needed for the basic formulation. The first results from a mass balance analysis around the catalyst module and is given by

$$R_r = Q_2(x_1 - x_2) \tag{3-3}$$

where, R_r = recombination rate in the catalyst module. The final basic equation is simply the differential equation relating the net CO rate of change to the CO generation rate in the discharge and the recombination rate in the catalyst module. This is given by

$$V dx_1 / dt = R_p - R_r \tag{3-4}$$

where,

R_p = CO production rate in the discharge
V = Laser gas ballast volume

Eliminating x_2 from equations 3-1 and 3-3 and substituting for R_r in equation 3-4 gives

$$V dx_1 / dt = R_p - Q_2(1-a)x_1 \tag{3-5}$$

where,

$$a = \exp(-k_1 V_c / Q_2) \tag{3-6}$$

For the case of strict decay after a steady state concentration of CO has been established, $R_p=0$ and equation 3-5 reduces to

$$V dx_1 / dt = -Q_2(1-a)x_1 \tag{3-7}$$

The solution to equation 3-5 which describes the rise to steady state and the steady state condition itself is given by the simple exponential form

$$x = x^\circ \left[1 - \exp(-t/\tau)\right] \tag{3-8}$$

where,

$$x^\circ = \frac{R_p}{Q_2(1-a)} \tag{3-9}$$

and

$$\tau = V x^\circ / R_p \tag{3-10}$$

The solution to equation 3-7 is given by exponential decay as

$$x_1 = x^\circ \exp(-t / \tau) \tag{3-11}$$

The model was compared to measurements with FAL in which the CO level was monitored in its rise to steady state and in its decay after the discharge was turned off. The measurements were performed for the following conditions and parameter values:

Discharge energy = 6 J/pulse
Repetition rate = 200 Hz, 40% duty cycle
k_1 = 120 min^{-1}
R_p = 112 cm^3/min (80 Hz average repetition rate)
Q_2 = 5.5 x 10^4 cm^3/min
V_c = 210 cm^3
V = 7000 cm^3

The generation rate was measured by removing the catalyst and measuring the rise in CO level at a 1 Hz discharge repetition rate. A value of 0.71 cm^3/min was measured and is typical for this type of laser.[11] The kinetic rate was measured in a flow-through catalyst reactor.[10] The catalyst flow rate was measured with a hot wire anemometer.

A typical plot of CO percentage as a function of time during operation of the sealed laser for the conditions outlined above is shown in Figure 3-31. For the 80 Hz average repetition rate, the CO level is seen to reach steady state in about 2.6 min (12 k shots). At that point the discharge is turned off to observe the CO level decay which takes about 1 min. The form of the data appears nearly exponential, as expected; and the time constant and steady state CO values derived from the data are 22 sec and 0.5%, respectively. By fitting the exponential forms derived from the model, the calculated time constant and steady state values are 21 sec and 0.57%, respectively, in close agreement to the experimental values. Similar correspondence between measured and calculated quantities was found for catalyst temperatures from 40 °C to 70 °C and for peak discharge rates from 20 Hz to 200 Hz.
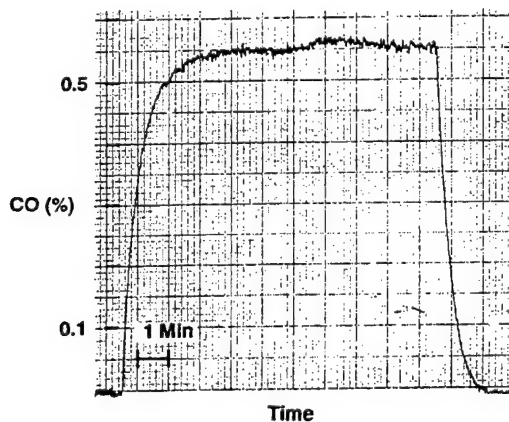

Figure 3-31. CO level versus time.

The behavior of laser output power was monitored for extended runtimes lasting several hours at an 80 Hz average repetition rate and for total shot counts on the order of 700 k. Two characteristics were observed (1) an approximate 5% drop in power over the first 5-10 min of

44

runtime and (2) a 15% further drop as the test progressed. The initial drop occurring over the first 25-50 k shots has been observed by others and is probably due to gas compositional changes.[9] The further 15% monotonic drop is probably not due to further gas dissociation effects, but rather to an increase in average gas temperature that would decrease laser gain. This is likely the case because pressure vessel temperature was found to rise even though catalyst temperature was held constant. Furthermore, the CO level was found to go to zero in about 1 min after discharge termination; but it required about 30 min of further cooldown before full output power could be regained.

Catalyst performance was monitored over periods as long as several months, but minor leaks in the pressure vessel precluded longer term observations. The CO level rise, steady state values and fall times were monitored for various repetition rates and no degradation of the catalyst was observed over the test periods. In addition, no degradation in the catalyst activity was observed in separate tests with the catalyst stored in sealed vials with the laser gas mixture for a period of six months.

3.1.9 Laser Operating Procedure

The laser operating procedure is shown in the diagram of Figure 3-32. Basically, it consists of setting up three modules. These are the Laser Control Electronics, Laser Power/ Signal Module, and the Computer, as described in detail in Section 3.1.4. There are two basic wait periods composed of the 5 min thyratron warm-up, after which the laser can be fired immediately at a 1 Hz repetition rate; and a 15 min catalyst warm-up for operation at high repetition rates. The computer is turned on after the Laser Power/Signal Module and can be set up during the warm-up period.

It is important to note that the catalyst heater and internal fan to which it is interlocked must be turned off to operate at a 1 Hz repetition rate. It is thought that discharge-generated gas species are required to serve as preionizers for discharge stabilization. For this reason, the first several discharges at 1 Hz are characterized by intermittent arcs, but this action leads to buildup of preionizers that soon stabilize the discharge. However, with the catalyst and internal fan on, the preionizers are recombined by the catalyst or on surfaces (due to the gas flow) and the 1 Hz discharge never stabilizes. Stabilization at 1 Hz is only achieved with the fan and catalyst off. At high discharge repetition rates, the first burst contains arcs but subsequent bursts are arc-free apparently because the preionizer generation rate exceeds the recombination rate. In general, with the catalyst and fan on for high repetition rates, the average repetition rate must be kept above about 20 Hz, taking into account the peak repetition rate of 200 Hz, the number of lines in a pattern, and the duty factor.

The first module to be set up is the Laser Control Electronics shown in Figure 3-33. There are four switches that must be set before applying power and these are numbered in the diagram. Their functions and positions are as follows:

| Switch	Function		Position
1	Tailchopper 28 Vdc input	Up: Down:	Voltage applied Voltage off
2	Laser fire fail-safe	Up: Down:	Laser allowed to fire Thyratron trigger disabled, command charge on
3	Internal /external trigger	Up: Down:	Internal trigger External trigger
4	Rep rate /catalyst heat	Up: Down:	1 Hz rep rate, catalyst heater and internal fan off High rep rate, catalyst heater and internal fan on
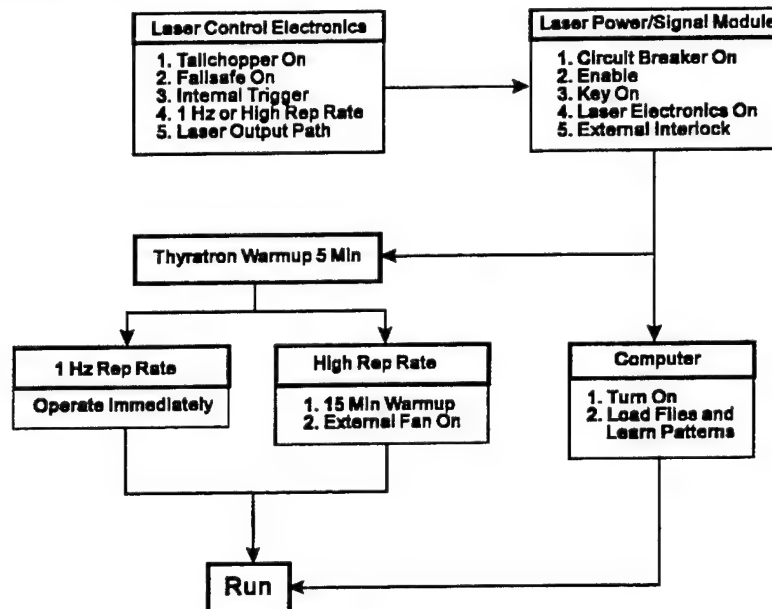
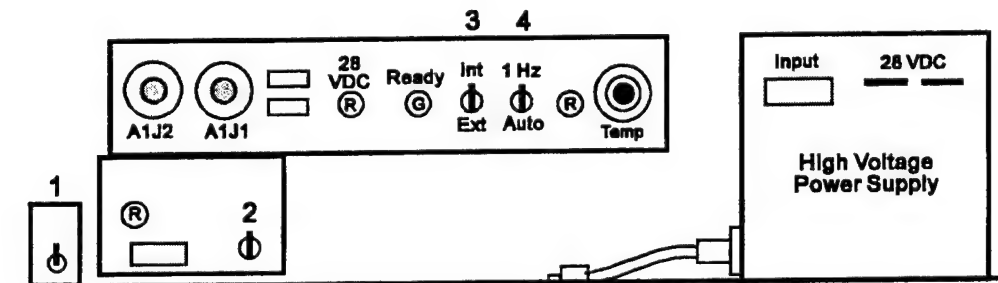Figure 3-32. Laser operating procedure.

Figure 3-33. Laser control electronics.

Switch #1 controls power to the high voltage pulser for the tailchopper and it is activated with the switch in the up position. Under conditions where alignment and calibration are being performed, it is desirable to turn off the tailchopper to conserve pulser lifetime and to prevent disturbance of calibration and the output waveform because of incorrect timing of the tailchopper.

Switch #2 is a fail-safe which blocks the trigger pulse to the thyratron. However, the command charge signal is still allowed and the capacitors can charge to full voltage. In the up position, the red light adjacent to the fail-safe switch is on indicating the laser is ready to fire.

Switch #3 controls the source of the trigger signal to start the laser charge and firing sequences. The Int position designates the internal trigger which is the normal case. In the Ext position, the laser electronics will accept an external trigger signal applied at the appropriate input on the laser power and signal module panel. It is used to fire the laser in the absence of the wavelength shifter.

Switch #4 selects either 1 Hz repetition rate operation or high repetition rate operation in the Auto position. With this switch in the 1 Hz position (and the catalyst heater and internal fan are turned off), it is still possible to program high repetition rate operation into the computer. In order to prevent damage to the laser electrodes in this case, circuitry has been included to limit the repetition rate to 1 Hz. In the Auto position, the adjacent red light is lit, and the catalyst heater and external fan are turned on.

At the time the Laser Power/Signal module is turned on, the red light comes on indicating that 28 Vdc is applied to the Laser Control Electronics. The thyratron warm-up then commences and after a period of 5 min, the green light comes on indicating the system is ready to fire at 1 Hz. If it is desired to fire at high repetition rate, and switch 4 is in the down position, the green ready light stays off for approximately 15 min until the catalyst reaches operating temperature. The catalyst temperature set point is determined by the Temp control at the far right of the control panel (in centigrade). Typical temperature set points are between 60 and 65 $^\circ$C. At approximately 55 $^\circ$C, the external heat exchanger fan comes on at a speed of 20,000 rpm.

With the laser control electronics set up, power is applied through the laser power and signal module shown in Figure 3-34. The various items on the control panel are referred to by their number and letter coordinates shown in the figure. The switch positions, functions, and indicating lights are as follows:

| Switch	Function	Position	Light
Circuit Breaker	Main power	Up-Power on, Down-Power off	1C-Red on
Interlock	Access doors	Connected-Laser enable Disconnected-Laser disable	2A-Green on
1B-Enable/Disable	Fail-safe	Up-Laser enable Down-Laser disable	1A-Green on
2B-Key	Parallel interlock	Clockwise-Laser enable Counterclockwise-Laser disable	2A-Green on
2D-Laser Elec On	Laser elec power	Up-Power on, Down-Power off	2C-Red on
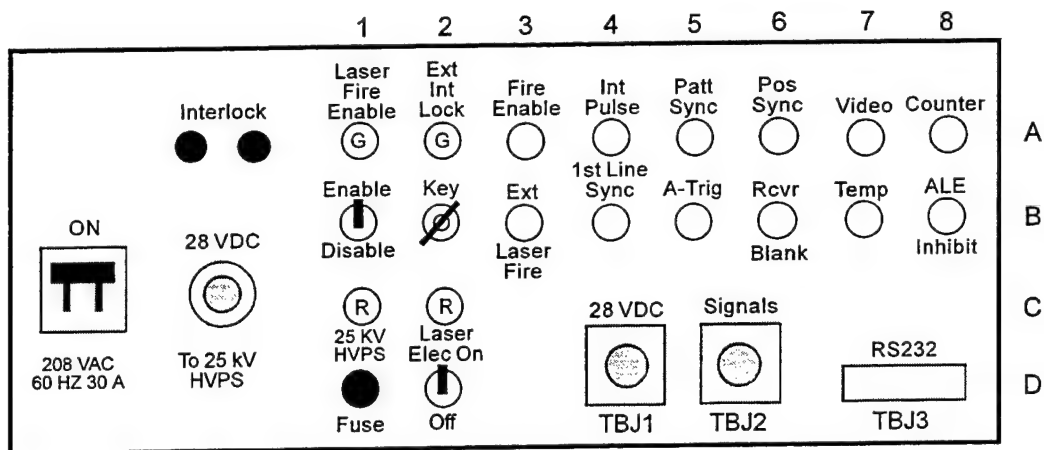
Figure 3-34. Laser power and signal module.

Power turn on proceeds by placing the switches discussed above in their on positions. The sequence is 2B-Key, 1B-Enable/Disable, Circuit Breaker, and 2D-Laser Elec On. Power is applied to all systems after the last switch, the laser electronics on toggle switch, is turned on. At that point, the laser begins to warm up and various diagnostic signals can be set up for monitoring.

Set-up of the computer for laser firing has been described in Section 3.1.6, Wavelength Selector. In summary, wavelength patterns, firing rates, pulse chopper timing, and discharge energy are selected through various menus. The start and stop of laser firing takes place through the R-Run and S-Stop commands in the main menu.

Power shut off requires that the wavelength shifter software be exited first, because the software requires that the wavelength shifter nonvolatile RAM be available for instructions. If power is shut off before this action, then changes to the files cannot be saved. Power shut-off proceeds by putting the laser electronics switch and the circuit breaker in the off position.

3.2 LASER TESTING

This section contains details of laser environmental and life testing. The environmental qualification included thermal cycling with laser operation in a combined laser diagnostic/thermal chamber setup. The shock and sine wave vibration tests were performed on an extensive array of equipment available in the Hughes Aircraft Environmental Engineering Department and under the supervision of that organization.

3.2.1 Introduction

After development of the first FAL, it was extensively tested (1) for qualification with respect to the functional requirements, (2) under various environmental conditions, and (3) for performance over a 50 million shot life test. Qualification testing involved monitoring laser output and condition while operating at full repetition rate and duty cycle for extended periods. This was done to determine overall laser capability. Subsequently, the environmental and lifetime test sequences were performed as outlined in Figure 3-35. The thermal test involved operation at
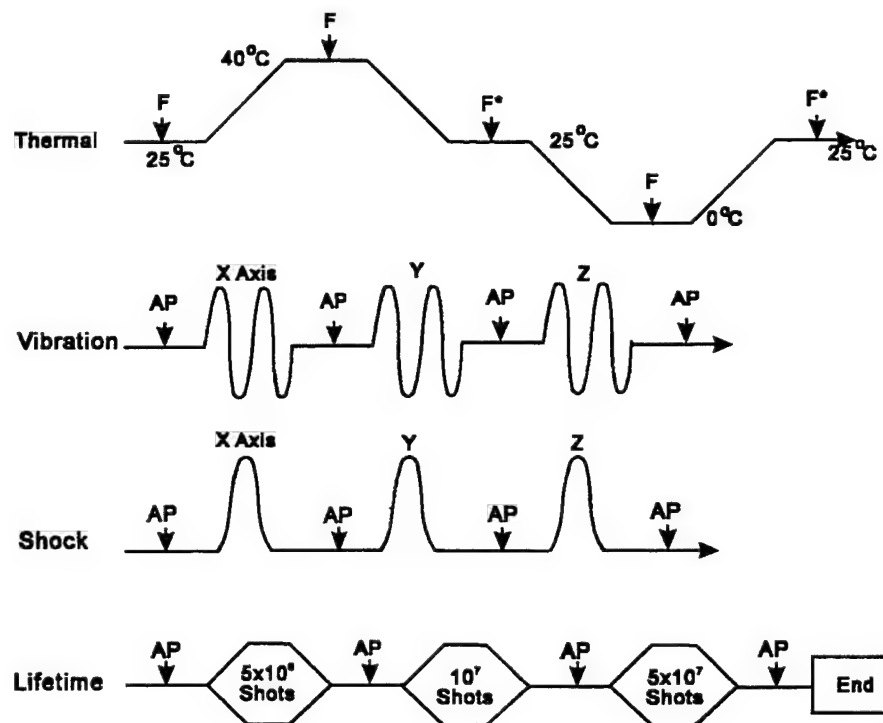
Figure 3-35. Environmental and test sequences.

0 °C, 20 °C, and 40 °C with a 4 hour dwell time and functional test (defined in Section 3.2.2) at each temperature. The functional test is defined by F (and its modified form by F*) in the figure and discussed in detail in Section 3.2.3. The vibration test was conducted with a ± 2 G sine wave sweep from 5 to 500 to 5 Hz along each axis and an average power test (defined by AP in the

49

figure) was performed before and after each sweep. The shock test involved a series of three, 3 G shocks in both directions of each axis with an average power measurement after each event. Following the thermal, vibration, and shock testing a qualification test was performed prior to lifetesting. Finally, life time testing was carried out with the goal of achieving 50 million shots with testing of laser output after every 5 million shots.

The FAL passed all tests successfully with the exception of optical damage found during testing. Specifically, the single, fully integrated and sealed laser was taken through qualification testing, environmental testing, and life testing without failure. In life testing it was operated to 53 million shots with testing terminated by the operator, not by any malfunction. After testing with this particular laser, several components were removed to aid in assembly of two more devices. This included the discharge module, high voltage module, and control electronics. These components were subsequently tested to 75 million shots without failure and their ultimate lifetimes are not known.

The first FAL was configured with a conventional optical resonator and ZnSe Brewster windows, as discussed in Section 3.1.5. The resonator was composed of an 86% reflecting output coupler with a beam cross-section of 1 cm x 1 cm and it was with this resonator design that optical damage was found to be the life-limiting problem. However, as discussed in Section 3.1.5, redesign of the resonator to incorporate a 3X intracavity beam expander and NaCl Brewster windows eliminated optical damage in further abbreviated life tests.

As discussed in Section 3.1.5, testing of the intracavity beam expander to 5 million shots has shown no indication of damage and extrapolations suggest that the lifetime of this component could approach the 100 million shot goal. S.A.T. has tested NaCl Brewster windows to 20 million shots under conditions similar to the FAL without indication of damage. Furthermore, as discussed in Section 3.1.5, it was found that wavelength selectivity of the laser was degraded for the 9R branch of the spectrum, possibly due to increased scattering from the copper turning mirror in the wavelength selector as a result of pitting over time caused by high intracavity flux. It was mentioned that the mirror may not have been optimum and that use of a mirror with different material and polishing specifications could extend its life. Testing in that regard has not been carried out. Finally, the lack of wavelength selectivity also led to redesign of the beam expander from a 3X to a 2X prescription, but this modification has not been tested. In summary, the new FAL optical designs appear to have solved the optical damage problem, although further testing is recommended. Aside from this issue, a failure mechanism has not been identified that would prevent achieving the 100 million shot life goal.

The main body of this section first contains details of the diagnostics setup and test approach. This includes a discussion of the laser parameters that were monitored and the measurement techniques. Results of the basic tests are then presented, including those of the initial qualification test; the environmental test composed of thermal, shock, and vibration testing; and the life test.

3.2.2 Test Approach and Diagnostics

Because of the large amount of data that were anticipated, measurements were tailored to the particular test condition. The conditions and measurables for each test are shown in Table 3-15.

Table 3-15. FAL test conditions and measurements.

Test Type	Test #	Condition	Test Outline
Initial Qualification	1	Lab conditions 1 Hz and Standard burst mode	• Arcing frequency • Output energy, 55 lines • Average power • 1 hour runtime, 2 weeks intermittent • CO percentage
Thermal	2	25 °C	• Functional
	3	40 °C	• Functional
	4	25 °C	• Energy, standard dev, 8 lines • Divergence 9P(20) and 9P(44)
	5	0 °C	• Functional
	6	25 °C	• Energy, standard dev, 8 lines • Divergence 9P(20) and 9P(44)
Vib/Shock	7	Static	• Average power
	8	Vibration, 3 axes	• Average power after vib each axis
	9	Shock, 3 axes	• Average power after shock each axis
Final Qualification	10	Lab conditions 1 Hz and Standard burst mode	• Arcing frequency • Energy, standard dev 16 lines • Divergence 9P(20) and 9P(44) • Average power • 1 hour runtime • CO percentage
Lifetime	11	Every 5×10^6 shots	• Arcing frequency • Average power

Standard burst mode is a benchmark operating condition defined as follows:

PRF	200 Hz
Duty cycle	40%
Average PRF	80 Hz
Wavelength shift rate	200 Hz
Wavelength pattern	16 lines

It was a benchmark operating condition consisting of a repeating burst of 16 different wavelengths, emitted at 5 msec intervals (200 Hz) with five bursts per second, giving an average firing rate of 80 Hz. This is shown schematically in Figure 3-36, where λ refers to the wavelength of a single output pulse. The 16 wavelengths sampled all four spectral branches and were specified as shown in Table 3-16. Table 3-16 also indicates (by an x) the specific measurements that were performed for each wavelength as part of the functional test indicated in each of the thermal test phases of Table 3-15. Note that the output pulse temporal shape and its divergence were sampled for only eight of the 16 available wavelengths. These were chosen to represent both a strong and a weak line for each branch.
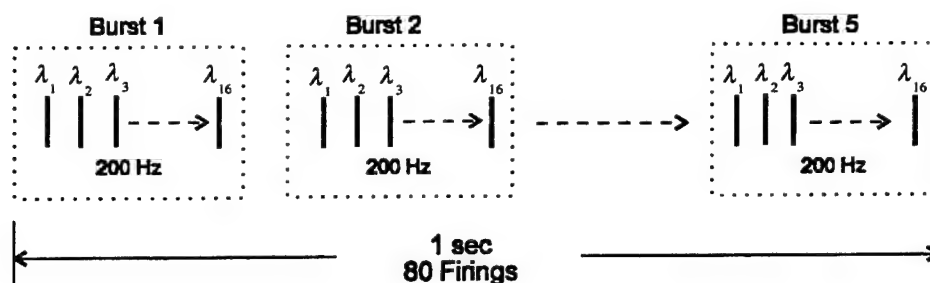
51

Figure 3-36 . Standard burst mode

Table 3-16. Wavelengths of standard burst mode and functional test outline.

Line	Ave Energy (mJ)	Stand. Dev (%)	Energy 250 nsec (mJ)	Energy 1 μsec (mJ)	Spike Width (nsec)	Diverg. (mrad)
9R30	x	x	x	x	x	x
9R20	x	x	x	x	x	x
9R10	x	x				
9P10	x	x				
9P16	x	x				
9P20	x	x	x	x	x	x
9P30	x	x				
9P44	x	x	x	x	x	x
10R32	x	x	x	x	x	x
10R20	x	x	x	x	x	x
10R10	x	x				
10R8	x	x				
10P8	x	x	x	x	x	x
10P10	x	x				
10P20	x	x	x	x	x	x
10P32	x	x				

The tests indicated in Table 3-16 involved seven basic measurements. These are shown in Table 3-17 with their specific diagnostic approaches. The fundamental measurement of laser performance was arcing frequency and this was determined by visual observation of the plasma discharge and by noting the number of arcs over a 10 sec interval. Under normal test conditions, arcing occurred approximately 0.1% of the time; and this would increase to 1% under the most adverse conditions, imposed by certain test procedures. Even at the highest arcing rates, there was sufficient time between arcs to allow accurate visual determination of frequency.

Temporal pulse profiles were obtained with a HgCdTe detector with a 15 nsec risetime and this was mounted to an integrating sphere in order to sample the entire multi-mode beam. The sphere diameter was 2 in. and provided a factor of 60 dB signal attenuation. This detector was also used with the digitizer and boxcar integrator for average energy and energy standard deviation measurements.

Table 3-17. Measurement methods.

Measurement	PRF (Hz)	Approach	Equipment
Arcing frequency	1-200	• Visual observation-highly accurate, typically one arc every 10 sec at 80 Hz average PRF	
Output energy per line	1	• Joulemeter • Digital oscilloscope with integrating function	Gentec ED 200 Tecktronix 466 HP 54111D
	200	• Digital oscilloscope with integrating function • Digitizer and boxcar integrator	
Energy average per line and stand deviation	1	• Pulse processor	Gentec PRJ-M
	200	• Digitizer and boxcar integrator	
Beam profile and divergence	1	• Pinhole scan with pyroelectric detector	
		• IR camera, resolution 63 μm	Insight Visions 83
Average power over all lines	50-200	• IR absorber/thermocouple	Scientech 365
Temporal profile	1-200	• Room temperature HgCdTe detector with integrating sphere, 75 MHz bandwidth	SBRC Labsphere 2 in. diam
CO level	1-200	• IR transmission cell in external flow loop	Beckman 880

Near and far field beam profile measurements were made by two methods. First, a pinhole was scanned across the beam to give an absolute measurement of the intensity profile with wide dynamic range detection. For all measurements, the pinhole diameter was 0.3 mm. In the near field, the laser beam diameter was approximately 1 cm and in the far field it was about 1 mm. Therefore, the ratio of beam diameter to pinhole diameter was 33 for the near field case, giving good spatial resolution. For the far field case, this ratio was 3; therefore, the pinhole scan was used only as an indicator of far field measurements and more precise measurements for purposes of determining divergence were carried out with an IR camera. The IR camera had a resolution of 63 μm, giving a beam diameter to resolution element ratio of 16.

In addition to the issues of resolution, the two methods of beam profile measurement were also fundamentally different in that the pinhole scan required multiple shots to complete; whereas, the IR camera could obtain an entire profile on only one shot. It was found that the mode spatial profiles were relatively steady from shot-to-shot, so that the multi-shot method of measurement was fairly reliable. The IR camera furthermore required that the data rate be limited to 1 Hz because of the camera internal scan rates. The camera did not have the feature of single shot triggering and would have accepted all 80 laser pulses over a 1 sec interval. Therefore, it was necessary to develop a method whereby the laser discharge would fire at the burst rate of 200 Hz, 40 % duty cycle, but the laser emission rate would be limited to 1 Hz. This was accomplished by the techniques shown in Figure 3-37.
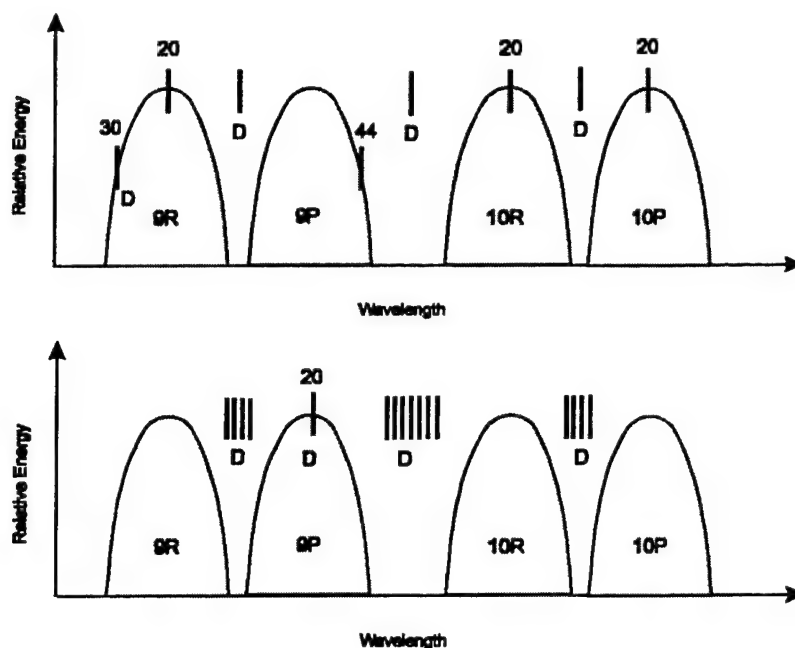
Figure 3-37. Schematic of the approach to achieve a 1 Hz lasing rate.

Figure 3-37 shows schematically the relative output energy versus wavelength for the four CO_2 emission bands and the vertical bars indicate the positions of wavelengths in the pattern. The top illustration shows the case relevant to measurements with the IR camera in which a single line (9R30 in this example) is allowed to lase at a 1 Hz rate while the laser discharge fires at a 100 Hz rate. For purposes of testing both the laser and the wavelength selector position accuracy, it was desirable to have the selector sweep over the entire spectrum and to have the discharge fire at 100 Hz. Because the wavelength selector is a resonant device that repeats patterns, it seeks addresses at its 200 Hz resonant frequency. Therefore, in order to achieve a 100 Hz firing rate, the discharge for alternate lines is turned off. The D indicated in the figure signifies that a discharge occurs for that particular wavelength. In order to prevent lasing on lines other than 9R30 for which a discharge occurs, the addresses for those lines are positioned in the clefts between the bands. It was not possible to fully suppress lasing by choosing addresses between lasing lines within the bands.

The bottom illustration in Figure 3-37 shows the situation where the repetition rate within a burst is at 200 Hz. and only the 9P20 line lases. In this case, all lines in the pattern fire and all lines other than the one desired are placed in the band clefts. The burst rate is reduced to 1 Hz for a net 1 Hz lasing rate.

3.2.3 Qualification Test

The qualification test was performed at several points in the latter stages of FAL development to provide a guide for modifications that were necessary to meet the functional requirements. This was necessary in order to enter into the environmental test phase. The

54

qualification tests were accomplished with the basic diagnostics setup shown in Figure 3-38. The equipment was aligned on an 8 ft x 10 ft optical bench. The dotted line shows the beam path for two colinearly aligned HeNe lasers that were used for boresighting the FAL and for alignment of the beam diagnostics with the FAL in place. The beamsplitter cube (BS Cube) provided the beam for aligning the joulemeter, power meter, HgCdTe detector, and spectrum analyzer. In normal operation with the FAL output beam, the BS Cube was removed. The joulemeter was removed for measurements with the other diagnostics.
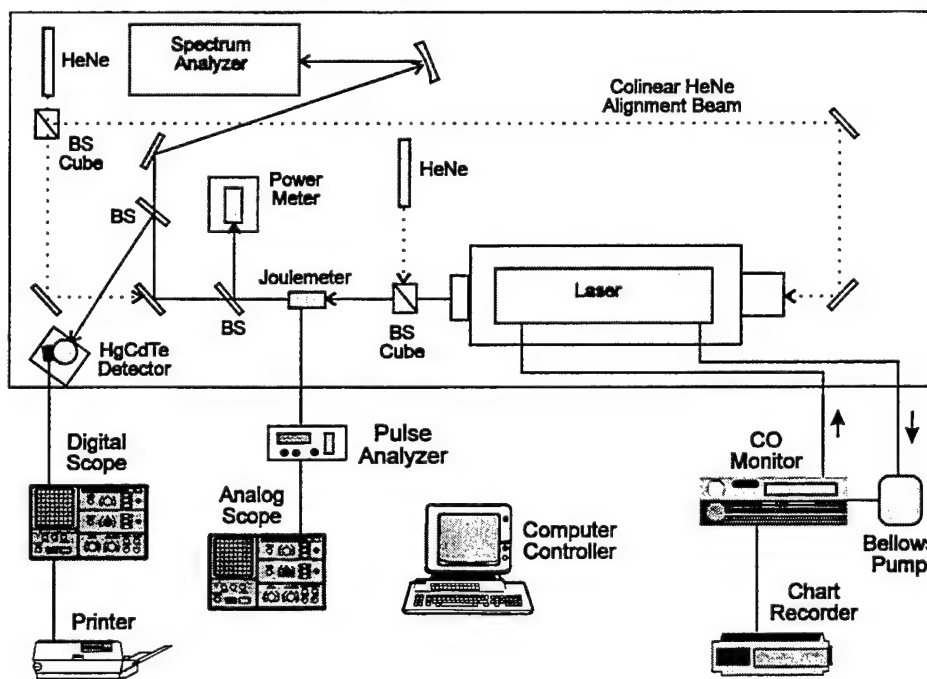
Figure 3-38. Qualification test diagnostic setup.

The joulemeter output entered a GenTec pulse analyzer used to provide energy standard deviation measurements for a 1 Hz repetition rate. This was followed by an analog oscilloscope in parallel to give a continuous readout of pulse energy on a shot-to-shot basis.

The HgCdTe detector output was fed into a digital oscilloscope to monitor output pulse shape. The oscilloscope had an integration function that was calibrated with the joulemeter and gave output energy at various points in the pulse. Typical traces are shown in Figures 3-25 and 4-45.

The CO monitor was described in Section 3.1.8 with respect to catalyst testing. Typically, a chart recorder was used to provide a continuous monitor of CO level for a variety of experimental conditions which included changes in catalyst amount, temperature, and gas flow velocity through the catalyst bed. Throughout the various developmental and qualification testing, efforts were made to correlate CO level with arcing frequency. As described in Section 3.1.8, it

was found that the CO level was always maintained below about 0.8% and that for this range of operation, arcing was not correlated with CO percentage.

Qualification testing was carried out by first establishing catalyst operating parameters that gave an arcing percentage of about 1% for short runs of 20 min in the standard burst mode. Then the laser was sealed and the arcing test was performed over a three day period with five starts from a cold condition each day. The laser was then kept sealed for one week and the laser was run for two hours each day over that period. Optimization was established by changing catalyst parameters and repeating the tests. The optimum laser conditions were found to be as follows:

Catalyst temperature	60 °C
Amount of catalyst	100 cm^3
Tangential fan speed	5000 rpm
Warm-up time	15 min
Heat exchanger fan speed	20,000 rpm

As discussed in Section 3.1.8 with regard to the catalyst, It was found through extended runtimes that laser output power would drop by 5% in the first 5-10 min, probably due to CO_2 dissociation effects. A further 15% drop occurred over one hour probably resulting from increased gas temperature as the pressure vessel and internal structure were heated. Results from the functional testing are shown below in the data tables related to thermal environment testing.

3.1.3 Environmental Test

Environmental testing was carried out in two stages with thermal testing first, followed by shock and vibration testing. Subsequent to this, the lifetest was carried out as described in Section 3.2.5. The laser was operated in a sealed condition throughout the entire series of tests which took about one month to complete. The laser did not experience any malfunction during testing and was fully operational at the conclusion.

Thermal test

Thermal testing was performed with the apparatus pictured in Figure 3-39. In Figure 3-39(a) is shown the thermal chamber situated to the left of a diagnostics table with an operator performing optics adjustment. A second operator is situated at the electronics rack performing tests with the IR camera and beam profiler system. Figure 3-39(b) shows details of the FAL mounted inside the thermal chamber.
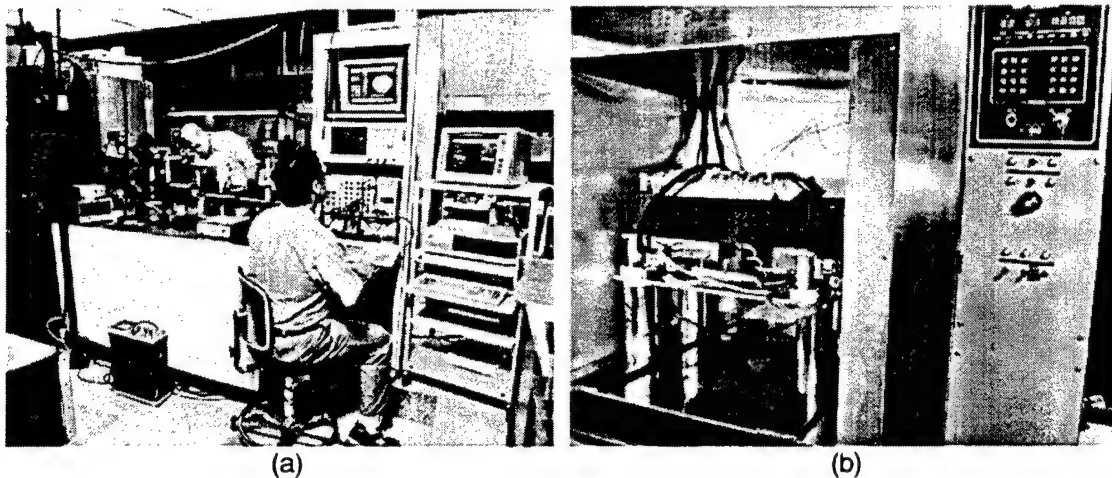
Figure 3-39. (a) Diagnostics setup and (b) thermal test chamber.

A schematic view of the diagnostics setup is shown in Figure 3-40. The laser beam exits the thermal chamber through an open port and is split at the first optic into one leg that is routed to the spectrum analyzer and the IR camera. The second leg propagates to the power meter, joulemeter, and HgCdTe detector. The joulemeter was used for 1 Hz beam energy measurements only and as a calibrator for the integrating function on the digital oscilloscope that received output from the HgCdTe detector. The HgCdTe detector output was also routed to the electronics rack that contained the waveform digitizer and boxcar integrator for measurement of average energy and energy standard deviation at high repetition rate. The power meter was used for all high repetition rate tests to measure average power. The spectrum analyzer provided periodic monitoring of spectral content.
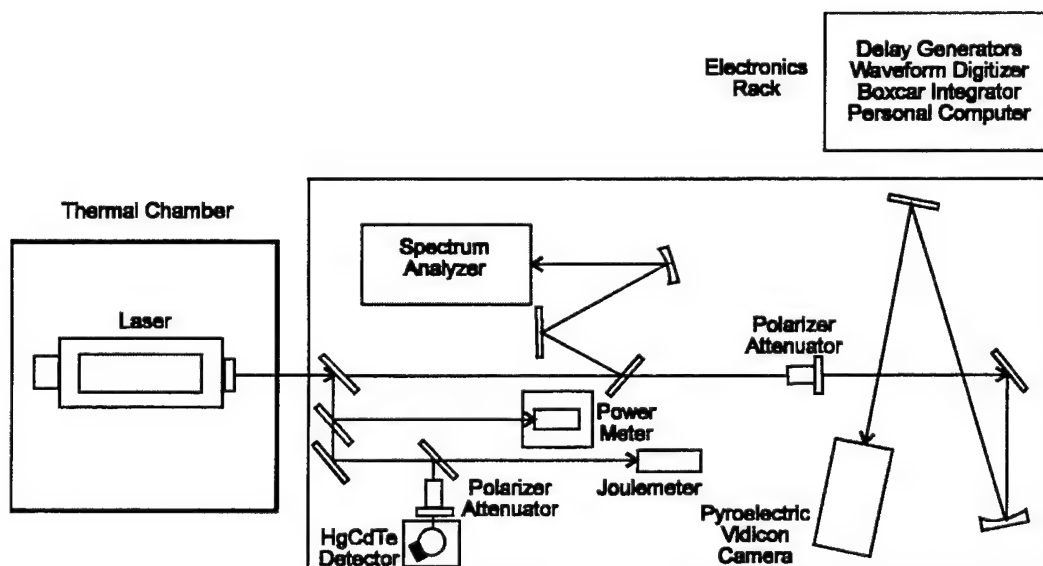

Figure 3-40. Thermal test diagnostics schematic.

The IR camera was placed at the focus of a 1m focal length parabolic mirror and was used for measurements of far field beam profiles for determination of mode structure and beam divergence. Beam divergence was obtained from the ratio of the $1/e^2$ focal spot diameter divided by the lens focal length. The far field beam diameter was 1 mm and the camera resolution was 63 μm. Figure 3-41(a) shows a black and white reproduction of a false-color image of the far field beam for the 9P20 line. The shading indicates the relative intensity levels which spanned a dynamic range of 20 in this case. Intensity plots of this image along the vertical axis (top trace) and along the horizontal axis (bottom trace) are shown to the right of the image. Intensity modulation in the horizontal direction is pronounced and shows the expected multi-mode beam structure. Measurements with the IR camera were carried out at an effective 1 Hz and the beam profiler software provided automatic calculation of beam divergence.
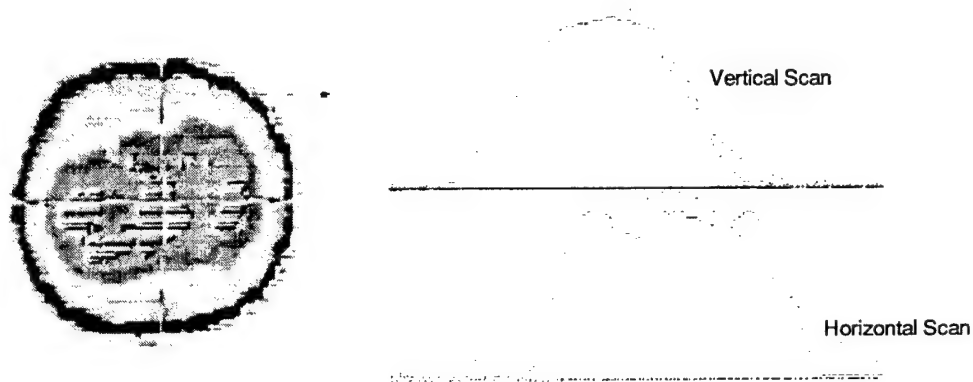
(a)
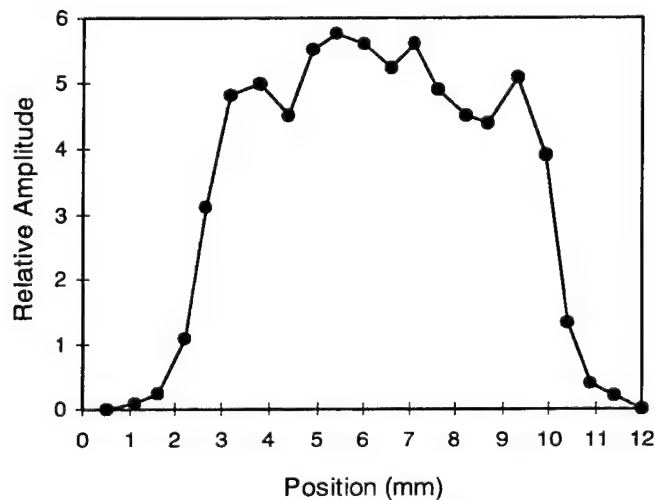
(b)

Figure 3-41. (a) IR camera far field profile and (b) near field pin-hole scan.

Pinhole scans were also carried out in the near field. In this case, a 0.3 mm diameter pinhole and pyroelectric detector were mounted to a translation stage and placed after the first beamsplitter on the diagnostics table. At this position, the beam had about a 1 cm diameter giving a ratio of beam to pinhole diameter of about 33. A typical trace for the 9P20 line is shown in Figure 3-41(b) in which the multi-mode structure is again discernible.

Laser performance was determined at three test temperatures in the sequence outlined in Figure 3-42. Benchmark operation was first determined at room temperature by performing an initial functional test. The thermal chamber was then elevated to 40 °C for a four hour dwell time to bring the laser to equilibrium, followed by another functional test. Following this, the chamber temperature was reduced to 25 °C and a functional test performed again. Testing at 0 °C was performed in the same fashion with four hour dwell times at each temperature and functional testing at each stage.
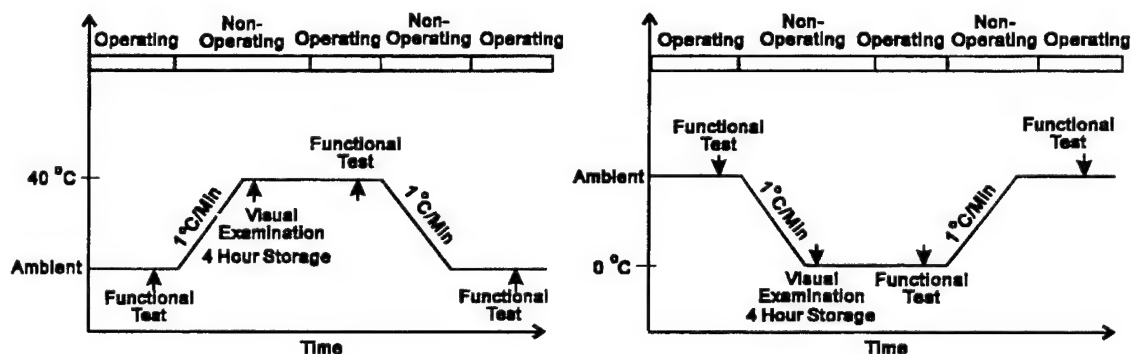

Figure 3-42. Thermal test sequence.

The results of the thermal testing are shown in Table 3-18 (25 °C), Table 3-19 (40°C), and Table 3-20 (0°). Note that all testing was performed at a 100 Hz discharge repetition rate and with an input voltage of 20 kV, with the exception of 9P44 which was operated at 25 kV. The average energy per wavelength indicated in the tables is plotted in Figure 3-43, parameterized by temperature. Finally, the average energy per wavelength for an input voltage of 20 kV and 25 kV is shown in Table 3-21 and plotted in Figure 3-44. The following observations can be made:

- Output energy increases with decreasing temperature, as expected for a CO_2 laser.
- The output energy at a temperature of 25 °C is greater than 120 mJ for all lines and is 140 mJ for the critical 9P44 line.
- The average energy standard deviation is about 5%, with a low of 1.5% and a high of 16% for all temperatures.
- The typical beam divergence is 3.5 mrad with a low of 2.9 mrad and a high of 4.5-5 mrad.
- Output energy increases with input energy, as expected.

Table 3-18. Functional test results-25 °C

Line	Ave Energy (mJ)	Stand. Dev (%)	Energy 250 nsec (mJ)	Energy 1 μsec (mJ)	Spike Width (nsec)	Diverg. (mrad)
			Input 20 kV (*25 kV), 100 Hz rep rate			
9R30	150	1.5	61.2	128.6	125	3.5
9R20	190	2.9	74.1	150.6	175	3.4
9R10	170	1.5				
9P10	175	2.2				
9P16	190	1.3				
9P20	200	2.7	76	170.2	160	4.2
9P30	180	2.1				
9P44*	140	10	56.8	123	185	2.9
10R32	150	4.9	79.4	134.1	140	3.5
10R20	200	5	91.7	176.7	130	3.6
10R10	190	11				
10R8	170	6				
10P8	160	11	57.3	109.4	100	3.6
10P10	170	9				
10P20	180	7.6	79.8	151.4	100	3.6
10P32	120	7.9				

Table 3-19. Functional test results-40°C.

Line	Ave Energy (mJ)	Stand. Dev (%)	Energy 250 nsec (mJ)	Energy 1 μsec (mJ)	Spike Width (nsec)	Diverg. (mrad)
			Input 20 kV (*25 kV), 100 Hz rep rate			
9R30	130	3.6	62.9	115.3	135	4.5
9R20	165	2	73.3	143	150	5
9R10	160	3.4				
9P10	156	1.2				
9P16	153	3.4				
9P20	175	1.4	80.4	153	115	3.9
9P30	168	4				
9P44*	115	11	63.9	108.6	170	2.9
10R32	130	8.6	61.6	112.2	140	3.2
10R20	175	7.4	86.7	157	150	3.8
10R10	160	11				
10R8	158	3.7				
10P8	140	10	80.8	131	105	2.9
10P10	138	4.8				
10P20	160	10	72.3	137.6	85	3.5
10P32	118	10				

Table 3-20. Functional test results-0°C

Input 20 kV (*25 kV), 100 Hz rep rate						
Line	Ave Energy (mJ)	Stand. Dev (%)	Energy 250 nsec (mJ)	Energy 1 μsec (mJ)	Spike Width (nsec)	Diverg. (mrad)
9R30	195	4.7	83.6	176.4	150	3.7
9R20	235	5	103.8	213.1	150	3.8
9R10	184	5.3				
9P10	210	3.8				
9P16	195	5				
9P20	245	4.8	122.5	230.3	120	3.6
9P30	215	4.1				
9P44*	160	15	80	152.9	200	3.2
10R32	170	7.7	83	162.1	130	3.3
10R20	225	4.7	109.6	207.7	125	3.4
10R10	219	18				
10R8	205	5.5				
10P8	170	23	84.2	154.7	130	3.4
10P10	213	4.7				
10P20	215	16	97.6	182.2	100	3.4
10P32	144	5.3				
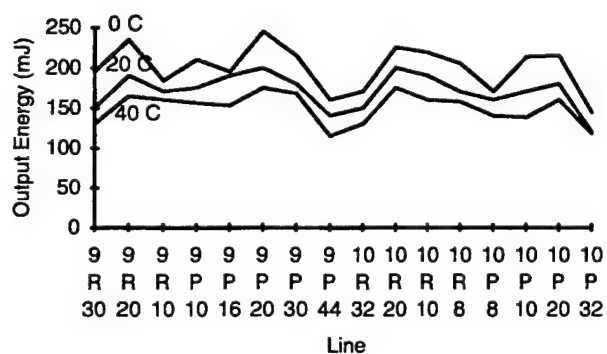
Figure 3-43. Output energy versus line for thermal test.

Table 3-21. Output energy for 20 kV and 25 kV input voltages.

Line	Ave Energy (mJ)	
	20 kV	25 kV
9R30	150	230
9R20	190	270
9R10	170	240
9P10	175	250
9P16	190	270
9P20	200	280
9P30	180	270
9P44	80	140
10R32	150	230
10R20	200	280
10R10	190	260
10R8	170	230
10P8	160	220
10P10	170	240
10P20	180	270
10P32	120	190
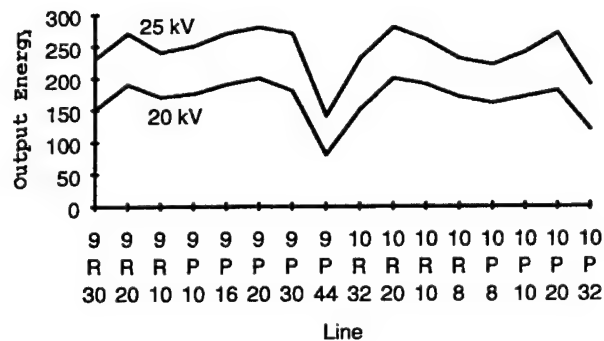
Figure 3-44. Output energy versus line for 20 kV and 25 kV input voltages.

Shock and vibration test

The shock and vibration testing was carried out on equipment that allowed for programming of specific mechanical waveforms. A picture of the apparatus is shown in Figure 3-45. Motion along all axes was monitored with accelerometers. The specific test conditions programmed into the equipment are shown in Table 3-22. The shock waveform applied to the apparatus is shown in Fig. 3-46(a) where the amplitude is 2.856 G and the timebase is 10 ms/Div. The vibration amplitude versus frequency are shown in Figure 3-46(b).
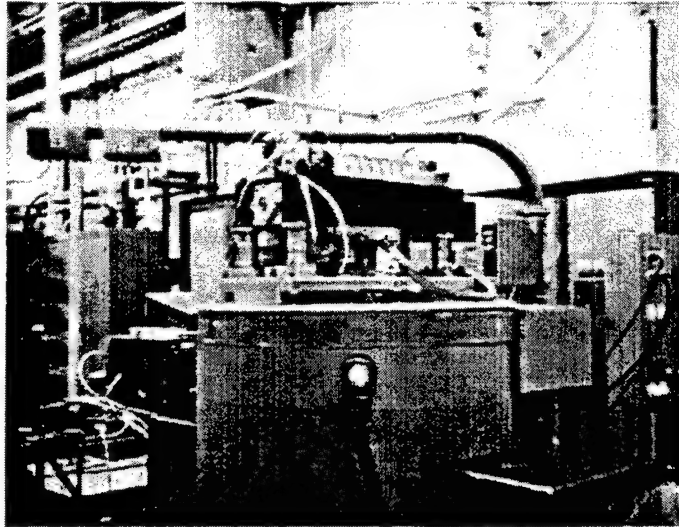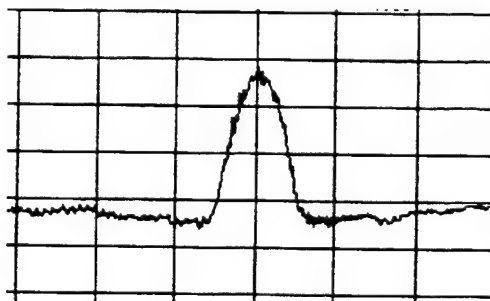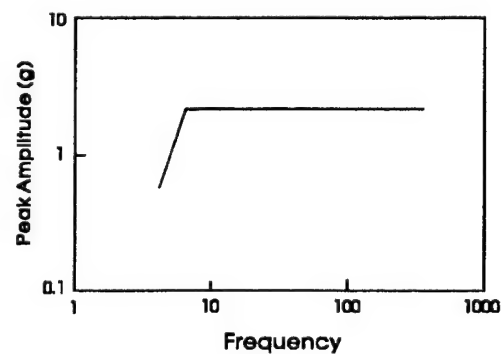
Figure 3-45. Shock and vibration test equipment.

Table 3-22. Shock and vibration test conditions.

Shock	
No. of events	3 shocks, both directions, each axis
Amplitude	3 ± 0.3 G
Duration	11 ± 1.1 msec
Pulse shape	Half-sine
Vibration	
Frequency sweep	Log sweep $5 \rightarrow 500 \rightarrow 5$ Hz
Duration	20 min/axis
Waveform	Sine wave
Amplitude	± 2 G

(a)

(b)

Figure 3-46. (a) Applied shock waveform and (b) vibration amplitude versus frequency.

The shock and vibration test procedures are shown in Figure 3-47. Functional tests were conducted before and after the entire test sequence for both shock and vibration. Between each axis shock or vibration test, an average power measurement was performed. The laser was not in an operating mode during shock or vibration. The vibration test was the most severe with the equipment making excursions as large as 1 cm and the acoustic energy that was generated required that ear protection be worn in the test area. No failures were noted.
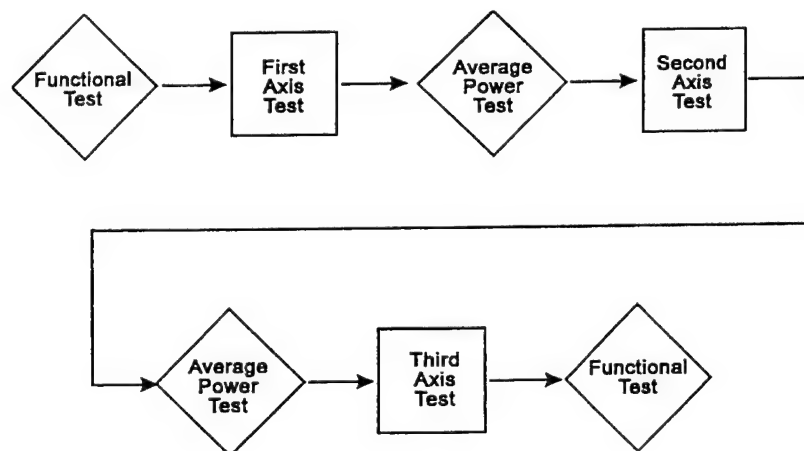
Figure 3-47. Shock and vibration test sequences.

3.1.4 Life Test

Life testing was conducted with the Qualification test diagnostic setup shown in Figure 3-38. The test conditions were as follows:

Gas/vessel condition   Sealed
Test duration   27 days
Starts/stops   32
Runtime/day   12 hours
Repetition rate   200 Hz
Duty cycle   30%
Wavelength shift rate   200 Hz
Number of lines   16
Charge voltage   20 kV
Output coupler   85% Reflectivity, 1 cm dia
Brewster windows   ZnSe

Early in the lifetest, after about 3 million shots, the conventional ZnSe output coupler showed damage to the extent that laser output was compromised. After about 5 million shots, both ZnSe Brewster windows showed damage, but of a nature different from that of the output coupler. These two findings were repeated in separate testing and are discussed fully in Section 3.1.5.

64

Because laser output was impaired by optics damage, laser output was not monitored during or at the completion of lifetesting. Rather, lifetesting was concentrated on other components, including the catalyst, flow system, discharge module, energy storage capacitors, high voltage switch, wavelength selector, and electronics. The lifetest results are summarized in Table 3-23. Note that the lifetest goal was 50 million shots and that testing was terminated by the operator at that point. Throughout the lifetest period, the number of starts/stops was approximately 32; and the last 100 hours of operation were continuous. The test results for some components with counts to 80 million shots (again terminated by the operator) were obtained in separate tests of those components for an additional 30 million shots beyond the 50 million shot goal.

Table 3-23. Lifetest results.

Component	Accumulated Shots (millions)	Status/Comments
Gas/Catalyst	53	Functional
Fan/Bearings	53	Functional, increased noise
Discharge Module	80	No change in voltage holdoff or arc frequency
High Voltage Capacitors and Potting	80	Functional
Thyratron	80	Functional
Wavelength Selector	80	Turn mirror reflectivity reduced
Control Electronics	80	Functional

Blank

4. SENSOR DEVELOPMENT

The sensor was developed primarily as a testbed for demonstrating chemical detection in the field with the high repetition rate FAL transmitter. In that respect, the design was guided by the need for easily modified components that were readily available and presented low schedule and technical risk. The design approach, therefore, did not favor size and weight reduction in relation to functionality and reliability, although efforts were made to produce as compact a system as possible. This approach resulted in a system that was shown to have good stability, low noise, and superior detectivity. The sensor was successfully tested in three separate field trials at Dugway Proving Ground, Utah. As a consequence of this experience, certain recommendations can be made regarding further development of the sensor in terms of reducing size and weight and improving performance. These are detailed in Section 6. The tasks of detailed analysis and publication of the field test data were undertaken by personnel at CBDC and are not included in this report.

The two major subsections that follow are 4.1, Sensor Description, which presents details of the sensor components, assemblies, alignment, and the operating procedure; and 4.2, Sensor Test Results, which presents details of calibration with a target of known spectral reflectance and details of experience with the hardware in the field.

4.1 SENSOR DESCRIPTION

4.1.1 Introduction

The sensor was designed to utilize a mixture of components that were both specially designed and commercially available, but with emphasis on the latter. In this way, cost was minimized while still meeting the functional and environmental requirements of fieldable hardware. In order to satisfy the requirements for performing field experiments, several pieces of diagnostics were included in the sensor design that could be eliminated in order to significantly decrease size and weight. These diagnostics included primarily an alignment HeNe laser, joulemeter, and spectrometer. All sensor components were mounted to a single side of an aluminum optical table for ease of alignment and modification for various experiments, and the table was mounted to a gimbal for pointing in azimuth and elevation. Sensor operation was supported by a 6 ft high equipment rack housing a power distribution panel, controls for a television camera, signal amplifiers and filters, data acquisition electronics, and an IBM-compatible computer. A picture of the fully integrated sensor mounted to the gimbal and with the data acquisition rack is shown in Figures. 4-1(a) and (b). The sensor specifications are summarized in Table 4-1 and discussed in detail in the appropriate sections below.
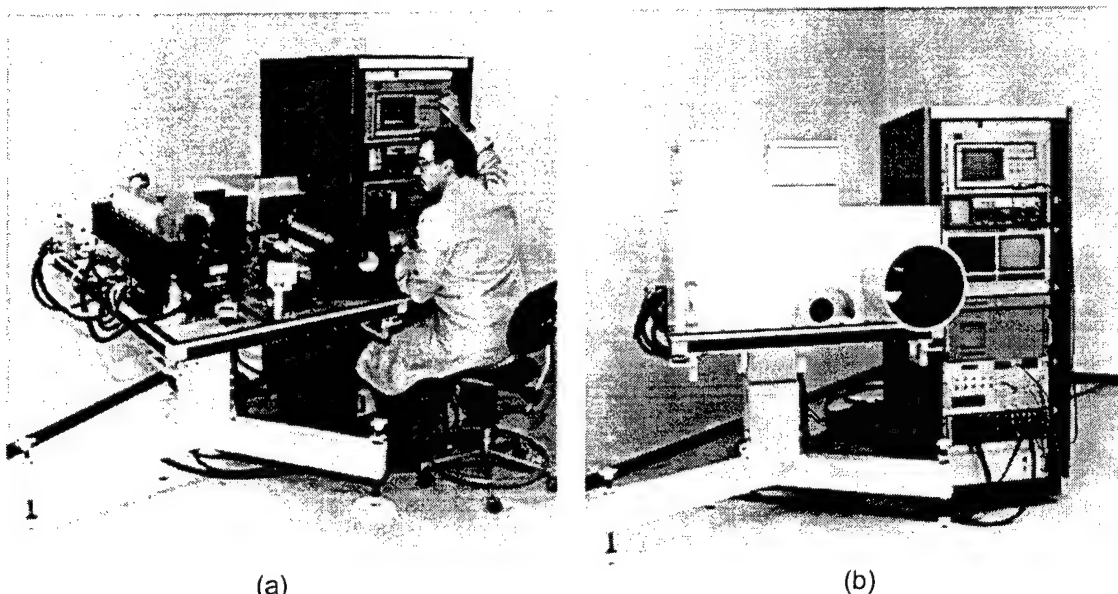
Figure 4-1. (a) Sensor with environmental cover off and (b) with covers in place.

Table 4-1. Sensor specifications summary.

Characteristic	Specification
Telescope	
Type	Cassegrain, afocal
Diameter	10 in.
Effective focal length	10 in.
Field of view	4 mrad
Detectors	
Transmit det type	TE-cooled photoconductive HgCdTe
Transmit det D*	1.94×10^8 cmHz$^{1/2}$/W
Transmit det size	100 μm square
Transmit det bandwidth	50 MHz
Receive det type	LN$_2$-cooled photovoltaic HgCdTe
Receive det D*	4.6×10^{10} cmHz$^{1/2}$/W
Receive det size	1 mm square
Receive det bandwidth	5 MHz
Transmit beam	
Repetition rate	200 Hz, 40% duty cycle
Output energy	>100 mJ, all lines
Divergence	3 mrad
Wavelength patterns	Max 20 lines/pattern, max 15 patterns
Gimbal	
Azimuth travel	± 90 deg
Elevation travel	-5 deg to +15 deg
Max speed	3 deg/sec
Height	32-36 in., adjustable
Weight	100 lb
Controller	Rack mount, 115 Vac, 3A

Table 4-1. Sensor specifications summary (Continued).

Characteristic	Specification
Data acquisition	
Analog-digital converter	Digital oscilloscope or PC card
Vertical resolution	12 bit
Sampling rate	30 MHz
Max segment size	4096
Max range	20 km
Record length	256 k
Max pattern at max range	62 wavelengths
Sensor	
Size	40 in. x 46 in. x 28 in., less gimbal
Weight	250 lb, less gimbal
Input power	208 Vac, 2 A; 110 Vac, 2 A

4.1.2 Layout and Gimbal

Subassemblies

The sensor system subassemblies and interconnections are shown in Figure 4-2 where two views of the sensor are presented to clarify these connections. All optical components and the laser transmitter are integrated on the optical table, attached to the top of the azimuth/elevation pointing gimbal. The electronic and electrical support equipment is contained in a 6 ft high equipment rack. This equipment includes (1) the Gimbal Power Amplifier, (2) the Laser Power/Signal Module (previously described in Section 3.1.4), and (3) the data acquisition electronics composed of an uninterruptible power supply (UPS), computer, monitor, and digital oscilloscope with external clock pulse generator. Power/bias supplies, preamplifiers, and temperature controllers for the transmit and receive detectors are located on the sensor optical bench next to the detectors. These subassemblies are described in detail in sections below. The remainder of section 4.1.2 is devoted to a description of major interconnections, mechanical details, and a description of the gimbal.

Electrical connections are made to the sensor table through three basic units. First, the Gimbal Power Amplifier is connected to the gimbal servo at the sensor through a 50 ft cable containing both power and signal leads. Second, the Laser Power/Signal Module is connected to the Laser Control Electronics through three power and signal cables as discussed in Section 3.1.4. Third, the Sensor Interface Unit is connected to the sensor optical table through four cables that carry (1) 28 Vdc and 110 Vac power, (2) control and video signals for the television camera, (3) the transmit signal from the transmit detector amplifier, and (4) the receive signal from the receive detector amplifier. Functional integration of the three control units is obtained through the computer and data acquisition systems as discussed below in Section 4.1.6.
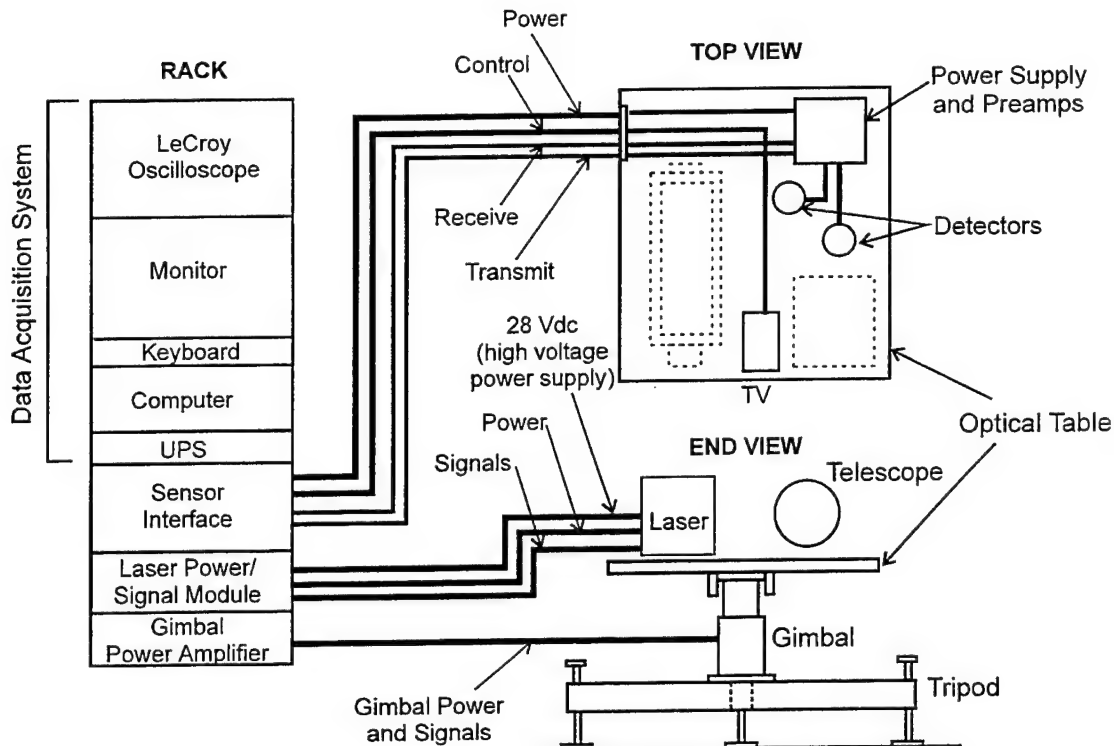
Figure 4-2. Sensor subassemblies and connections.

Mechanical details of the sensor assembly are shown in the front and top views of Figure 4-3. An aluminum EMI housing encloses the laser within the larger aluminum environmental cover that surrounds the entire sensor above the optical table to a height of 17 in. Both covers are demountable with quick-disconnect bolts. In addition to EMI shielding, the laser housing effectively separates air flow between the high capacity laser heat exchanger blower and the sensor optical and electronic components. Cooling air is introduced into the laser and sensor compartments through two separate fan and filter assemblies. One fan and filter assembly, measuring 12 in. x 24 in. x 11 in. high, directs air into the laser housing at 150 cfm through a filter with 90% efficiency for 5 μm particles. This airflow is exhausted out the side of the sensor cover that also provides access for the cables to the laser electronics. The other fan and filter assembly, measuring 12 in. x 12 in. x 11 in. high, provides cooling for the remainder of the sensor and it is exhausted through the telescope port which also helps prevent accumulation of dust on the telescope surfaces. The sensor environmental cover has a hinged hatch in the top for access to the transmit and receive filters and it has a telescope port extension and cover. Finally, a glass window covers the television port for sealing against the environment.
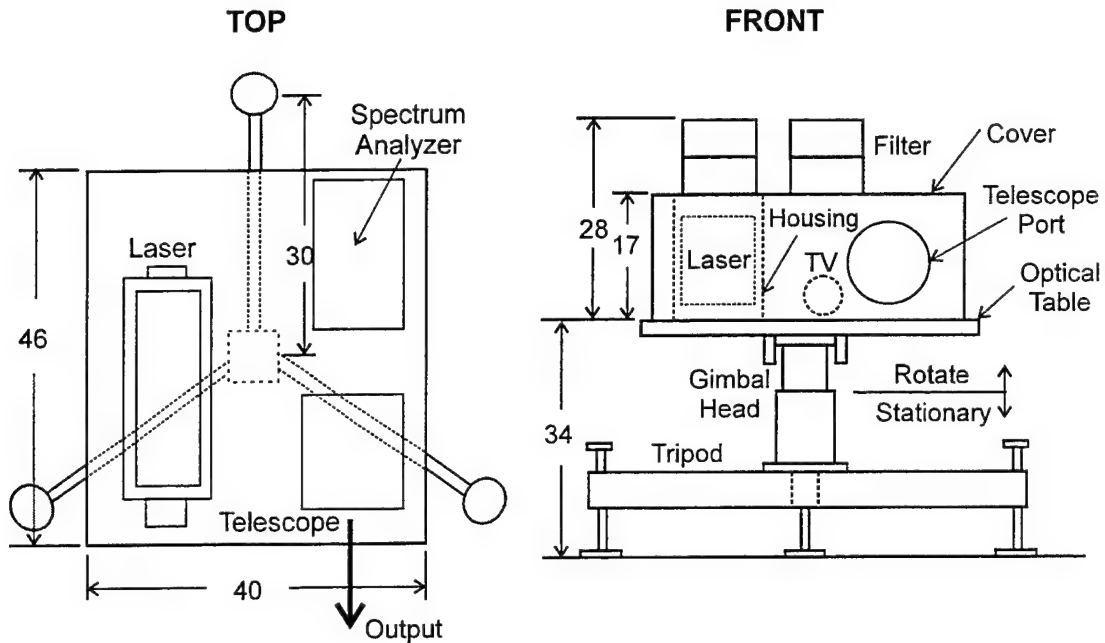
Figure 4-3. Sensor assembly dimensions (inches).

Gimbal

The gimbal system is composed of four elements, including (1) an IBM PC-compatible digital motion control (DMC) card that resides in the system computer, (2) a servo amplifier, (3) a gimbal head, and (4) a stationary tripod.[12] The assembly of these components is shown in Figures 4-2 and 4-3. Note that the gimbal head is composed of a stationary section, attached to the tripod, and a rotary part attached to the bottom of the sensor optical table. The gimbal moves the entire optical table in azimuth and elevation. The nominal gimbal height is variable within several inches of 34 in. by adjustment of the vertical tripod legs that rest on the floor.

A functional block diagram of the gimbal system is shown in Figure 4-4. The DMC card, which resides in the system computer, performs all the functions of motor control. These functions include generating motion profiles and position trajectories, decoding the encoder feedback and comparing it with the command position, stabilizing the servo system, outputting a motor command signal for driving the power amplifier, and providing error and status reporting. The Gimbal Power Amplifier amplifies the DMC command signals to the appropriate current levels necessary for driving each of the servo motors for azimuth and elevation control. The gimbal drive motors and encoder are contained in the gimbal head which is mounted to the tripod and carries the sensor table mounted to its top. The encoder provides position readout and, for noise immunity, differential inputs are used.
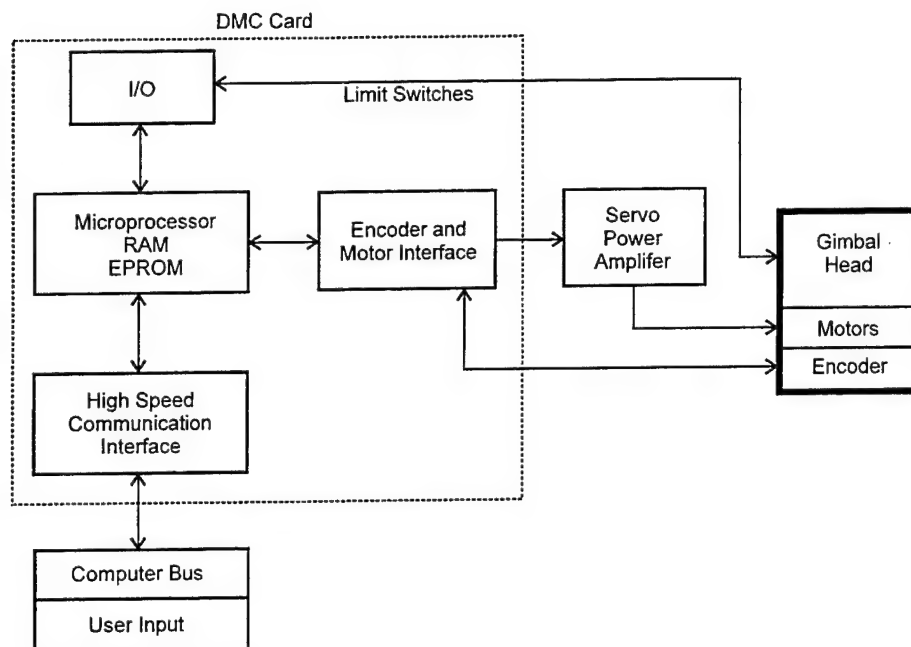
Figure 4-4. Gimbal functional block diagram.

Detailed specifications of the gimbal are contained in Table 4-2. Any position within the azimuth and elevation travel are accessible through inputs from the system computer and once a position is stored in memory, it can be repeated by the gimbal to within 0.01 deg accuracy (167 µrad) or about 6% of the transmit beam divergence. After a fixed position is accessed, a caliper brake is engaged to ensure that the position is held with no wander due to finite gear tolerances. Wobble due to imperfect gear mesh would degrade position accuracy to 0.1 deg. The brake is engaged 1 sec after a position is reached and is immediately disengaged when the command is given to move to a new position. Therefore, the gimbal system is suitable primarily for measurements along multiple, but fixed lines of sight. In the case of scan measurements made during gimbal movement, the pointing accuracy could degrade to 0.1 deg, or about 60% of the transmit beam divergence. For scans over several degrees, the 0.1 deg pointing accuracy would probably be sufficient. Design modifications to the gimbal gearing are possible that would result in a pointing accuracy of 0.01 deg even in the scanning mode.

Table 4-2. Gimbal characteristics.

Characteristic	Value
Azimuth travel	± 90 deg
Elevation travel	-5 deg to +15 deg
Max speed	3 deg/sec
Position repeat accuracy	0.01 deg
Position hold accuracy	0 deg with brake engaged
Height	32-36 in., adjustable
Weight	Head 70 lb, tripod 30 lb
Servo amplifier	Rack mount, 115 Vac, 3A

In operation, the servo amplifier is turned on, followed by the system computer. For safety reasons, a fail-safe toggle switch located on the gimbal head is left in the off position until the DMC card is successfully accessed and the message "caution, gimbal recentering to start" is displayed. At that point, the toggle switch is put in the on position, and the command to recenter the gimbal is given to the computer. If the gimbal had been left in a non-centered position at turnoff, it will reacquire the center position and at that time personnel must be made aware that the sensor table will begin moving. Further details of gimbal operation as it relates to data gathering are contained in Section 4.1.8.

4.1.3 Optical System

All optical components were integrated on a single optical bench of dimension 40 in. wide, 46 in. long, and 2 in. thick. The bench was made with aluminum face sheets and a lightweight honeycomb core and a matrix of tapped holes on 1.0 in. centers allowed for attachment of components. A schematic of the optical components integrated on the sensor optical table is shown in Figure 4-5. The beam emitted by the laser is optionally 3 x 3 cm square, if the intracavity beam expander is used, or it is 1 x 1 cm square if the beam expander is not used; and it is the former case which is described here. In that instance, the beam is turned and reduced (through element 2) to match the aperture of the CdTe crystals. After passing through the tailchopper composed of the CdTe crystals and ZnSe polarization analyzer, the beam passes through a splitter which diverts approximately 2% to a transmit beam monitor. The transmit beam monitor is composed of an integrating sphere and HgCdTe detector. A holder placed after the transmit beam monitor allows for beam intensity reduction using various ZnSe attenuators (element 7).
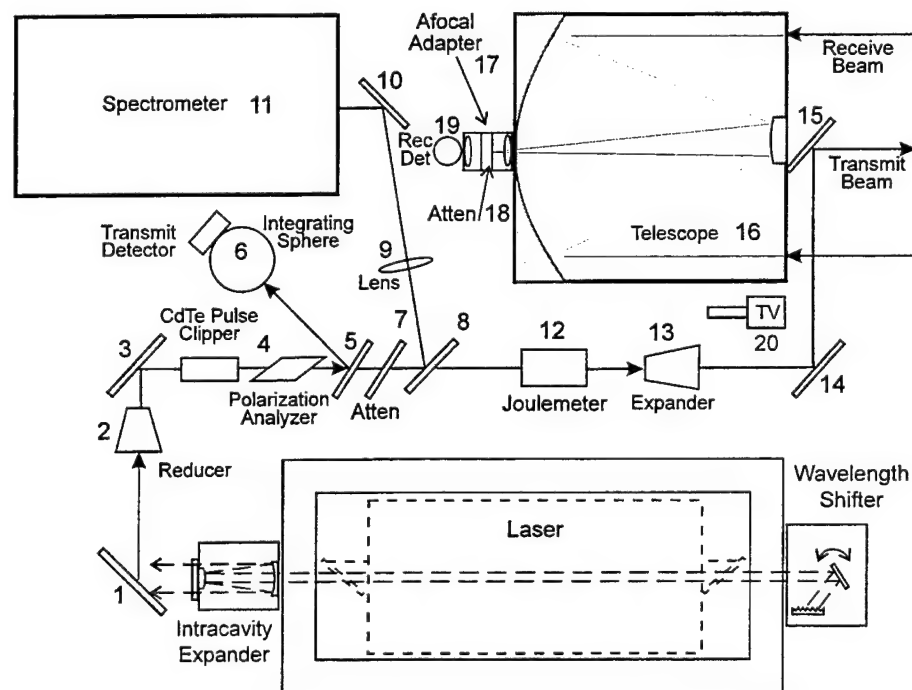
Figure 4-5. Sensor optical schematic.

73

In order to observe the emission spectrum, the option exists of inserting a total reflector in the beam path (element 8) on a kinematic mount to divert the entire beam to the spectrum analyzer. In a similar way, observation of total output energy is possible by insertion of a joulemeter on its kinematic mount (element 12). With these elements withdrawn in the normal data gathering mode, the beam is enlarged through the expander (element 13) and is propagated to the scene by the beam directing mirrors (elements 14 and 15).

The beam returned from the scene is collected by the Cassegrain telescope and focused through the primary mirror to an afocal region of 1 in. diam. The afocal section allows for insertion of attenuators or other optical elements without changing the focal spot position with respect to the field lens. The field lens then focuses the incoming radiation onto the receive detector.

The component specifications are summarized in Table 4-3. With respect to beam directing optics, flat total reflectors made of copper were generally used; and transmissive elements (aside from the tailchopper crystals) were made of ZnSe with broadband antireflection coatings, centered at 10.0 μm. Details of the telescope, beam reducer, and beam expander are presented immediately below. Optical details critical to sensor calibration are discussed further in Section 4.2.1.

Table 4-3. Sensor optical components.

	Component	Description
1	Turn mirror	Cu, flat, 4 in. diam
2	Beam reducer	ZnSe, AR coat, 3.6 x
3	Turn mirror	Cu, flat, 2 in. diam
4	Pulse clipper	CdTe crystals with ZnSe polarization analyzer, Section 3.1.7
5	Beam splitter	ZnSe, 2 in. diam, 5 % reflectivity, 25 deg angle of incidence
6	Transmit detector	Integrating sphere and TE-cooled HgCdTe detector
7	Attenuator	ZnSe, reflectivity=90%, 98.4%, and 99.4%
8	Total reflector	Cu, flat, 2 in. diam, kinetic mount
9	Lens	ZnSe, AR coat, focal length=10 in.
10	Turn mirror	Cu, flat, 2 in. diam
11	Spectrometer	0.75 m dispersion length, carbon observation screen
12	Joulemeter	GenTec model ED-200, 1 in. diam aperture, kinematic mount
13	Beam expander	ZnSe, AR coated, 2.3 x
14	Turn mirror	Si, flat, 2.5 in.x 3.5 in.
15	Turn mirror	Ge, 3 in. diam
16	Telescope	Cassegrain, 10 in. diam aperture x 10 in. tube length
17	Afocal adapter	Beam diam=1 in., 2 in. drift length
18	Attenuators	Ge, various ND 0.4 to ND 3.0, 4 pieces
19	Receive detector	LN$_2$-cooled, HgCdTe
20	Television	2/3 in. black/white, 10.5-105 mm zoom

Telescope

Design of the telescope was based on obtaining the largest practicable aperture and field of view consistent with the various receive detector characteristics required to achieve a detectivity exceeding 3×10^{10} cmHz$^{1/2}$/W and a signal bandwidth of at least 5 MHz. The motivation for large aperture was to maximize signal strength. A large field of view was necessary both to

satisfy the need for effective speckle averaging for near-range, strong signal, speckle-dominated conditions and to accommodate the 3 mrad transmit beam divergence.

The telescope and detector parameters are simply related for an ideal afocal Cassegrain as follows:

$$s = (f/\#)_{field} D(FOV)_{tel} \qquad (4\text{-}1)$$

$$\tan\left[\frac{(FOV)_{det}}{2}\right] = \frac{1}{2(f/\#)_{field}} \qquad (4\text{-}2)$$

$$M = \left[\frac{(FOV)_{tel}}{\lambda/D}\right]^2 \qquad (4\text{-}3)$$

where, s = focal spot diameter, $(f/\#)_{field}$ = f-number of field lens, D = telescope diameter, $(FOV)_{tel}$ = field of view of telescope, $(FOV)_{det}$ = field of view of detector, and M = number of speckle cells. Also, detector noise is proportional to s and detector bandwidth is proportional to $1/s^2$. (Field lens refers to the final element before the detector in the afocal section of the telescope.) In practice, the telescope was designed to have an $(FOV)_{tel}$ of 4 mrad in order to fully accommodate the 3 mrad transmit beam divergence. Furthermore, the afocal section of the telescope was made slightly converging (from 1 in. to 0.9 in diam over the 3 in. drift length) to provide a focal spot blur diameter of 0.76 mm. This allowed for a margin of misalignment for the 1 mm square detector element. The telescope and related detector parameters are summarized in Table 4-4.

Table 4-4. Telescope and related detector parameters.

Parameter	Value
s, focal spot blur diameter	0.76 mm
D, telescope diam	25 cm
$(FOV)_{tel}$, telescope field of view	4 mrad
$(FOV)_{det}$, detector field of view	53 deg
$(f/\#)_{field}$, field lens f-number	1.0
M, number of speckle cells	10^4
Detector diam	1 mm
Detector bandwidth	7 MHz
Detector D*	4.6×10^{10} cmHz$^{1/2}$/W

The telescope is shown schematically in Figure 4-6. It is composed of a 10 in diam primary mirror and a 2 in. diam secondary mirror. A total reflecting, flat mirror attached to the rear of the secondary mirror directs the transmit beam to the scene. The secondary mirror converges the beam to the afocal section where polarizers, neutral density (ND) filters, and a rotation stage can be placed. The space allotted for these elements is 5 cm in length and allows 2 in. diam elements to be inserted. At the rear of the afocal assembly is mounted the field lens that focuses the beam into the HgCdTe detector. The afocal section is demountable for telescope boresighting.
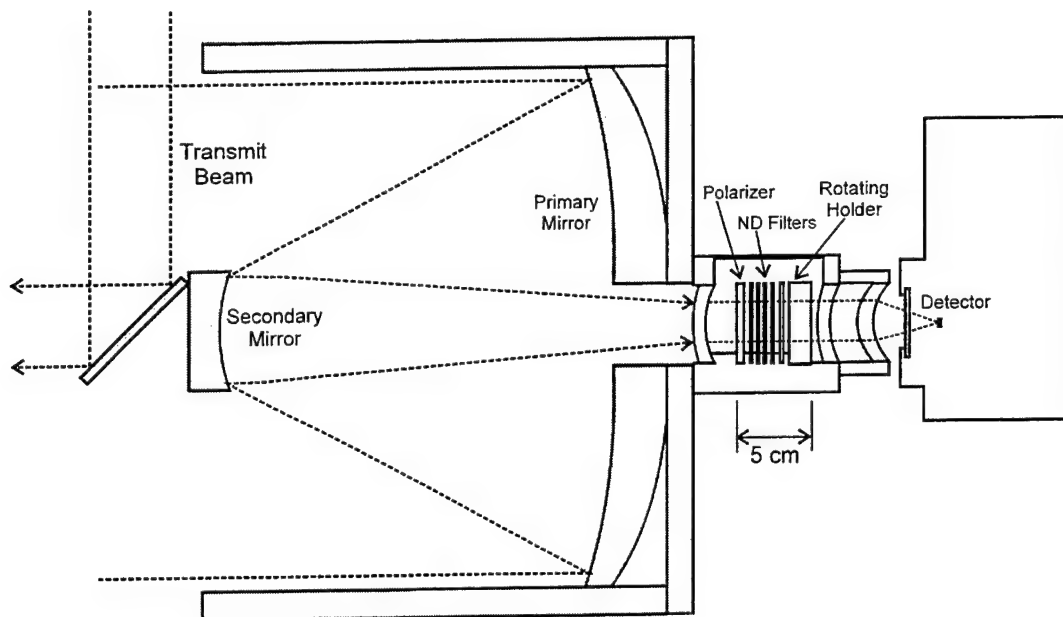
Figure 4-6. Telescope with afocal filter section details.

The transmission characteristics as a function of wavelength for the various telescope refractive elements are important for purposes of calibrating the absolute sensitivity of the sensor. Assuming that the primary and secondary mirrors are totally reflecting with no spectral dependence, the remaining elements are the three antireflection (AR) coated Ge refractive optics. The overall spectral transmission for these elements is shown in Figure 4-7.
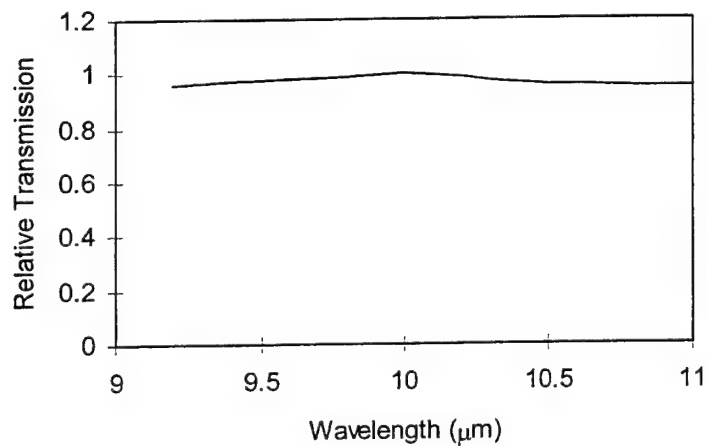

Figure 4-7. Telescope transmission versus wavelength.

Beam expander and reducer

As described with reference to Figure 4-5, a beam reducer and an expander are used at two points in the optical train. The reducer (element 2) is used to reduce the size of the output beam from the laser to accommodate the aperture of the tailchopper crystals. After passage through the tailchopper, the beam passes through an expander (element 13) in order to tailor the beam divergence to 3 mrad. Both the expander and reducer have the same outline as shown in Figure 4-7, where the direction of arrows are characteristic of beam propagation for the case of expansion. The design of each expander or reducer provides for a coarse adjustment in which the coarse adjust locking collar is loosened and the barrel containing the entrance optical element is moved with respect to the exit optical element. Fine adjustment of the optical element spacing is then made with a rotating fine adjust collar. The optical element spacing is adjusted so that the emitted beam is parallel which is equivalent to obtaining the minimum focal spot size in the far field with the sensor alignment and divergence measurement apparatus as discussed below in Section 4.2.2.
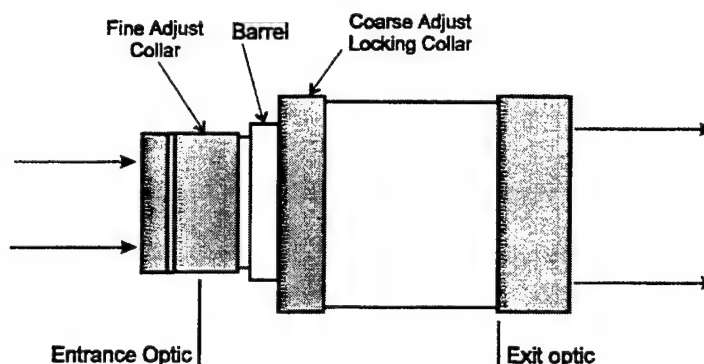

Figure 4-8. Expander schematic.

The laser intracavity beam expander produces a beam at the output coupler which is 3x3 cm square and this beam must be reduced to fit the 1x1cm square aperture of the CdTe tailchopper crystals. For an ideal Gaussian beam, the reduction ratio would be 3:1; but in the case of the multimode FAL beam it was found that a reduction ratio of 3.6:1 was necessary. With respect to the beam expander, it would normally be necessary with a Gaussian beam to have an expansion ratio of 1.7 to achieve a final transmit beam divergence of 3 mrad starting with a 1x1 cm square beam and a maximum single line divergence of 5 mrad. However, measurements showed that the multimode FAL beam required an expansion ratio of 2.3:1. For both the beam reducer and expander, the lens elements were coated with a broadband, AR coating, centered at 10.0 μm. Measurements showed virtually no change in transmission as a function of wavelength over the range 9.2 μm to 10.7 μm.

Optical alignment

Alignment of the optical elements on the sensor table shown in Figure 4-5 consisted of (1) boresighting the components in the transmit beam path, (2) aligning of the transmit beam with the telescope optical axis, and (3) centering of the transmit beam in the telescope field of view. Boresighting of the transmit beam with the various total reflecting mirrors and the beam

expanders/reducers was carried out simply by using a liquid crystal to indicate beam position on the mirror surfaces and within the apertures. This approach was facilitated by the available large clear apertures. In the case of the CdTe crystals for the tailchopper, which had a square aperture of 11x11mm compared to the 10x10 mm beam, fixtures were attached to the crystal mounts to indicate the crystal center and the beam center was aligned to those points.

Alignment of the transmit beam with the telescope optical axis was accomplished with the setup shown in Fig. 4-9. First, irises were aligned with the infrared (IR) transmit beam (shown as the dotted line) both on the sensor optical table and at a position about 5 m away. With the IR beam off, the irises were then used to coalign a HeNe beam with the IR transmit beam. Injection of the HeNe beam was accomplished with a cubic beamsplitter (Melles Griot, Inc.) that produced counter-propagating rays. Note that the beamsplitter is not transmissive to the infrared beam and that onced the iris positions were established, the infrared beam was no longer used. Second, the telescope field lens was removed and an alignment fixture was attached in its place. The fixture had a pinhole at a position coincident with the focal spot defined by the telescope primary and secondary mirrors. Third, a corner cube was placed just outside the final turn mirror so as to capture the emitted HeNe beam and reflect a parallel beam back into the telescope. Alignment of the transmit beam with the telescope optical axis required that the HeNe beam exit through the pinhole in the alignment fixture and this was accomplished by adjustment of the final turn mirror only.
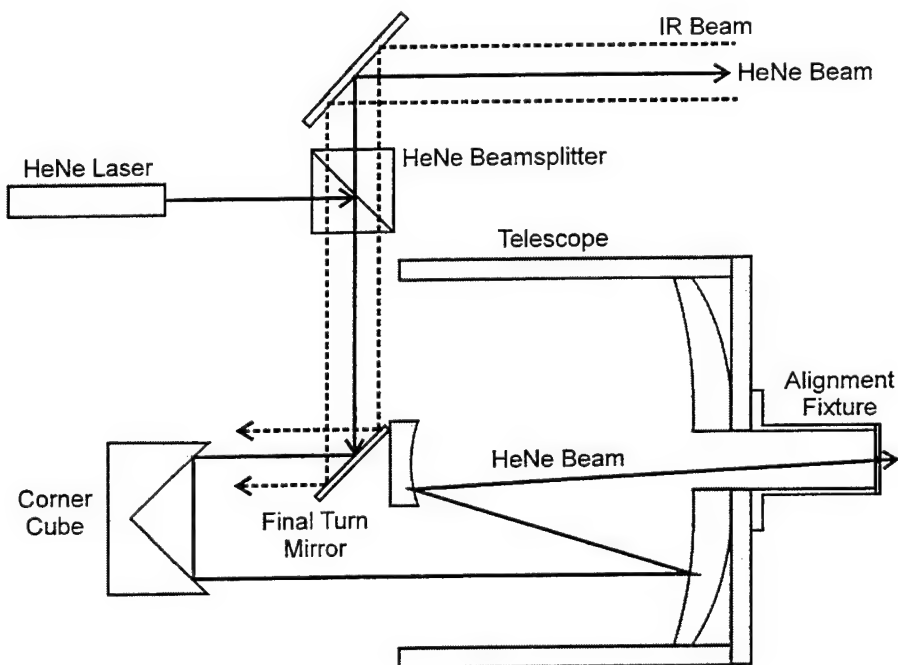

Figure 4-9. Transmit beam-telescope axis alignment.

Following alignment of the transmit beam with the telescope optical axis, it was necessary to align the transmit beam with the telescope field of view. This alignment was performed with the setup shown in Figure 4-10. Note that the transmitted beam had a divergence of 3 mrad, compared with the 4 mrad telescope field of view. With reference to the top diagram in Figure 4-

10, the transmit beam was first focused using a large diameter flat mirror and a long focal length mirror. Typically, the mirror diameters must be roughly twice the diameter of the telescope secondary and the focusing mirror should have a focal length of about 1 m. For a beam divergence of 3 mrad this produced a focused spot with a diameter of 3 mm. Conversely, measurement of the focused spot was used to determine the transmit beam divergence. Once the point of focus was determined (typically with burn patterns on thermal printer paper), a pinhole with diameter of 3mm was placed at that precise position.
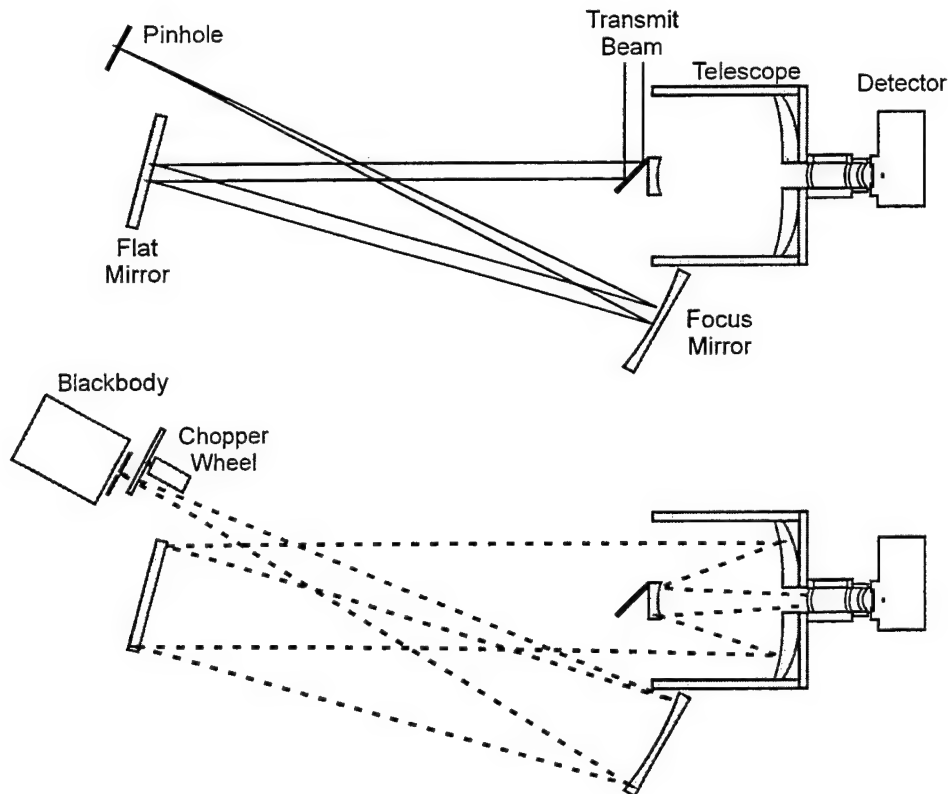
Figure 4-10. Transmit beam and receive field of view alignment.

After placement of the pinhole at the point of focus, a blackbody radiator was positioned behind the pinhole and a chopper wheel was placed in front of it as shown in the bottom illustration of Figure 4-10. The result was that an isotropic radiator now emitted from the far field focal point of the focused transmit beam. Divergent rays emitted by the blackbody at the focus of the collimating system (shown as dotted lines) were then refocused as parallel rays that entered the telescope and were focused at the detector. Alignment of the transmit beam and telescope field of view then proceeded by adjustment of the detector position micrometers to maximize the square wave signal produced by the chopper wheel. Turning optics in the transmit beam path could not be adjusted at this stage of alignment, because it would have caused misalignment of the transmit beam with respect to the telescope optical axis. This alignment technique was verified under field conditions by using reflection off targets located at ranges on the order of 1 km. It was found that only minor readjustment of the detector position was required to maximize signals. As a point of reference, Table 4-5 gives equipment parameters and signal values obtained with one typical setup. It should be noted that for quick verification of alignment and

simplicity of setup, a soldering iron could be used in place of the traditional regulated blackbody. In that case, a soldering iron at a temperature of about 800 °F placed behind the pinhole produced a signal on the order of 200 mV under otherwise similar conditions shown in Table 4-5.

Table 4-5. Typical alignment parameters.

Mirror diameter	6 in.
Mirror focal length	1.2 m
Pinhole diameter	2.5 mm
Blackbody temp.	400 °K
Optical atten.	ND 1.45
Oscilloscope signal	800 mV
Oscilloscope term.	1 MΩ

4.1.4 Detector Systems

The sensor has two detection channels as mentioned previously with respect to the optical schematic of Figure 4-5 and as shown with electronic details in Figure 4-11. These are the transmit detector which is used to monitor the transmit pulse intensity and shape, and the receive
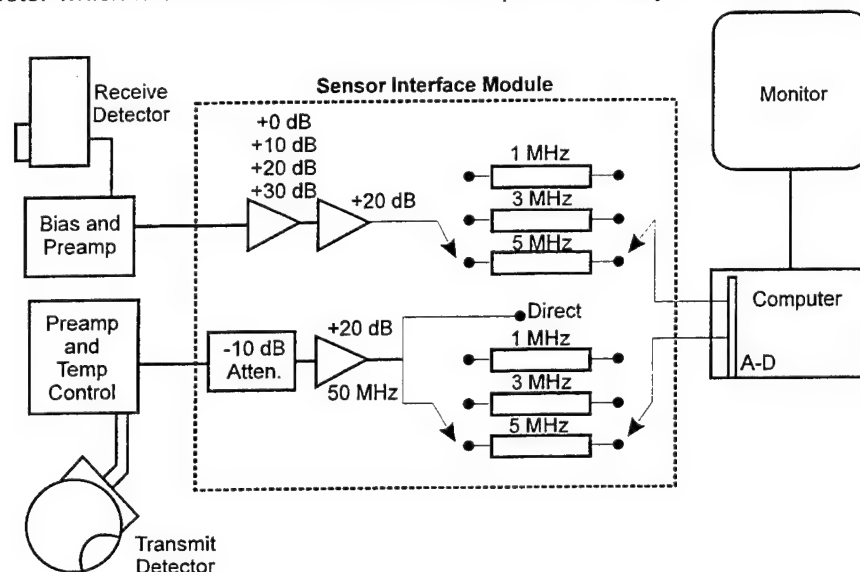
Figure 4-11. Detector and amplifier block diagram.

detector which is used to monitor the return radiation collected by the telescope. The detectors and preamplifiers are located on the sensor optical table and their output signals are carried to the Sensor Interface Module located in the equipment rack. The Sensor Interface Module provides for additional signal amplification (with nominal values shown in the figure), a choice of low pass filters as described below, and provides an analog output to the analog-digital (A-D) transform circuit located on a circuit card within the system computer. The computer, monitor, and other data acquisition equipment also located in the equipment rack are used for storage, display and processing of the digitized data as described in Section 4.1.6.

Transmit detector

Sampling of the laser transmit beam was complicated by the presence of multiple transverse modes that can lead to large intensity variations across the beam diameter from shot-to-shot. This fact precluded the use of the conventional approach wherein the beam is focused on a small detector element. In the conventional case of focusing a multimode beam, the problems of movement of focal hot spots across the detector, variation of responsivity across the detector element diameter, and beam steering give rise to unacceptable fluctuations in the data that are estimated to be on the order of 20%. Therefore, the alternative approach using an integrating sphere and small diameter detector element was utilized. In this approach the integrating sphere causes a factor of about 10^6 reduction in the signal due to the effect of integrating the beam over the internal surface of the sphere. However, this signal reduction is desirable because of the very high sensitivity of the recommended high speed, photoconductive (PC) HgCdTe detector which, in fact, necessitated the use of an additional attenuator at the entrance of the integrating sphere.

The transmit detector system composed of a PC HgCdTe detector attached to an integrating sphere is shown in Figure 4-12. A portion of the transmit beam is split off and directed through an attenuator into the sphere entrance hole. The detector is mounted at 90 deg with respect to the input beam direction and a baffle between the detector and the wall on which the input beam first impinges prevents the detector from receiving first-bounce, direct radiation. The detector element is contained in a small cannister with an infrared transmissive window that allows for a wide field of view in order to sample radiation from a large angle within the sphere. The specifications for these various elements are detailed in Table 4-6.
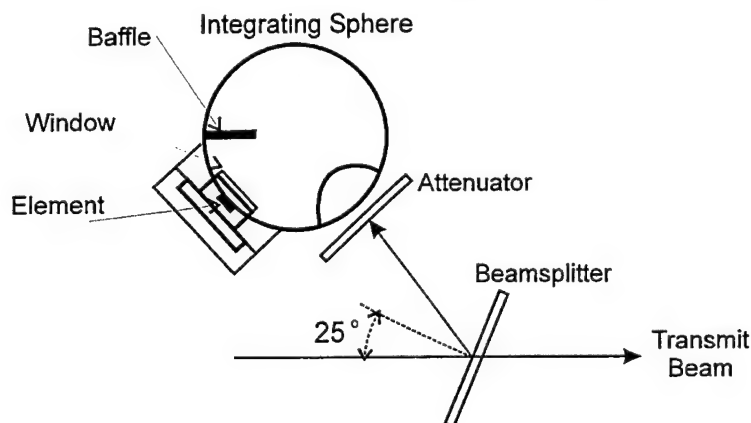

Figure 4-12. Transmit detector.

The beamsplitter indicated in Table 4-6 took several forms over the course of sensor field testing. In the first approach, an uncoated ZnSe element was used with an angle of incidence approximately 10 deg less than Brewster's angle. This element gave a reflectivity which was constant as a function of wavelength for the usual case of a beam polarized parallel to the optical table (P-polarization). It was this configuration that was used to satisfy the test requirements for measuring absolute reflectivity of a calibrated canvas target at a range of 600 m. In the second approach, outlined in the table, it was required to achieve approximately identical reflectivities for S- and P-polarization at a single wavelength for the purpose of measuring absolute target reflectance as a function of transmit polarization state. Constant reflectivity for each polarization

was achieved, but the reflectivity became wavelength dependent. The system was calibrated for this wavelength dependence. Finally, the relatively high value of 5% reflectivity was chosen for the beamsplitter in the polarization measurements because much lower values of reflectivity would have resulted in much larger differential values between the S and P states.

Table 4-6. Transmit detection system parameters.

Component	Characteristics
Integrating sphere	
Dimensions	2 in. diam, 0.75 in. aperture
Coating	Gold
Attenuator	Ge, ND2
Beamsplitter	ZnSe, 5% refl S&P, 25 deg
Detector	
Type	PC HgCdTE
Manufacturer	EG&G Judson
Element dimensions	0.25 x 0.25 mm
Window	ZnSe, uncoated
Element FOV	131 deg
Element temperature	-60 $^{\circ}$C
Cooler type	3 stage, thermo-electric
Peak D*	1.94×10^8 cm Hz$^{1/2}$/W
Responsivity	12.0 V/W at 9.7 μm and -60°C
Time constant	7 nsec
Bias voltage/current	0.405 V/14.58 mA
Saturation voltage	4 V into electronic filters

For the purpose of performing an absolute reflectivity calculation with a target as discussed in Section 4.2.3, the factors for detector responsivity and detector window transmission as a function of wavelength are eliminated by calibration with an energy meter. Nonetheless, these dependencies are shown in Figure 4-13 for reference. It can be seen that the wavelength dependence is not strong over the 9.2-10.7 μm range of interest. There is similarly negligible wavelength dependence of the attenuator at the entrance of the integrating sphere.
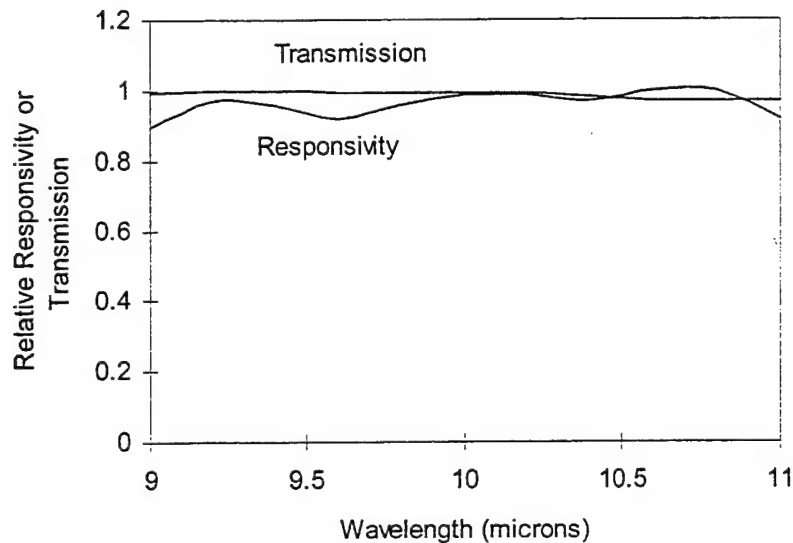
82

Figure 4-13. Transmit detector dependence on wavelength.

The transmit detector preamplifier and amplifier train are shown in Figure 4-14. The voltage preamplifier has a gain of +30.2 dB, an ac-coupled bandwidth of 700 Hz-135 MHz, and a noise figure of 3 nV/Hz$^{1/2}$. At the full bandwidth of the preamplifier, its noise is 35 μV and at the filtered bandwidth of 5 MHz it is 7 μV. This value is about 10^3 lower than the intrinsic detector noise level. The preamplifier schematic is shown in Fig. 4-15. The following amplifier with a gain of +20 dB and bandwidth of 61 MHz was initially built for the system, but was found to saturate the data acquisition card; therefore, a -10 dB attenuator was placed in series to give a net post amplification gain of +10 dB. After transmission through the filters, the net transmit detector gain at the input to the A-D card in the computer was found to be exactly +40.2 dB with an ac-coupled bandwidth of 850 Hz-5 MHz. A buffered "direct" line gave access to the unfiltered transmit pulse profile with a bandwidth of 61 MHz. The user-selectable filters allowed for selection of low pass filters with an upper frequency -3 dB cutoff at 1 ,3, and 5 MHz. These filters were 7-pole, Bessel designs with flat group delay. Note that the maximum permissible signal level at the filter inputs to avoid saturation is 4 V. In order to provide an operating margin, signal levels should be kept below about 3 V.
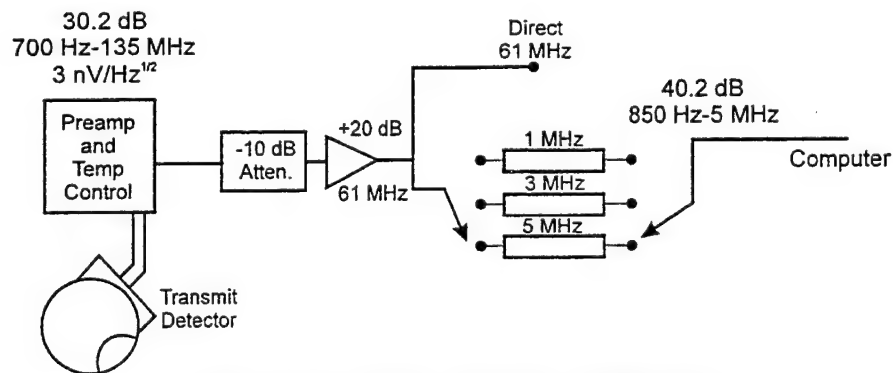

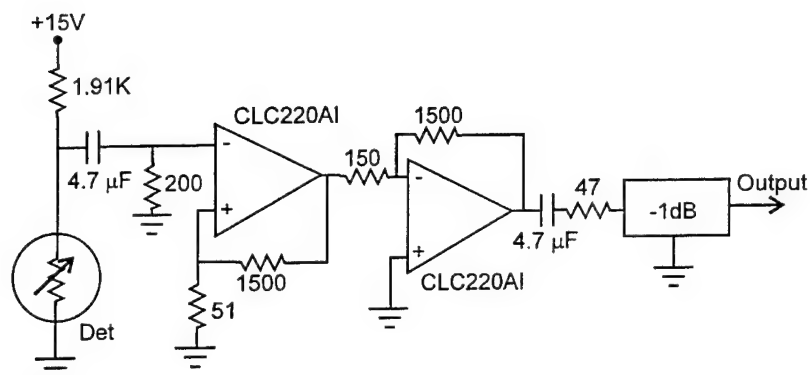Figure 4-14. Transmit detector amplification.

Figure 4-15. Transmit detector preamplifier schematic.

Receive detector

The receiver detection system is shown in Figure 4-6. It includes the photovoltaic (PV) HgCdTe detector in a pour-fill dewar that was integrated with the sensor and tested in the field. In addition, a HgCdTe detector using a split-Stirling cooler was designed and built, but was not tested with the sensor because of its reduced detectivity. The detectors were mounted on a 3-axis translation stage with micrometer adjustment. Specifications for both detector types are given in Table 4-7.

Table 4-7. Receive detector specifications.

Parameter	Pour-Fill Cooler	Split-Stirling Engine Cooler
Type	PV HgCdTe	PV HgCdTe
Manufacturer	SAT	Graseby Infrared
Element dimensions	1.0 x 1.0 mm	1.0 x 1.0 mm
Window	Ge, AR coated	Ge, AR coated
FOV	55 deg	70 deg
Temperature	77 °K	77 °K
Cooling	Liquid nitrogen, pour-fill, 8 h dewar	0.4 W Split-Stirling cooler
Peak D*	5.6×10^{10} cm Hz$^{1/2}$/W	2.5×10^{10} cm Hz$^{1/2}$/W
Peak responsivity	4.8 A/W at 58% Q.E.	not measured
Transimpedance conversion	17,172 V/A	not measured
Bandwidth, -3 dB	7 MHz	5 MHz
Saturation voltage	4 V	not measured

The responsivity of the pour-fill detector and the transmission of its AR coated window are shown as a function of wavelength in Figure 4-16. These factors are important for absolute calibration of the sensor using a known reflector, because it is not possible to calibrate the receive path with a broadband energy meter as was the case with the transmit detector in the transmit beam path.
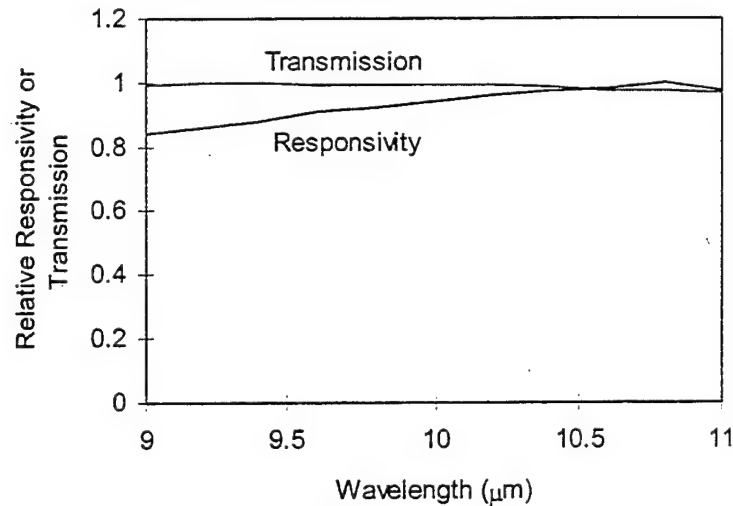
84

Figure 4-16. Receive detector wavelength dependence.

The receive detector preamplifier and amplifier train are shown in Figure 4-17. The preamplifier located with the detector on the sensor optical table is a transimpedance type with a conversion factor of 17,172 V/A. Its schematic is shown in Figure 4-18. Given the peak detector responsivity of 4.8 A/W, the preamplifier output voltage factor is 82,426 V/W. Furthermore, the preamplifier noise figure is 1.5 pA/Hz$^{1/2}$ which gives a voltage noise of 58 μV at a bandwidth of 5 MHz and is about a factor of 100 less than the intrinsic detector noise. The voltage amplifier immediately following the preamplifier has available three independently switchable, zero or +10 dB gain settings. This allows for the user-selectable net gains shown in the figure. The second amplifier in the train has a fixed gain of +20 dB. A set of filters identical to those in the transmit pulse detection system are available for selection of upper cutoff frequencies at 1 ,3, and 5 MHz. After transmission through the filters, the net transmit detector voltage gain at the input to the A-D card in the computer is selectable with values of exactly 50.21 dB, 60.14 dB, 70.1 dB, and 80 dB with an ac-coupled, lower bandwidth of 411 Hz and an upper bandwidth selectable at 1, 3, and 5 MHz. Note that the maximum permissible voltage at the output of the filters to avoid saturation is 4 V with the interstage gain set at 0 dB. In order to achieve a safe operating margin, signals should be limited to 3 V.
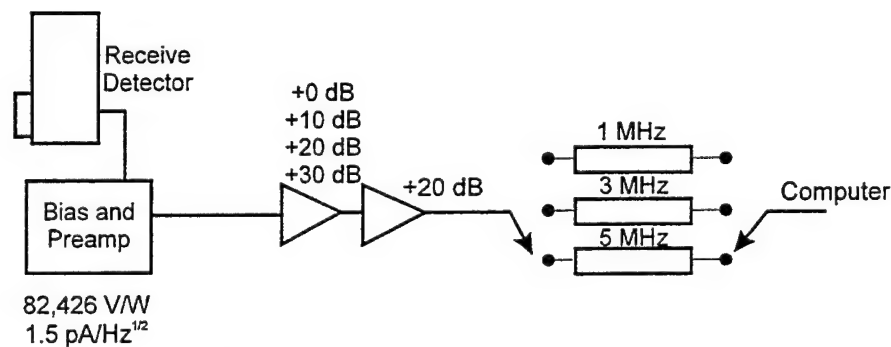

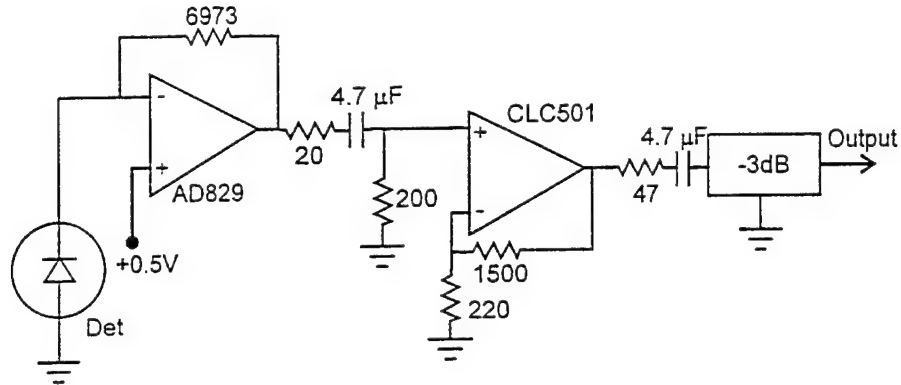Figure 4-17. Receive detector amplifiers.

85

Figure 4-18. Receive detector preamplifier schematic.

4.1.5 Interface Electronics Module

As shown in the block diagram of Figure 4-19, the Interface Electronics Module contains the transmit and receive signal amplifiers and filter sections as described with reference to Figure 4-11. It accepts the delayed A-trigger and first line sync signals from the Laser Power/Signal Module, passes them through (shown by dotted lines) to the A-D card located in the system computer, and adds an appropriate delay to the first line sync signal for the diagnostic oscilloscope. A discussion of the timing of the various signals generated by the Laser Power/Signal Module is contained in Section 3.1.4. The analog transmit and receive signals from the optical table are routed both to the A-D card for data acquisition and to the oscilloscope for display. Finally, the Interface Electronics Module houses the power distribution network for the various systems located on the optical bench, controls for the television camera, and readouts for the shot counter and catalyst temperature. All components shown in Figure 4-19 are contained in the equipment rack, with the exception of the external clock. The trigger requirements and setup of the A-D card and oscilloscope are discussed in Section 4.1.6
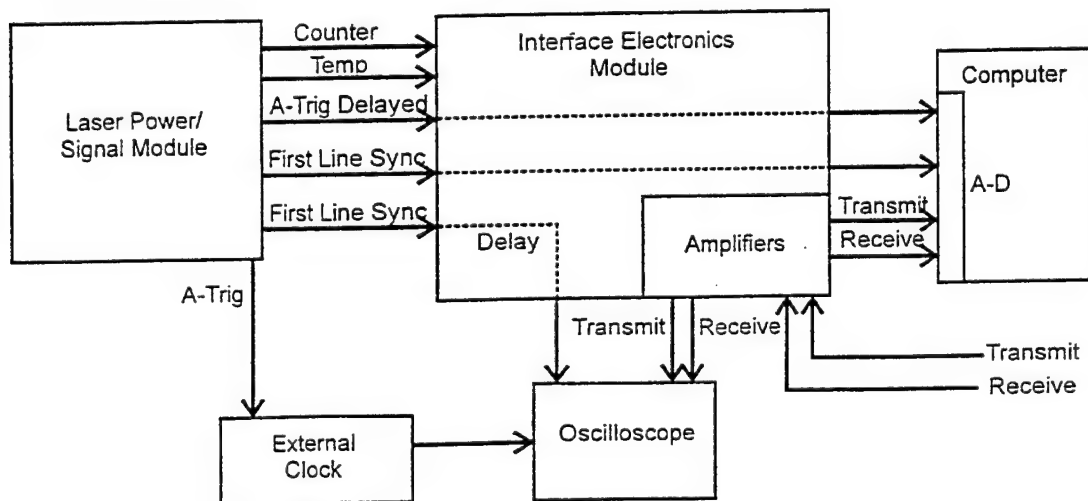

Figure 4-19. Interface Electronics Module functional block diagram.

The layout of the Interface Electronics Module and cabling to other subsystems contained in the equipment rack is shown in Figure 4-20. Trigger connections to the Laser Power/Signal Module, the digital oscilloscope, and its external clock generator are shown in detail. The Electronics Module includes a top panel that contains front-mounted inputs for pass-through to the
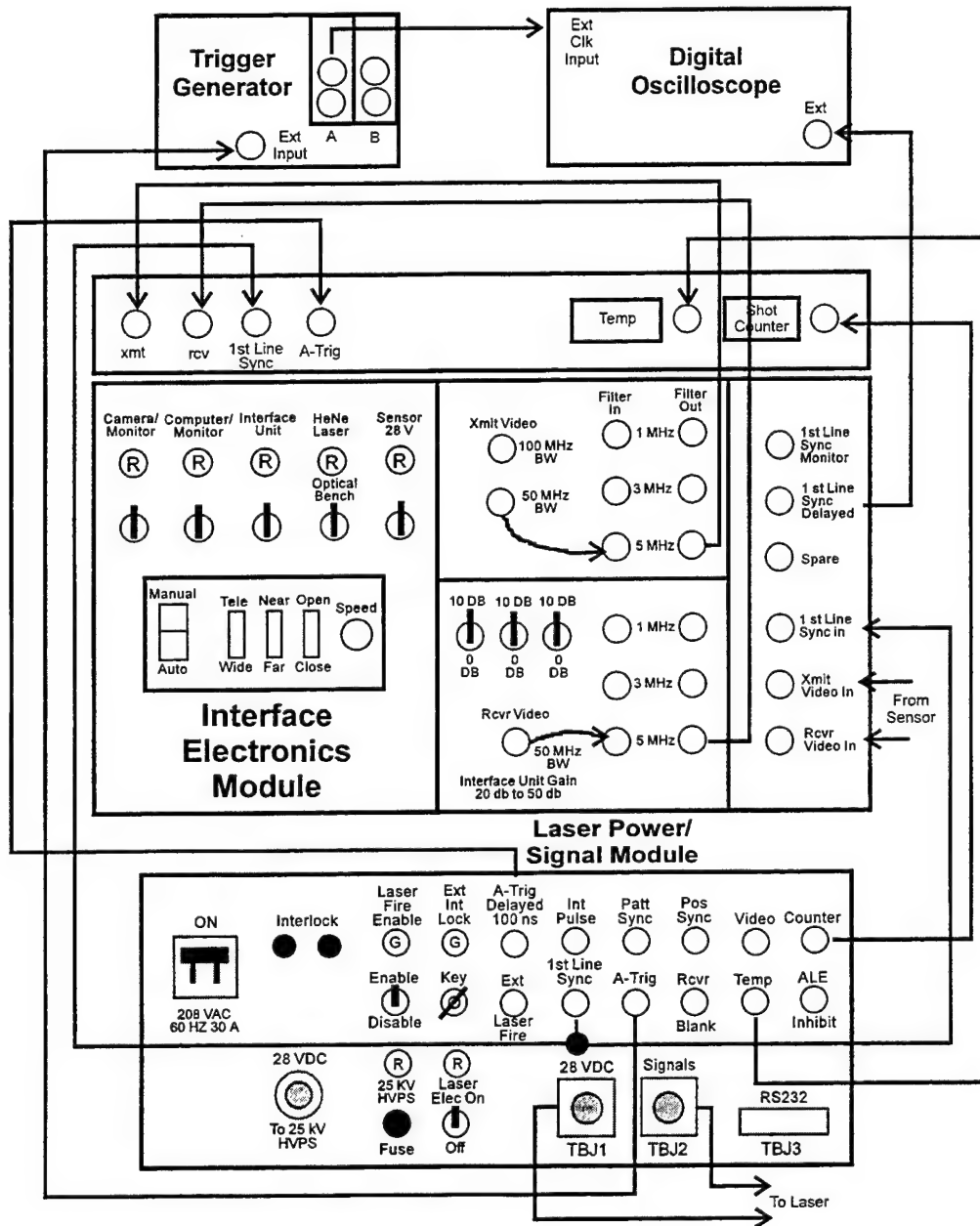

Figure 4-20. Interface Electronics Module layout.

A-D card, the temperature readout and the shot counter. The main panel consists of four sections. The largest section on the left side of the unit contains power switches with indicator lights for the sensor and the television controls which includes lens zoom and focus. The top-central section of

the Interface Electronics Module is devoted to the transmit pulse monitor and contains a high bandwidth output for displaying the transmit pulse and a 50 MHz output that connects to the low pass filters of choice. The lower-central section of the Interface Electronics Module contains the user-selectable receiver series amplifiers and low pass filters. The final section contains inputs for the transmit and receive signals from the sensor optical table, trigger input from the Laser Power/Signal Module, and trigger output to the digital oscilloscope.

4.1.6 Data Acquisition System

The data acquisition and display system was developed in two phases. In the first phase which included the first two field trials, the function of data acquisition was performed by a digital oscilloscope with its external clock trigger generator. In this case, the oscilloscope was capable of displaying individual transmit and receive pulse burst trains, but could store only a running average of these waveforms, thereby precluding critical sensor noise level analysis on a burst-to-burst basis. As defined in Section 3.2.2, a burst is a 200 Hz repetition rate train of pulses containing various wavelengths. Furthermore, the oscilloscope required a general purpose interface bus (GPIB) which was capable of a data transfer rate of only about 300 kB/sec. Therefore, a second phase of data acquisition refinement was entered into in which a two channel Analog-Digital (A-D) card was developed for the system computer that would permit acquisition of all transmit and receive signals for all individual pulse bursts. In addition, the sensitivity of acquisition was increased from 10 bits with the oscilloscope to 12 bits with the digitizer card. In the case of the digitizer card, pulse display software allowed for monitoring of individual transmit and return pulse amplitude and shape in order to determine the level of optical neutral density filtering required and as an indicator of laser wavelength tuning quality. However, this diagnostic was not entirely suitable and the oscilloscope was used for this function.

The data acquisition and display system is composed of two major sections, including (1) the system computer with its internal A-D card, monitor, and uninterruptible power supply (UPS) and (2) the digital oscilloscope with its external clock trigger generator. The data acquisition and display system components are shown within the dotted line of Figure 4-21 and in their relative positions with respect to other components in the equipment rack. As detailed in Section 4.2.5, the analog transmit and receive signals from the sensor optical table first enter the Interface Electronics Module where they are amplified and filtered before transmission to the digitizer in the computer. The digitizer also requires trigger signals from the Laser Power/Signal Module. Other inputs to the computer include the television signal from the sensor optical table and control signals to and from the gimbal servo amplifier.
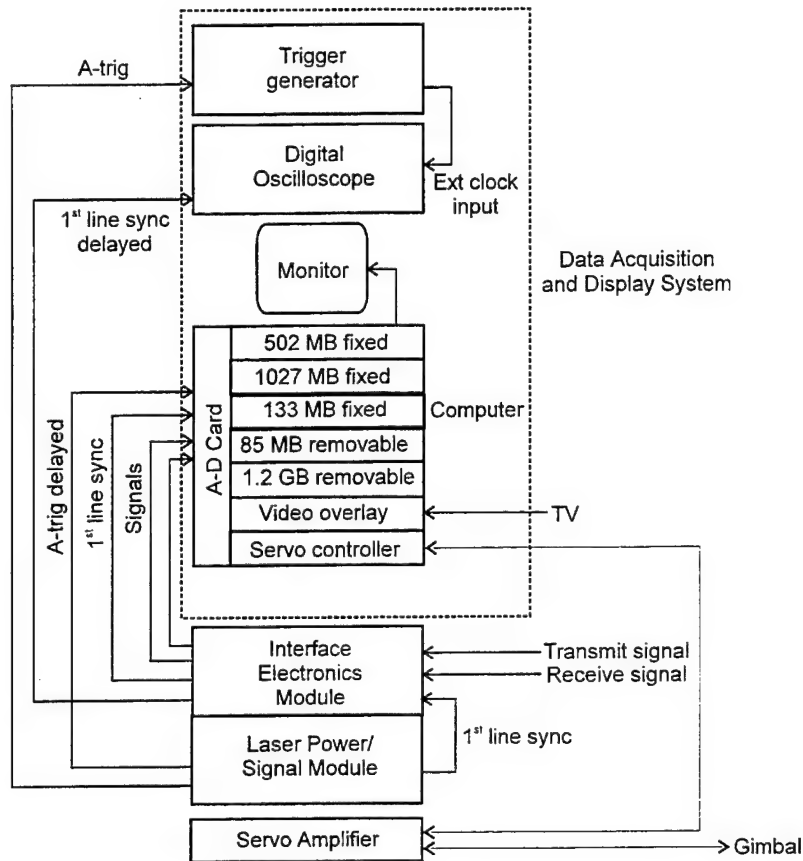
Figure 4-21. Data acquisition and display system block diagram.

Digital oscilloscope

The digital oscilloscope with its external clock trigger generator was used to display both transmit and receive waveforms and could be used alternatively to digitize data for storage in the system computer. Specifications for this equipment are detailed in Table 4-8. The sequence mode was used for data acquisition in which data was acquired in a gated window for each transmit and receive pulse, thereby eliminating data acquisition in the 5 msec blank period between laser firings.

Table 4-8. Digital oscilloscope specifications.

Oscilloscope make/model	LeCroy 9430
Clock make/model	LeCroy 9210/9211
Sampling rate	30 MHz
Resolution	10 bit
Bandwidth	150 MHz
Acquisition mode	Sequence
Memory length/channel	50 K
Interface	GPIB

Cabling to the oscilloscope and external clock is shown in Figure 4-20 and required an A-trig signal into the clock and a first line sync delayed trigger signal into the oscilloscope. A timing diagram for the various trigger signals with respect to laser output is shown in Figure 4-22 and is related to the electronics timing diagram presented previously in Figures 3-7 and 3-8. Note that A-trigger is emitted at the firing of each laser line, first line sync is emitted at the time of A-trigger for only the first line in a pattern (or burst), first line sync delayed is emitted with a delay of 700 nsec from the starting edge of first line sync, and the gain-switched laser output occurs about 800 nsec after A-trigger.
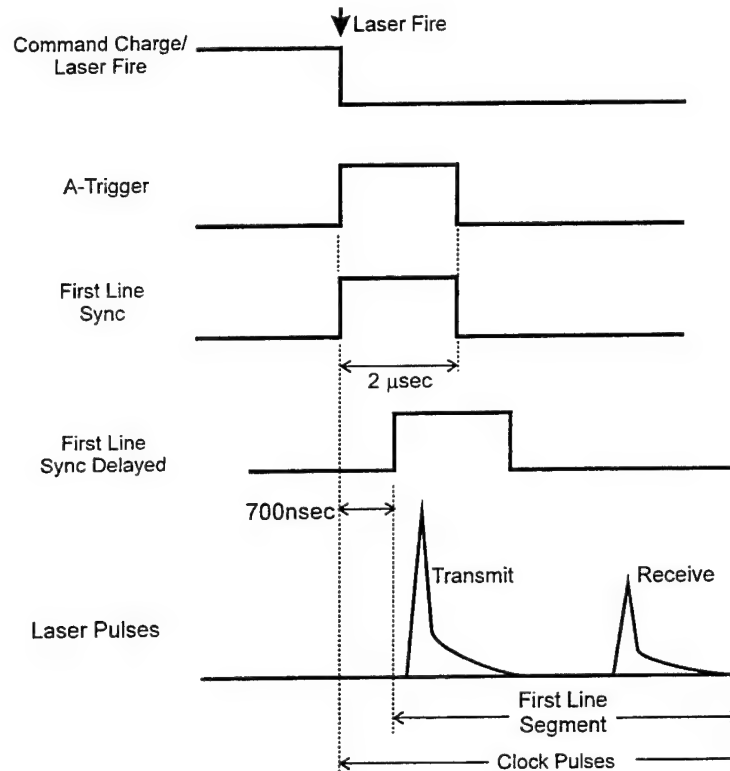
Figure 4-22. Oscilloscope and external clock timing diagram.

The timing sequence is as follows. The A-trigger signal starts the external clock which runs for a predetermined segment time that encompasses both the transmit and receive pulses. The oscilloscope samples and digitizes data at the clock rate for both the transmit and receive channels only during the segment time when clock pulses are received and ignores the much longer 5 msec interpulse period. The oscilloscope is programmed to accept a predetermined number of total clock pulses after which a completed record is declared and it resets to accept data for the next burst. Each of the "time bins" defined by the sampling rate of the external clock is updated with a running average from burst-to-burst and it is not possible to store data for individual bursts. After the average transmit and receive signals for a predetermined number of bursts is collected, the data is downloaded to the system computer. Finally, it should be noted that the oscilloscope triggering is such that it requires approximately 30-50 clock pulses before the start of data acquisition for each pattern of wavelengths (a single burst) in order to arm its data acquisition mode. This is accomplished with the first line sync delayed signal.

90

The optimum data acquisition setup is determined by a tradeoff between (1) the desired sampling rate (clock rate), (2) the range to the target which determines the total number of samples required to obtain both the transmit and receive pulses, (3) the number of lines (segments) in a burst, and (4) the maximum 50 K record length of the oscilloscope per burst (since essentially a single average burst is stored). The time from A-trig to emission of the transmit pulse (800 nsec) and some time to ensure complete capture of the receive pulse (1 μsec) should be included in the calculation of total segment time. The data acquisition setup criterion can therefore be formulated as NST$\leq$50K, where N is the number of wavelengths in a burst, S is the sampling rate (clock rate), and T is the total segment time. T = 1.8μsec+2R/c, where R is the range and c is the velocity of light. An example is shown in Table 4-9 where the 16.8 K total sample number suggests that the product NST can be increased by about a factor of three before reaching the 50 K oscilloscope limit.

Table 4-9. Sample oscilloscope data acquisition setup.

Range	5 km
Roundtrip time	33 μsec
Total segment time, T	34.8 μsec
Number of lines in burst, N	16
Sampling rate, S	30 MHz
Sampling resolution	33 nsec
Total samples, NST	16.8 K
Maximum samples	50 K

Computer and A-D card

All sensor functions were controlled from the system computer including gimbal motion, laser fire control, data acquisition, and video imaging. Therefore, the computer contained a variety of control cards including the analog-digital signal processor, video overlay card, the gimbal control card, and peripheral interface cards. The computer, keyboard, and monitor were mounted directly in the equipment rack.

Specifications for the computer are shown in Table 4-10. Importantly, the system included a number of high capacity fixed and removable storage media. In the process of data taking, data would be downloaded to the 1027 MB fixed SCSI (small computer system interface) drive and then transferred to the 1.2 GB magneto-optical removable media for storage and post-processing. The interface hookups at the rear of the computer are shown in Figure 4-23.

Table 4-10. Computer specifications.

Processor	486DX2, 66 MHz
Ram	8 MB
Bus type	VESA local
Drives:	
A: 3.5" floppy	1.44 MB
B: 5.25" floppy	1.2 MB
C: IDE fixed	502 MB
D: SCSI fixed	1027 MB
E: SCSI fixed	133 MB
F: SCSI removable Bernoulli	85 MB
G: RAM disk	1 MB
H: Magneto-optical	1.2 GB
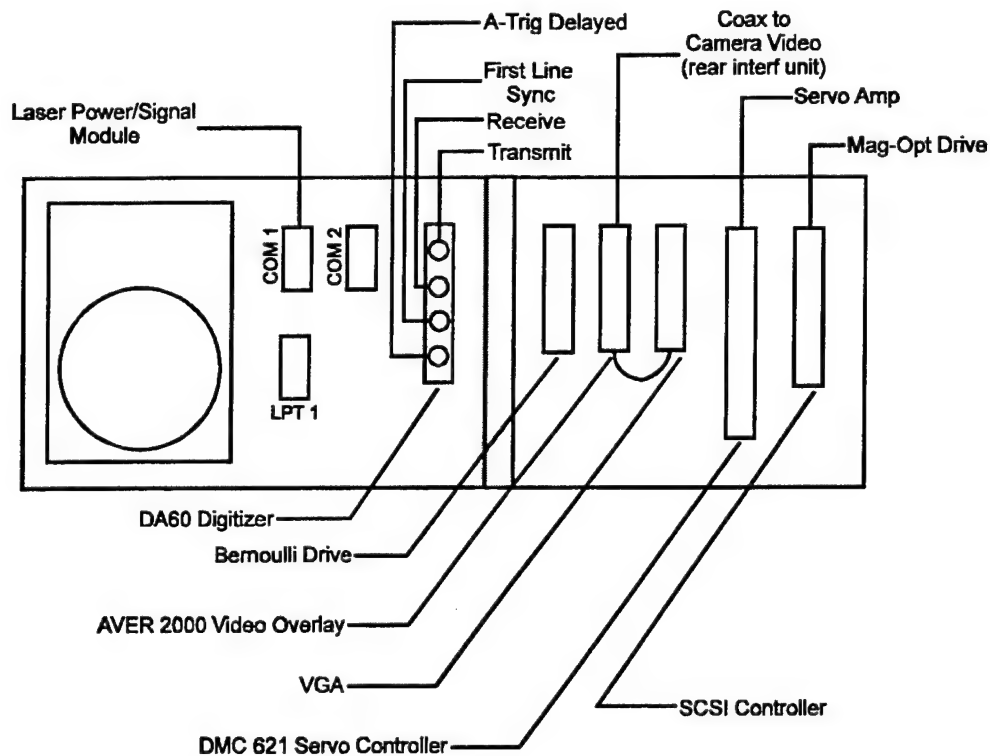
Figure 4-23. Computer rear attachments.

The A-D card was developed by Signatec, Inc.(model DA60) for the FAL system and its use allowed for storage of transmit and receive signals for each wavelength pattern as opposed

to the case of the running burst average obtained with the oscilloscope. In the case of the card, data for each wavelength pattern (burst) is downloaded to the computer hard drive between bursts. The card specifications are shown in Table 4-11. The card has two analog input channels for the transmit and receive pulses and requires two trigger inputs. It is possible through software to adjust the gain of the A-D card and its offset. Finally, the card is used in the ac-coupled mode exclusively.

Table 4-11. Digitizer specifications.

Input signals	
	Channel 1 analog transmit pulse
	Channel 2 analog receive pulse
	External trigger
	External clock
Analog inputs	
Full scale voltage	5.0 V peak-peak
Impedance	50 Ω
Bandwidth (-3 dB)	dc to 30 MHz
Coupling	dc or ac (jumper selectable)
Gain settings	
Range	50 to 1 (34 dB)
Resolution	0.2 dB
Control	Digital, 8 bit DAC
Resolution	12 bits
Trigger modes	Single shot and segmented
Memory size	256K by 12 bits, each channel
Sampling rates	30 MHz and 30 MHz/factors of 2
(2 channel)	or
	20 MHz and 20 MHz/factors of 2

Triggering and data acquisition is accomplished in the segmented mode as shown schematically in Figure 4-24. A four wavelength pattern (burst of wavelengths) is shown where T refers to a transmit pulse and R refers to a receive pulse. As in the case of the digital oscilloscope, the A-D card acquisition memory is adjusted by the user so that each segment contains a pair of transmit and receive pulses for each wavelength. For acquisition of each pattern of wavelengths, the first line sync trigger arms the card and the A-trigger delayed signal starts the data acquisition for each segment. It is necessary to delay the first A-trigger signal by about 100 nsec with respect to the first line sync pulse to allow the card time to arm. This causes no loss of data in the transmit pulse, because of the roughly 800 nsec delay between the first line

93

sync pulse and emission of the laser gain-switched spike. The card onboard clock is typically set at a sampling rate of 30 MHz and runs over the segment time. The active memory length is determined by the product of segment size and the number of wavelengths in the pattern.
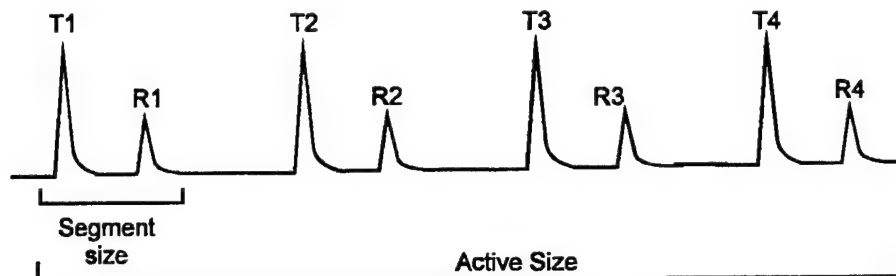

Figure 4-24. Digitizer record definition.

In a manner similar to the digital oscilloscope, the optimum data acquisition setup is determined by a tradeoff between the range to the target and the number of lines in the pattern, but with the constraints of a fixed sampling rate of 30 MHz, a maximum segment size of 4096 samples, and a fixed memory size of 256 K per channel. The upper limit to segment size of 4096 samples determines the maximum range because the segment size must be large enough to capture both the transmit and receive pulses. Note that for extended targets, such as clouds, the pulse return can be significantly stretched and additional receive pulse time must be included. Assuming the receive pulse is 1 μsec long and the sampling rate is 30 MHz (33 nsec sample period), the maximum range time, T, is (4096-30)x33nsec=134 μsec; and the maximum range, R, is cT/2=20.1 km. For an extended target, assuming a 10μsec stretched return pulse, the maximum range would be about 19 km which far exceeds the sensor capability to detect range-resolved targets. At the maximum range (4096 samples), the total number of wavelengths in a pattern can be 256K/4096 or 62. Of course, the wavelength scanner only allows for a maximum of 20 wavelengths in a pattern; therefore, the 256 K upper memory limit will never be approached.

The calculation of absolute signal voltage is important for sensor calibration. Signal voltage can be obtained by first noting the bit gain setting contained in the header file for the data of interest. The gain setting bit is related to full scale voltage (FSV) through a lookup table (Cal Table .001). Finally, volts/bit=FSV/4096, for the 12 bit card resolution, and signal volts=(signal bits-ground bits)xvolts/bit.

Data acquisition software

The code was written in Microsoft, Inc. Professional BASIC Compiler version 7.1. It also used several third party assembly routine libraries for increased processing throughput where needed and for greater functionality in areas where the compiler was deficient. The code was written in a modular form for easy modifications and increased maintainability. The following list contains the FAL module names and respective code line counts.

Module Name	Code Lines
MAIN.BAS	125
ACQUIRE.BAS	83
AVERUTIL.BAS	741
UTILITY.BAS	471
GIMBAL.BAS	555
OSCOPE.BAS	1057
DMC.BAS	489
DISPLAY.BAS	585
FALUTILS.BAS	1263
TOTAL	5369

The computer code was developed to interface the three main sensor hardware systems. These were (1) the laser and its firing setup via the wavelength shifter interface software, (2) the gimbal with the television video overlay, and (3) the data acquisition system with the A-D card. The procedure for setting up the sensor follows these interfaces. First, the wavelength pattern and repetition rate are specified through the wavelength agile tuner software. Second, the gimbal position is chosen via a computer interface screen which also contains a live television video overlay. Third, a simulated oscilloscope screen is accessed in order to set up the gains and offsets of the A-D data acquisition card and to test for the proper optical attenuation in the transmit and receive beam paths by viewing the transmit and return pulses in real time. Alternatively, the digital oscilloscope can be used for this latter function. Fourth, the data acquisition screen is accessed from which data for the header file is inserted and data acquisition is started. Finally, various utilities are available to review the data and experimental parameters. A description of the various screens and menus that are available in the operation of the sensor are described below.

The introductory main menu screen shown below displays various options (where the second line is displayed when the Laser option is highlighted). The user must access four screens to set up the sensor for data acquisition. This process begins with the Laser screen (1). After the laser is set up, it is then necessary to access the Gimbal screen (2) for setting up the gimbal position; the Oscope screen (3) for set up of the A-D card; and finally the Acquire screen (4) for preparation of the data header file, file name designation, and to start data acquisition. The introductory screen reappears after setting up each secondary screen. Other menu items provide for access to utilities for file and data manipulation.

The Laser screen shown in Figure 4-25 provides for selection of all laser operating parameters. Laser setup proceeds in the manner detailed in Section 3.1.6 and after quitting the shifter program, the user is returned to the main sensor options screen. The parameters contained in the Laser screen are automatically stored to a file with the name of the acquisition file and the extension .TXF.

```
 1        2         4                        3
Laser  Gimbal  Acquire  Display  Utils  Oscope  File  External  Quit
Setup/Select  Laser  Firing  Patterns  (AGILITY UNIT)
```

```
┌─────────────────────────────────────────────────────────────┐
│                   WAVELENGTH AGILE TUNER                      │
│  ┌──────────────────────────┐  ╔═══ STATUS ═══╗ ┌─PATTERN 0─┐│
│  │                          │  ║              ║ │ 0    9R30 ││
│  │ R - RUN                  │  ║BURSTS PER SEC - 5.7║ 1  9R18││
│  │ S - SHUT DOWN            │  ║AVE REP RATE - 34.3 ║ 2  9P44││
│  │                          │  ║MAX REP RATE - 200  ║ 3 10R20││
│  │ P - SELECT PATTERN       │  ║      LASER - READY ║ 4 10P24││
│  │ L - PEAK PATTERN         │  ║ SYSTEM RUN - OFF   ║ 5 10P30││
│  │ B - ENTER BURSTS PER SEC │  ║    UNIT ID - 32    ║ 6      ││
│  │ M - ENTER MAXIMUM REP RATE  ║ ERROR CODE - 0     ║        ││
│  │                          │  ╚════════════════════╝        ││
│  │ I - RESET                │                                ││
│  │ C - CALIBRATE LINES      │                                ││
│  │ F - FILE MANAGEMENT      │      PG DN - PAT MENU           ││
│  │                          │        ESC - EXIT              ││
│  │                          │                                ││
│  │                          │                                ││
│  │   SELECT COMMAND         │                                ││
│  └──────────────────────────┘                        └────────┘
└─────────────────────────────────────────────────────────────┘
```

Figure 4-25. Wavelength selector main screen.

The gimbal screen shown in Fig. 4-26 has two major fields,. the azimuth and elevation positions indicated along the bottom and the large central area for the video overlay. The positions can be stored by moving the gimbal (with the cursor keys) to the desired position and pushing one of the F1-F8 keys. The target indicator in the middle of the video field is produced electronically and is boresighted with the laser beam. Various help screens can be accessed by pressing Shift +
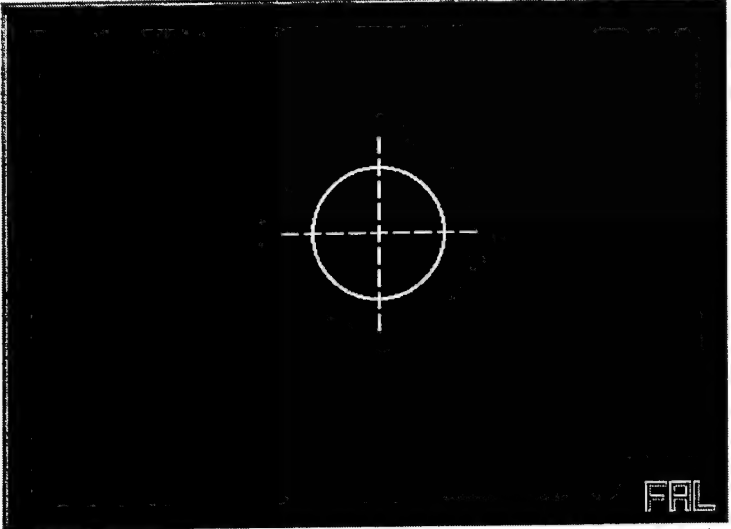
Figure 4-26. Gimbal screen.

F1. The image can be stored to a file with the name of the particular data acquisition and the extension .TIF.

The Oscope screen shown in Figure 4-27 is used to set the gains and offsets of the transmit and receive signals by viewing them on the virtual oscilloscope screen which is the large window that occupies most of the display. It is also necessary to set the A-D card memory segment size and active size which is the product of segment size and number of segments or wavelengths. The laser can be turned on and off directly from this screen to facilitate setting these parameters. In operation, the transmit pulses occupy the top half of the screen and the receive pulses occupy the lower half. Saturation of either of these channels occurs when the pulse amplitude exceeds the respective screen half. The Status window to the right of the screen indicates when any bit in the pulse record is saturated. The cursor keys provide for scrolling horizontally through the wavelengths in a pattern and the Page Up and Page Down keys provide for scrolling vertically among patterns.
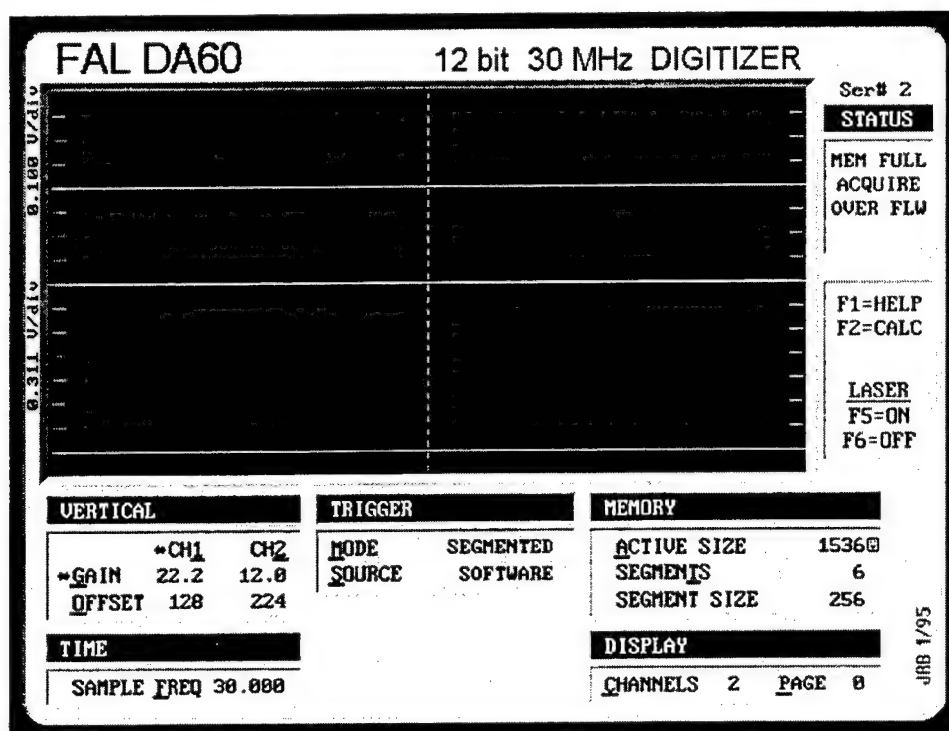
Figure 4-27. Oscope screen.

The Acquire screen shown in Figure 4-28 contains five fields, including the field for storage of test parameters and the test file name as specified by the user, a field to catalog the laser firing parameters, a field for the F-key functions, an area that displays the video image, and a window to view the transmit and receive waveforms during data acquisition. The acquired data are stored to a file with the name specified by the user and the extension .FAL. After the test parameters are entered, the acquisition can be started by pressing F3. The experiment will run for the indicated time after which the laser automatically turns off. The data will then reside on the SCSI hard drive D and can be viewed using the utilities.
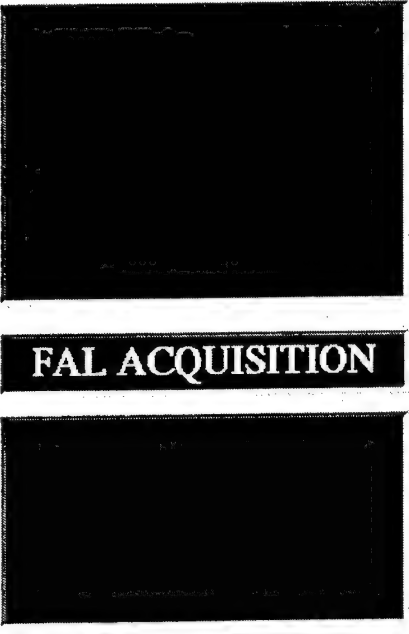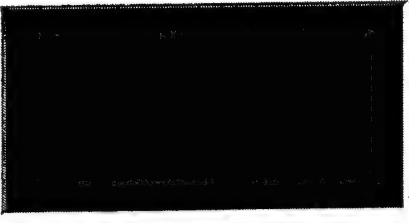
```
LENGTH OF TEST:                          003.0
(IN MINUTES)
FILE NAME TO USE:                        Test_001
(DO NOT USE AN EXTENSION)
(.FAL WILL BE ADDED FOR YOU)
RANGE TO THE TARGET:                     1200
(IN METERS)
GAIN ADDED TO THE RECEIVE SIGNAL:        0
(IN dB)
TRANSMIT FILTER USED:                    OK

RECEIVE FILTER USED:                     OK

CHEMICAL TYPE:                           OK

TEST COMMENT:                            Morning Te
```

```
LINES IN THIS PATTERN:                   7
FIRING LINES IN THIS PATTERN:            6
AVERAGE LASER FIRING RATE:               34.3
BURST RATE:                              5.7
```

```
F3=START ACQUISITION     F5=LASER ON
F4=STOP ACQUISITION      F6=LASER OFF
F7=DISPLAY WAVEFORMS
F8=BLANK WAVEFORMS
```

FAL ACQUISITION

Figure 4-28. Acquire screen.

The data and experimental parameters can be accessed from the main menu through the display shown in Figure 4-29. The first of these options, Display Waveform File, is shown in Figure 4-30 with an example of transmit and receive waveforms. The data displayed is contained in the relevant file with the .FAL extension. The scrolling features are identical to those for the Acquisition screen. The header file shown in Figure 4-31 contains all of the pertinent experimental conditions. A sample of the Display TXF *.File option is shown in Figure 4-32. It contains all of the parameters stored for the wavelength shifter. The Display Image Option displays the stored video scene image. Finally, various file utilities are accessed through the Utils menu shown in Figure 4-33.

```
1)  Display Waveform File

2)  Display Waveform Header File

3)  Display *.TXF File

4)  Display Image File

5)  Return to Main Menu
```
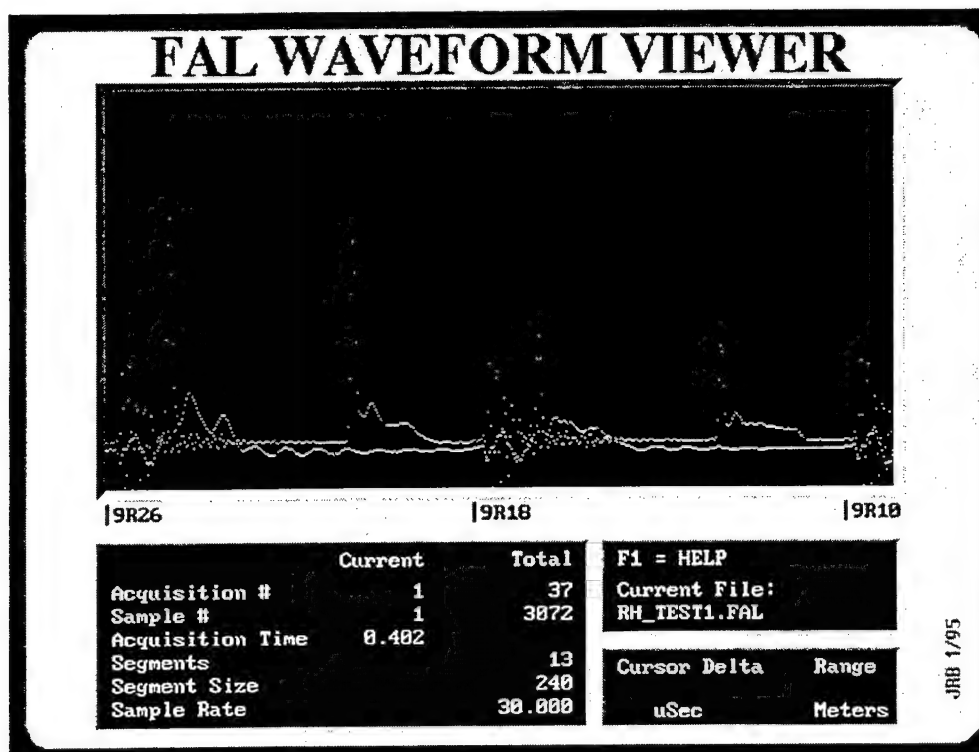
Figure 4-29. Display menu screen.

Figure 4-30. Display waveform file screen.

```
File Name: RH_TEST1.FAL    Start Date: 5-18-1995   Start Time: 16:52:21
Comments: Roofhouse test against clouds. Signal filtered @ 5 MHz.


Total Bursts Acquired:          37      Clock Frequency (MHz):   30.000
Active Memory Size (Samples):   3072    Test Duration (Seconds):  12.0
Segment Size (Samples):         240
Segments (Lines per Burst):     13


       Gain (Bits:    db)    Offset (Bits)     Ground (Bits)

Ch 1          60    12.0           224              414
Ch 2          40     8.0           224              482
Receiver             0

Range to Target (Meters):   690                   Filters
                                            Transmit    Receive
Gimbal Position (Degrees)                   NO FILTERS  ND 2.001
      Az:             -0.86
      El:              0.04

Chemical Type: H2O

Header Version:  2
```

Figure 4-31. Display waveform header file screen.

```
                TXF Data for File: RH_TEST1.TXF

TXF Filename                        : RH_TEST1.TXF  Line #      Name   Fire/No Fire
Creator of TXF file                 : 3 Sigma           0       9R26        1
Current command for Agility Unit    : 0                 1       9R18        1
Laser Firing                        : No                2       9R10        1
Laser Ready                         : Yes               3       9P10        1
Error Code                          : 0                 4       9P16        1
Agility Pattern Number              : 5                 5       9P42        1
Pattern Rate                        : 2.9               6      10R30        1
Firing Rate                         : 38.2              7      10R22        1
Number of lines in this pattern     : 17                8      10R14        1
                                                        9      10P08        1
                                                       10      10P16        1
                                                       11      10P24        1
                                                       12      10P32        1
                                                       13       HN16        0
                                                       14       HN16        0
                                                       15       HN16        0
                                                       16       HN16        0
```

Figure 4-32. Display TXF file screen.

```
1) Convert Range to Time

2) Convert Time to Range

3) Calculate Beam Width at Range

4) System Information

5) Shell to DOS

6) Adjust Video

7) Format Optical Disk

8) Return to Main Menu
```

Figure 4-33. Utility screen.

Typical waveforms

Typical waveforms obtained with the data acquisition system are shown in Figures 4-34 to 4-36. In Figure 4-34, the A-D card was used at the 30 MHz sampling rate and the tailchopper was on. Data was obtained for a pattern of 11 lines emitted at a 200 Hz repetition rate and 1 Hz burst rate. The 9R20 line with an emitted energy of about 150 mJ is shown. The target in this case was a plywood board located at a range of 600 m. The initial noise in the receive channel is due to laser discharge-induced EMI and subsides by the time of the return pulse. The receive pulse waveform is displaced from the transmit waveform to show this effect clearly.

100
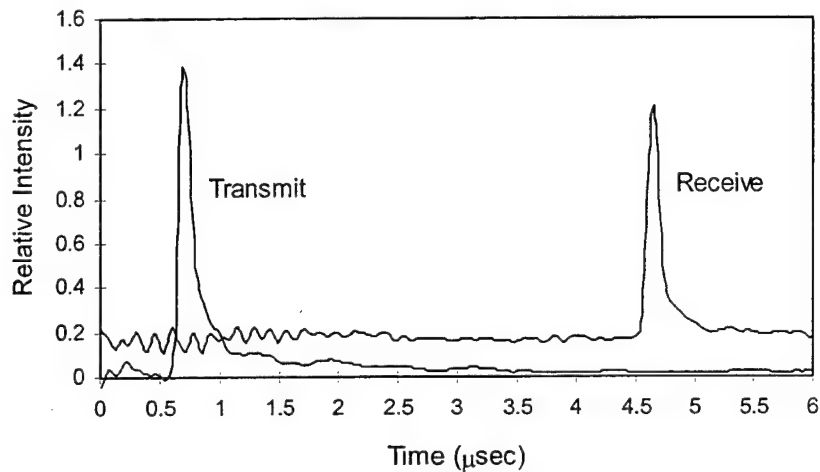
Figure 4-34. Waveform, solid target with tailchopper.

The data shown in Figure 4-35 were obtained under the same conditions as for the previous figure, except that the near-range return has been amplified. The experiment was performed just after a light rain and under these conditions the aerosol backscatter can be observed to a range of about 300 m. The peak in the return observed at an equivalent range of about 100 m is due to the cross-over effect where the transmit beam is beginning to enlarge appreciably beyond the telescope secondary mirror diameter.
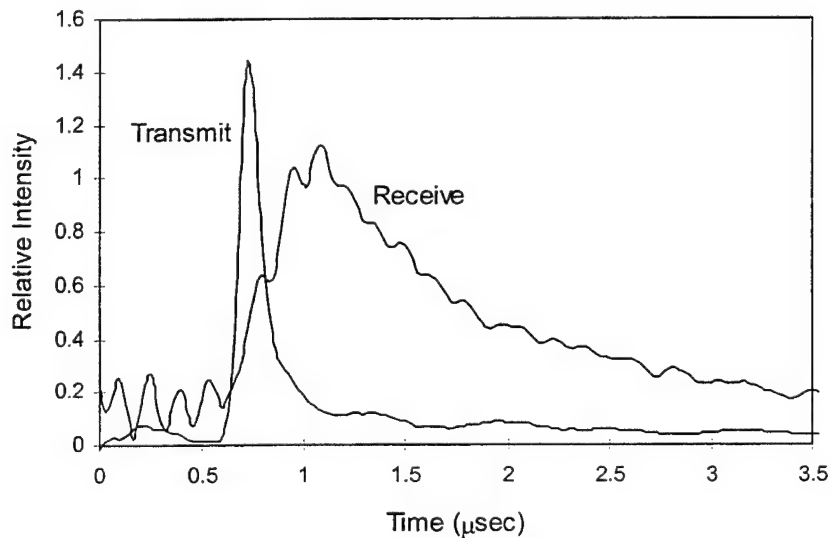
Figure 4-35. Waveform, aerosols with tailchopper.

Data was also obtained with the digital oscilloscope operating at a sampling rate of 100 MHz. and with the tailchopper on as shown in Figure 4-36 for the 9P20 line. In this case, the sensor was elevated to range off rain clouds in a light rain. The near-range aerosol return (used in conventional range-resolved measurements) is of much lower amplitude than the return off the cloud at a range of 1.5 km. Specular reflection off water droplets may contribute to the increased cloud signal. Furthermore, the pulse in the cloud is significantly lengthened compared to the transmitted waveform suggesting significant penetration into the cloud. Consideration of strong water droplet reflection with good penetration suggests that differential absorption measurements could be performed on similar clouds containing chemicals, emitted for example in chemical process stacks.
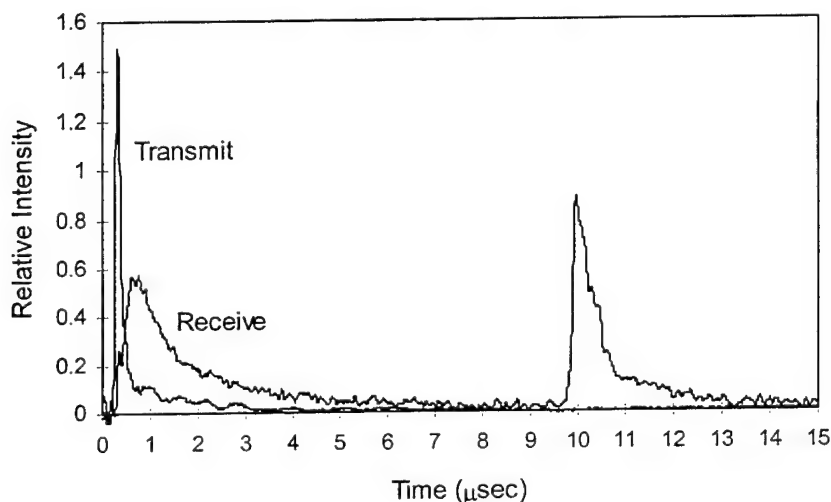
Figure 4-36. Waveform, aerosols and cloud with tailchopper.

4.1.7 Post-Processing Software

Post-processing software was developed primarily to provide the sensor operator with a method of evaluating data in the field in order to rapidly obtain an indication of the quality of the data, the state of the sensor, and the validity of the experimental setup. The code allows for calculation and display of (1) concentration-path length product, CL; (2) range-resolved concentration, C(R); (3) transmit and receive pulse amplitude standard deviation; and (4) calculation of atmospheric water vapor content.

The code was written in the C and C++ languages using the Microsoft Inc. C/C++ compiler, version 8.00c and the NMAKE utility of Visual C++ 1.5. Graphics were generated with the LabWindows Run Time Library version 2.3a from LabWindows for DOS (National Instruments Corp.). A modular format was used for code development including the FAL_MAIN.CPP module which contains the "main" function, initialization, and event loop results display; the FAL_IO.CPP module containing the code to read and process the data and auxiliary files; and the FAL_CALC.CPP module which contains the code for calculations. The Main routine reads data

files produced by the FAL system and performs various types of data analysis. The results are displayed as either number charts or plots, either of which can be printed. The files required for operation of the Main routine are FALMAIN.UIR, the LabWindows resources file; the *.FAL main sensor data file; the *.TXF laser operating parameters file; the *.TXT chemical coefficient data files; the CHEMTYPE.INI chemical coefficient file names; and the CALTABLE.011 calibration values. All files except the *.FAL and *.TXF files must exist in the same directory as the executable file. The initial search directory for *.FAL files is \FDATA which must exist but need not hold the data files. The fundamental program logic flow is shown in Figure 4-37 and the detailed flow with the four optional analysis tools is shown in Figure 4-38.
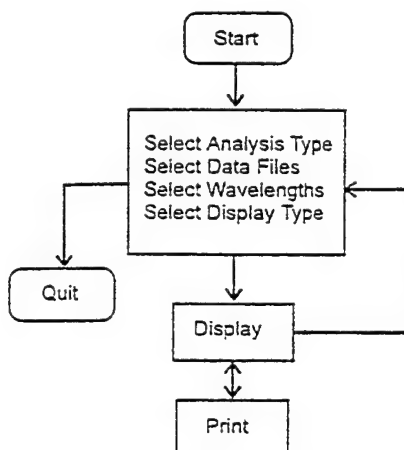
Figure 4-37. Fundamental post-processing logic flow.
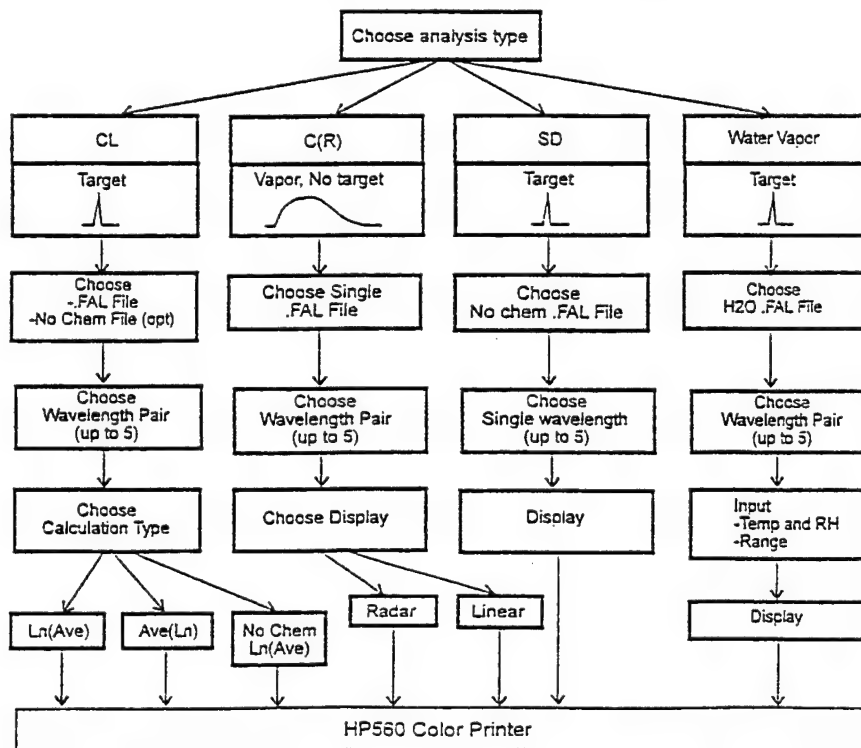
Figure 4-38. Detailed post-processing logic flow.

103

The post-processing screen shown in Figure 4-39 has four fields that follow the program logic flow. These fields are Select Analysis Type, Select Data File(s), Select Wavelengths or Wavelength Pairs, and Select Display Type or enter Water Vapor Data. Selections may be made in any order with the exception that a data file must be selected before wavelengths are selected. At least one data file must be selected for all analysis types. An additional file (Without Chemical) may be selected for the CL measurement and up to four files may be selected for the Range-Resolved Simulated Radar calculation. At least one wavelength (STDEV) or wavelength pair (all others) must be selected. Up to five wavelengths (STDEV) or five pairs (all others) may be selected. Selections may be made with a mouse or with the keyboard using TAB, SHIFT TAB, ENTER, and SPACEBAR combinations. After all selections have been made, the Calculate menu item is selected. The data is read and processed and the results are displayed on the screen. The user may then select the Print menu item to print the screen or the Return menu item to return to the main screen. While at the main screen, the user may select the Quit menu item to exit the program. Note that the first 0.5 μsec for each transmit pulse and the first 1.0 μsec for each receive pulse are not processed in all segments to eliminate noise generated during the laser discharge.

Figure 4-39. Post-processing selection screen.

Concentration-path length product, CL

The post-processing code provides for three methods of calculating CL., all based on Beers' Law for absorption and assuming a simple pair-wise ratioing of signal intensities for two wavelengths only. In the first two methods, the return pulse intensities are normalized with respect to their transmit intensities, but no factors are included for target reflectivity as a function of wavelength. These two methods involve basically taking the logarithm of the average of the

intensity ratios or taking the average of the logarithm of the intensity ratios. In the third method, the normalized receive intensities are further normalized with respect to the previously obtained target background reflectivity (and perhaps absorption cell window spectral dependence) in the absence of chemical (the no chemical case) at the specific wavelengths used in the pair-wise calculation.

Calculation of the CL product begins by forming the individual normalized receive pulse with respect to its corresponding transmit amplitude for each laser firing (I_a^i for wavelength a and burst i, as an example). This is accomplished by taking the ratio of the receive peak intensity to the transmit peak intensity where the peak intensity is defined as the largest data point in the record, excluding noise generated by the laser discharge at the beginning of each record. By method 1 (logarithm of the averages) the calculation of CL is obtained by the equation

$$CL = \frac{1}{2\Delta K} \ln\left[\frac{\frac{1}{N}\sum_{i=1}^{N} I_a^i}{\frac{1}{N}\sum_{i=1}^{N} I_b^i}\right] \tag{4-4}$$

where a and b refer to the two wavelengths under comparison, typically at the peak and minimum of the chemical absorption profile; the index, i, is the burst number; N is the total number of bursts; and ΔK is the differential absorption coefficient at the wavelengths a and b. These designations are clarified in Figure 4-40 which shows intensity as a function of time for a four-line wavelength pattern and depicts either the transmit or receive channel.
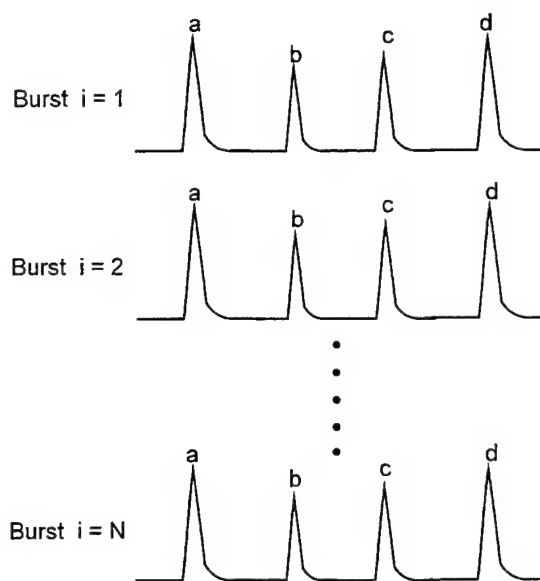

Figure 4-40. Data index illustration.

By method 2 (average of the logarithms), the calculation of CL is given by

$$CL = \frac{1}{2\Delta K} \sum_{i=1}^{N} \frac{1}{N} \ln\left(\frac{I_a^i}{I_b^i}\right) \qquad (4-5)$$

where the logarithm of the ratio of normalized receive intensities for the wavelengths under comparison is obtained in each burst, i, and the logarithms are averaged. Finally, CL by method 3 is calculated from

$$CL = \frac{1}{2\Delta K} \ln\left[\frac{\left(\frac{1}{N}\sum_{i=1}^{N} I_a^i\right)_{chem} \left(\frac{1}{M}\sum_{j=1}^{M} I_b^j\right)_{nochem}}{\left(\frac{1}{N}\sum_{i=1}^{N} I_b^i\right)_{chem} \left(\frac{1}{M}\sum_{j=1}^{M} I_a^j\right)_{nochem}}\right] \qquad (4-6)$$

where it can be seen that the averages of equation 4-4 are normalized by the average over M bursts for the respective wavelengths in the absence of chemical.

Range-resolved concentration, C(R)

In order to calculate range-resolved concentrations, the formalism developed by Schotland was used, involving the stepwise difference of the logarithm of intensity ratios.[13] In this case all receive waveforms, stretched in time because of reflection from an extended target, are normalized with respect to the peak of the narrow transmit pulse. The stretched and normalized waveforms for each transmitted wavelength are then averaged over all bursts and the stepwise difference equation is as follows:

$$C(R) = \frac{1}{2\Delta K \Delta R} \ln\left[\frac{\bar{I}_a(R)/\bar{I}_a(R+\Delta R)}{\bar{I}_b(R)/\bar{I}_b(R+\Delta R)}\right] \qquad (4-7)$$

where the simplification for the case of wavelength-independent backscatter has bee invoked; the intensities are obtained from the averaged waveforms for wavelengths a and b; and ΔR is the range resolution of the transmit pulse, given by cT/2 (T=pulsewidth). Assuming a 200 nsec wide gain-switched spike with the tailclipper operating, the range resolution is 30 m.

As shown in Figure 4-41, the post-processing code also provides for the display of C(R) data as a function of range and azimuth on a simulated radar map with color-coded intensity levels. Up to four azimuth positions can be designated and the C(R) data obtained from four separate data acquisitions (four data files) is plotted along each azimuth. The range-resolved simulated radar mapped display is a representation of the C(R) vs. R averaged data. It covers a fixed range of 300 to 1000 m (with 100 m range bins) and the concentration in mg/m^3 is auto-scaled based on this range for the first data file selected and is not recalculated for subsequent files. The value computed and displayed for each range bin (numbered 1-7 in the figure) is an average of the points for that range. The wavelength table is also created from the first file.
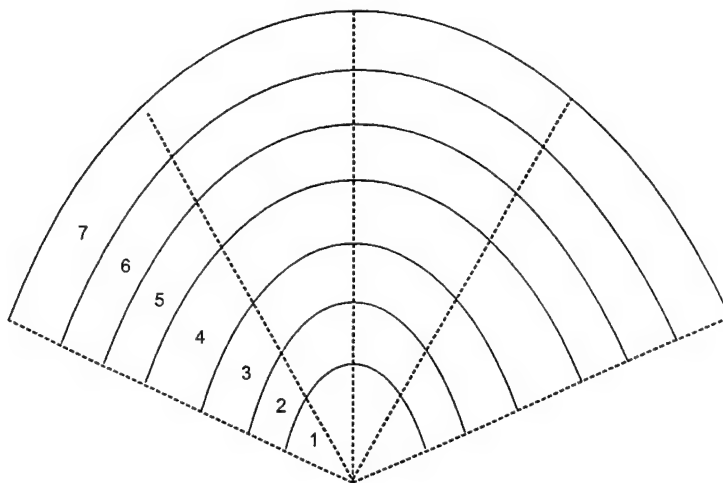
Figure 4-41. Simulated radar map.

Standard deviation, SD

The post-processing software provides for the calculation of the standard deviation for the transmit intensity, receive intensity, and the ratio of receive to transmit intensities for any wavelength in a burst as a function of the number of bursts, n, where n goes from 2 to the total number of bursts, N. With reference to Figure 4-40, the standard deviation is calculated "vertically" through the bursts for each wavelength a-d. The average, A_a, for wavelength a is calculated over the entire array of bursts and is defined as

$$A_a = \frac{1}{N} \sum_{i=1}^{N} I_a^i \tag{4-8}$$

where I_i^a is the transmit, receive, or ratio of transmit to receive signal for wavelength a in burst i. The standard deviation, SD_a^n, for wavelength a and number of pulses n is given by

$$SD_a^n = \sqrt{\frac{\sum_{i=1}^{n} \left(I_a^i - A_a \right)^2}{n-1}} \tag{4-9}$$

and the percentage standard deviation is given by the ratio SD_a^n / A_a.

Water vapor concentration

The water vapor concentration utility in the post-processing software provides for a rapid estimate of the atmospheric water vapor content as measured by the lidar and compares that

measurement to the value determined from meteorological data. In the latter case, the code uses a look-up table to determine the water vapor saturation value based on the user input of temperature, then calculates the water vapor content based on the user input of relative humidity. Five pairs of wavelengths can be used to produce up to five individual estimates and an average of water vapor density measured by the lidar. The code also determines the percentage deviation from the meteorological measurement. The formalism is identical to that shown in equation 4-4 with the range to the target as an added input. The absorption coefficients for the pairs of wavelengths are obtained from a look-up table.

4.1.8 Sensor Operating Procedure

The steps in initially setting up the sensor for a field test session are shown in the block diagram of Figure 4-42. Generally, these steps involve checking the multi-wavelength output of the laser on the spectrometer and the pulse profiles on the transmit detector; aligning with the target; cautionary steps to prevent damage of the receive detector; setting the optical attenuators, electronic filters, and electronic gain; and taking the first set of data. After these initial steps, subsequent data can be taken by entering only step 14. It has been found through field experience that the spectrometer check is not necessary and it is performed only occasionally throughout several weeks of testing as a formality. Furthermore, it has not been found necessary to adjust the sensor optical alignment after transportation to a field site or during extended test periods. Therefore, operation of the sensor has been shown to be straightforward and it can be operated by one person for rapid data taking in the field.

Step 1, turning on the laser, is detailed in Section 3.1.9. Generally, under conditions where the laser has been checked prior to sensor field testing, this involves simply turning on the main circuit breaker and the laser electronics (switch 1D) of the Laser Power/Signal Module shown in Figure 3-34.

Step 2 involves pouring liquid nitrogen into the pour-fill detector and ensuring that the sheet metal beam block is placed in front of the detector for the duration of target setup and the initial sensor check. It has been found that even backscatter from hard targets within one meter of the sensor will not cause noticeable loss of detector sensitivity, but the precaution of a beam block is taken in any case.

Step 3, turning on the sensor electronics, requires first setting the power switches for the television camera, interface unit, and sensor 28 V located on the Interface Electronics Module shown in Figure 4-20. Second, the computer, monitor, and external magneto-optical storage unit are turned on through the single power switch on the UPS. Finally, the digital oscilloscope and its clock trigger generator are turned on separately and the gimbal servo amplifier is turned on through a single toggle switch.

Step 4 is in preparation for checking the laser multi-line output on the spectrometer. This involves inserting copper mirror 8 of Figure 4-5 into the beam path to redirect the entire transmit beam. The mirror is kinematically mounted and needs no adjustment to achieve alignment with the spectrometer.

Step 5 involves entering the gimbal screen of the data acquisition software shown in Figure 4-26. Assuming that the servo amplifier in the equipment rack and the safety toggle switch on the gimbal head have been turned on, the gimbal will recenter itself and personnel must be

warned that this is about to occur. In the event that a message appears on the system monitor screen indicating that recalibration of the gimbal position is required, this should be performed at this point. Recentering requires invoking a software routine that involves (a) accessing the recentering code in the directory D:\FAL2\talk2bus, (b) pressing the F3 key to perform a download, (c) inputting the file name ZERO.FAC and noting the message "a carriage return will now be sent", and (d) inputting the code XQ #A. At this last command, the gimbal will go to the minimum elevation point and rotate 90 deg counter-clockwise, then recenter itself, after which it will respond to user commands to move to a new target or to various positions stored in memory accessible through the F-keys.
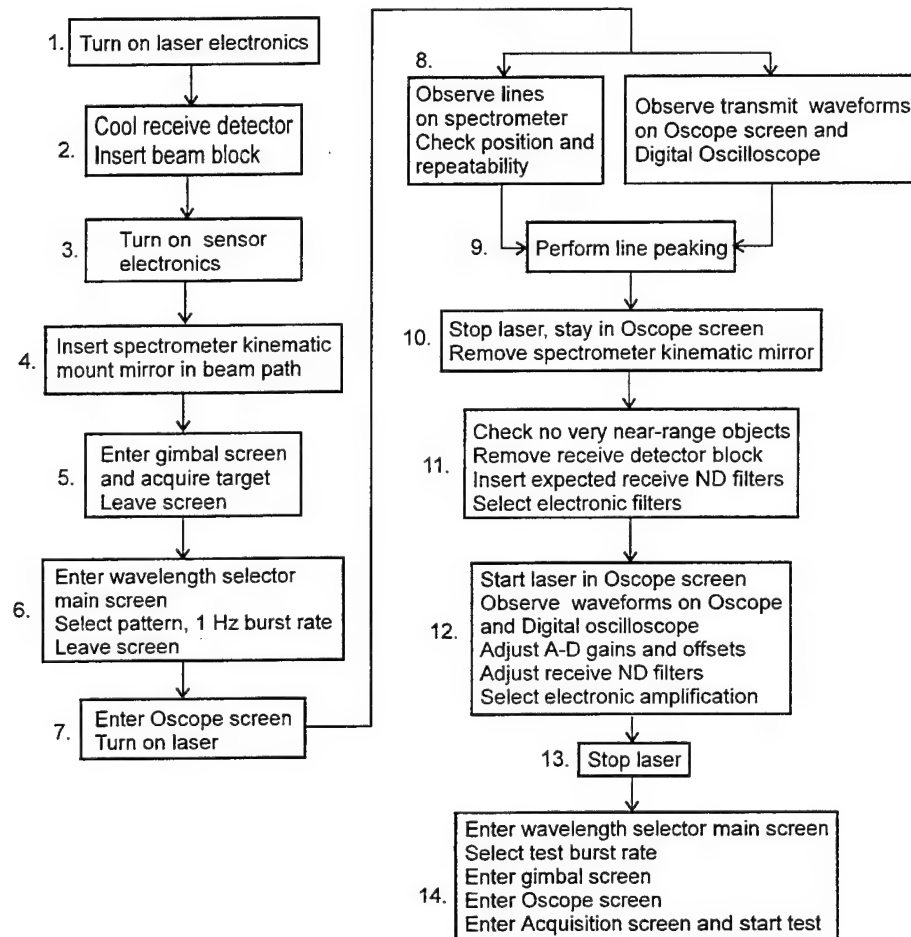

Figure 4-42. Sensor setup procedure block diagram.

Step 6 requires that the wavelength selector main screen shown in Figure 4-25 be entered in order to specify the wavelength pattern. It is desirable to set the burst rate to 1 Hz in order to conserve laser firings during the setup period.

Steps 7, 8, and 9 involve entering the Oscope screen shown in Figure 4-27 to turn on the laser and observe the transmit waveforms on the virtual oscilloscope. In addition, the digital oscilloscope is used for this purpose. The spectrometer is checked to verify the emitted

wavelength pattern and to note any erratic behavior from burst-to-burst. If necessary, peaking of the line positions is performed and adjustments to the input voltage per line and the position of the tailclipper are made.

Steps 10 and 11 include preparation for the final check of laser output prior to taking the first set of data. This involves removing the mirror that diverts the output beam to the spectrometer, inserting the expected optical ND filters (ND4 for a hard target at a range of 1 km, for example), and selecting the proper electronic filters with cabling on the front of the Interface Electronics Module shown in Figure 4-20.

Steps 12 and 13 include the final waveform check prior to taking data. Waveforms are observed on the virtual oscilloscope and the digital oscilloscope, the A-D gains and offsets are adjusted for maximum dynamic range, the receiver optical ND filters are adjusted, and selection of the electronic gains is made. The laser is then stopped prior to entering the data acquisition mode.

Step 14 follows the discussion above concerning the data acquisition software. The introductory main menu screen is entered and the operator moves consecutively through the Laser, Gimbal, Oscope, and Acquire screens. After the data is acquired, the user can access the various utilities to view the data, perform post-processing to verify sensor operation and the experiment setup, and move the data files to high capacity storage media. Generally, if the target remains unchanged, step 15 is all that is required to continue with additional data sets.

4.2 SENSOR TEST RESULTS

This section describes calibration of the sensor including (1) absolute reflectivity measurements of a calibrated canvas target as a function of wavelength and measurement of the short term sensor noise level and (2) operation of the sensor under field test conditions. The reflectivity calibration was undertake to verify sensor alignment, detector responsivity, and optical and electronic calibration factors. The results show that the sensor was aligned correctly and that the optical and electronic component data were accurate. The measurement of noise level is of central importance in determining the minimum detectable concentration-path length product. It was found that the sensor would achieve a 1-2% signal stability after averaging 16 shots, suggesting that it is capable of state-of-the-art performance. Finally, the description of field trials is included primarily to indicate the level of sensor reliability and as a basis for statements about possible improvements that appear in Section 6. Detailed analysis of the field test data was undertaken by CBDC personnel and will be available in agency publications and professional journals.

4.2.1 Calibration

The reflectivity measurements were conducted with a target made of Army canvas that was supplied by CBDC after calibration at that agency. It was uncoated and the "light" side was used. The canvas measured approximately 3 m on a side and was attached to a rigid support at the top and by ropes to supports along the sides; therefore, it was constrained along the top, but could move moderately in the wind. It was located at a range of 600 m. The laser was set up to cover the entire CO_2 spectrum from 9.2-10.7 μm, including the lines 9R30, 9R10, 9P10, 9P26, 9P36, 10R30, 10R10, 10P8, 10P20, and 10P32. The laser repetition rate was 200 Hz with a 4 Hz burst rate and the signals were averaged over 100 bursts. The peak receive signals were normalized by their corresponding transmit amplitudes as discussed in Section 4.1.6. The tests were repeated several times with essentially the same results.

The reduced data is shown plotted as points with the calibration curve in Figure 4-43. The steeply rising calibrated reflectivity as a function of wavelength is reproduced in the data. Furthermore, the data differs from the calibration curve by about 20% over the spectral range, but it is well within the experimental error. These results suggest that the various optical and electronic signal factors were accurately known. A detailed discussion of these factors and the method of data reduction is included below.
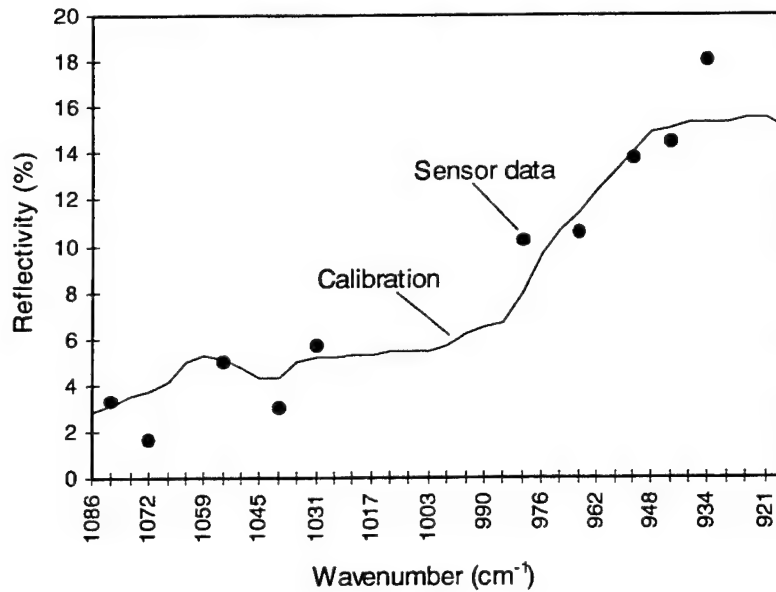
Figure 4-43. Canvas target reflectivity and sensor data.

The laser emits a gain-switched spike, followed by a 1 μsec tail, and chemical (or reflectivity) measurements involve determining the receive to transmit ratios of the spike only. Therefore, sensor calibration involves finding absolute relationships between the receive and transmit detector amplifier voltages and their respective laser spike intensities, taking into account the dependence of detector responsivity and optical component transmission on wavelength. The optical component factors can be seen with respect to Figure 4-44. The transmit beam passes through elements 1-4 before being partially reflected from element 5 into the detector assembly, 6. The receive beam passes through the antireflection coated afocal lens, the field lens, and the detector dewar window.
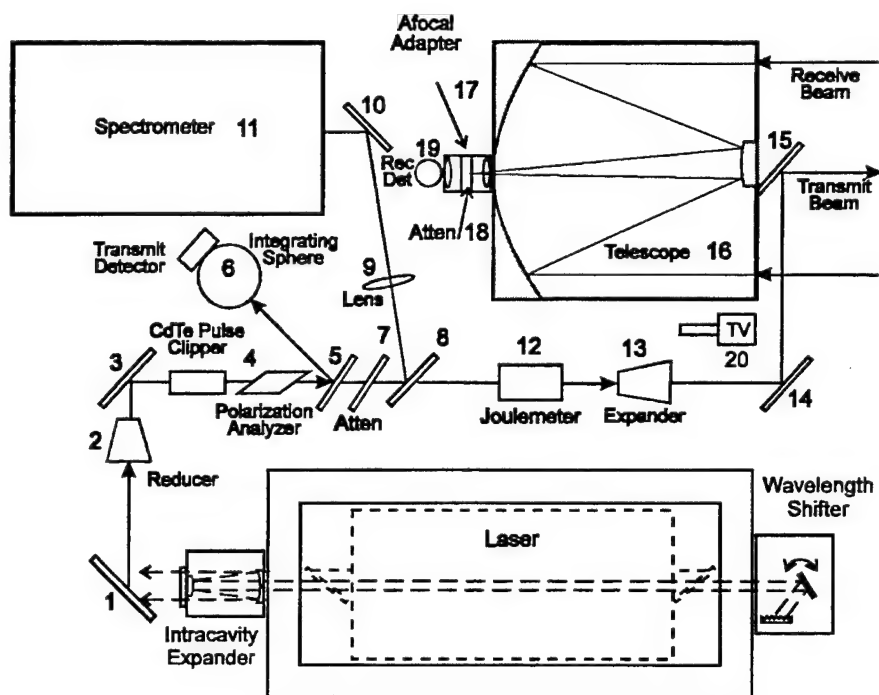
112

Figure 4-44. Sensor optical schematic.

In the case of calibration of the transmit path, a joulemeter (with flat response as a function of wavelength) is used to calibrate the peak intensity measured by the high bandwidth transmit waveform detector. This is accomplished by first measuring the output pulse shape with the transmit detector and relating the total energy integral obtained from its waveform to the total energy measured with the joulemeter. Second, the detector peak voltage is related to the output power for all of the laser lines through a measured calibration function that takes into account the spectral dependencies. In the case of the beam received by the telescope, however, it is not possible to accurately measure total energy with a joulemeter because of the extremely low levels. Therefore, the spectral transmission curves of the various optics and the detector responsivity are relied upon to relate receive detector voltage to received light intensity. This calibration of the receive path was verified to within a factor of two by direct tests using a blackbody radiator at the focus of a collimator and illuminating the receive telescope as shown in the bottom illustration of Figure 4-10.

Transmit detector calibration

Absolute calibration of the transmit detector begins by relating the total pulse energy to the peak power of the gain-switched spike. This is accomplished by analyzing a typical pulse profile and its integral obtained with the digital oscilloscope as shown in Figure 4-45. The spike integral, approximated as a triangle, is given by $1/2P_T\Delta T$, where P_T is the peak spike power and ΔT is the width of the base (typically 250 ns). Furthermore, it is shown by the integral that the

113

spike contains about 40% of the total pulse energy. Therefore, the equation relating peak power to total energy, E_{Tot}, is

$$P_T = 3.2 \times 10^6 E_{Tot}$$ (4-10)

where P_T is in Watts and E_{Tot} is in joules.
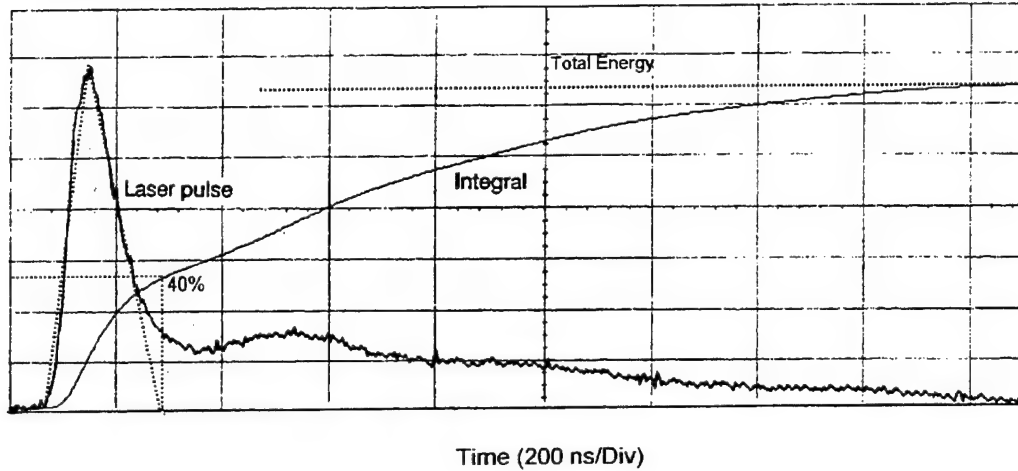

Time (200 ns/Div)

Figure 4-45. Typical output pulse waveform.

For all of the waveforms monitored by the transmit detector, a peak voltage, V_T, is associated with the spike and it is also proportional to total energy, by the same arguments that led to equation 4-10. However, the constant of proportionality differs from line-to-line because of the spectrally-dependent transmission of the optical elements shown in Figure 4-44 and the wavelength dependent detector responsivity. To account for these effects, the peak voltage and total pulse energy can be related through a wavelength-dependent factor, $K_1(\lambda)$, as follows:

$$V_T = K_1(\lambda) E_{Tot}$$ (4-11)

Combining this with the previous equation gives

$$P_T = \frac{3.2 \times 10^6}{K_1(\lambda)} V_T$$ (4-12)

Therefore, the problem of calibrating the transmit path amounts to specifying the correction factor $K_1(\lambda)$.

Measurement of the spectral correction factor involves measuring the output energy of each laser line with the joulemeter and noting the spike voltage. Alternatively, the total pulse integral can be used for this purpose once it is calibrated with respect to the joulemeter. The difference between the measured voltage and the voltage expected from pulse energy scaling is

114

attributed to the spectral effect. The resulting equation relating peak transmitted power to peak voltage is

$$P_T = 2.37 \times 10^6 R_T(\lambda) V_T F_T(\lambda) \qquad (4\text{-}13)$$

where $R_T(\lambda)$ is the wavelength calibration factor and is plotted in Figure 4-46. $F_T(\lambda)$ is the wavelength-dependent transmission of the power attenuator (7) in Figure 4-44 that is optionally placed in the transmit path. In performing the calibration tests, the joulemeter (12) of Figure 4-44 was placed after the beam expander (13) and the expander used in this case had a magnification of 1.6, allowing the joulemeter to capturing the entire beam. Furthermore, it was assumed that reflection off the total reflectors (14) and (15) caused negligible attenuation of the beam. Finally, these measurements were performed with a ZnSe Brewster plate in place of the beamsplitter (6). In the event that the alternative 5% beamsplitter is used to couple energy into the transmit detector, a different calibration curve is required.
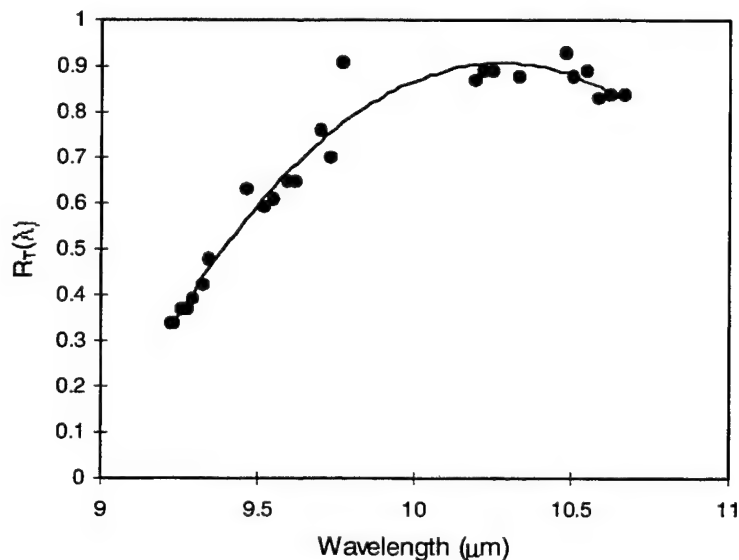

Figure 4-46. Transmit peak voltage correction factor.

Receive detector calibration

The measured receive detector voltage is given by

$$V_R = R_P R(\lambda) T_L(\lambda) T_W(\lambda) P_R \qquad (4\text{-}14)$$

115

where the parameters are defined as follows:

R_P Peak detector responsivity at the input to the filter section shown in Fig. 4-14. This value is 8.2426×10^5 V/W, including the fixed 20 dB (10x voltage gain).
$R(\lambda)$ Relative spectral responsivity of the detector shown in Fig. 4-16.
$T_L(\lambda)$ Wavelength-dependent transmission coefficient of the telescope field lens shown in Fig. 4-7.
$T_W(\lambda)$ Wavelength-dependent transmission of the detector window shown in Fig. 4-16.
P_R Peak power entering the telescope

It is assumed that the primary and secondary telescope mirrors are lossless and that their reflectivities are wavelength-independent.

Target reflectivity

In the case of sensor calibration, the canvas target was larger than the beam. Therefore, the power received by the telescope is given by

$$P_R = \rho(\lambda) P_T(\lambda) \frac{\Omega_R}{2\pi} \left[1 - \exp-\left(\alpha_T / \alpha_B\right)^2 \right] \exp(-2\alpha R) \qquad (4\text{-}15)$$

where the previously undefined parameters are as follows:

$\rho(\lambda)$ Canvas target reflection coefficient.
Ω_R Telescope solid angle at range, R, given by $\pi(R_1^2 - R_2^2)/R^2$; where R_1 and R_2 are the telescope primary and secondary radii, respectively.
α_T Telescope field of view, 4 mrad
α_B Transmit beam divergence, 5 mrad, only for calibration measurements.
α Atmospheric attenuation coefficient, including water vapor.

The expression in brackets involving α_T and α_B is the overlap factor of the laser beam and the telescope taking into account a geometric receiver. By equation 4-15, target reflectivity is given by the ratio of received to transmit power, taking into account constant geometric factors. The transmit power is related to the transmit detector voltage by equation 4-13 and the receive power is related to the receive detector voltage by equation 4-14. For the data of Figure 4-43, the atmospheric attenuation was assumed to be 1 dB over the 1200 m propagation path and the water vapor attenuation coefficients for the lines 9R30, 9P10, and 10P20 were taken as 2.8×10^{-5} m^{-1}Torr^{-1}, 3×10^{-5} m^{-1}Torr^{-1}, and 0.93×10^{-5} m^{-1}Torr^{-1}, respectively.[14] The ambient temperature and relative humidity were taken as 21 °C and 20%, respectively.

Sources of error

There are several sources of error in the above calibration method. These inlcude (1) the values of the attenuating filter as a function of wavelength, (2) errors in the transmission coefficients of other optical elements, (3) assumptions about the percentage of energy in the output spike for weak and strong lines, (4) assumptions about the laser beam divergence from line-to-line, (5) the atmospheric attenuation assumption, and (6) neglect of the average reduction

116

of target reflectivity due to movement in the wind. Perhaps the largest of these sources of error is in the measured value of $F_T(\lambda)$ for the particular filter used. Its nominal value is 0.6%, but the values as a function of wavelength can have uncertainties as high as 20%. The other transmission factors, $T_L(\lambda)$ and $T_W(\lambda)$, are probably correct to within 5%.

It was assumed that all lines had a divergence of 5 mrad. However, it was shown in laser testing that strong lines generally have higher divergence than weak ones. The error in divergence measurements could be as high as 20%. Referring to the reflectivity data of Figure 4-43 and reviewing the emission lines, it appears that the fourth and ninth lines would be strongest, with the largest divergence, and that these data points would then be underestimated.

Assumptions were made about the atmospheric attenuation coefficient. If an error had been made in that regard, it would have led to an underestimation of the data. In addition, the temperature and relative humidity were only estimated so that the resulting water vapor attenuation coefficient may be in error. However, this latter error would have affected only the first, third, and ninth data points.

The canvas target was observed to move a great deal in the wind. Therefore, the canvas would not be expected to appear as a single, normal incidence target as it was under calibration. Therefore, it would be expected that the net reflectivity resulting from the variable angles of incidence over the target surface would give rise to a net reduction in reflectivity.

Given the values for independent error noted above, it is estimated that the total error could approach 50% of the measured reflectivity. Considering that the data points are well within this margin, it can be stated that the sensor was well aligned and that all transmit and receive factors had been taken into account.

Sensor noise level

The sensor short term noise level was measured with the canvas target at a range of 600 m. The digital oscilloscope was used to record transmit and receive pulses for a pattern of ten wavelengths emitted at the standard 200 Hz repetition rate and with a burst rate of 1 Hz. As detailed in Section 4.1.6, the oscilloscope was capable of recording only the running average of a number of bursts; therefore, it was required to perform sequential experiments in order to accumulate data for the average transmit and receive intensities as a function of the number of pulses averaged. The elapsed time between such data sets was about 10 sec.

The results for a typical data set are shown in Fig. 4-47 where the average standard deviation is plotted against the number of pulses averaged for four representative lines. It can be seen that the noise level drops monotonically to about 1% with a 16 pulse average, after which no further reduction is achieved. The dotted line indicates a $1/N^{1/2}$ dependence.
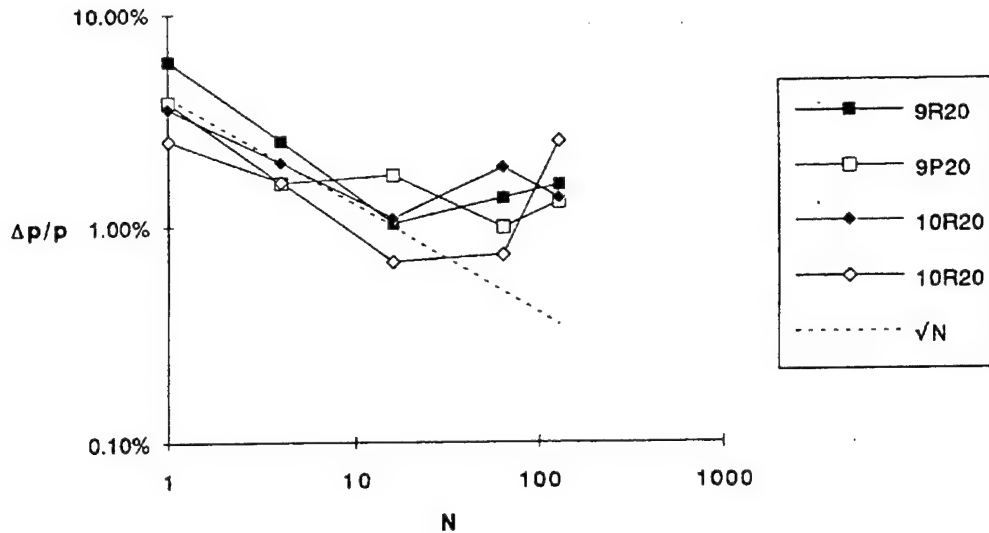
Figure 4-47. Sensor short term noise level.

4.2.2 Field Testing

The FAL sensor underwent three field trials at Dugway Proving Grounds, Utah over a period of four years (beginning in 1992) with each trial lasting approximately four weeks. The tests took place at a desert location with the weather sometimes varying from summer to winter conditions over the course of testing. The sensor was mounted in a van shown in Figure 4-48
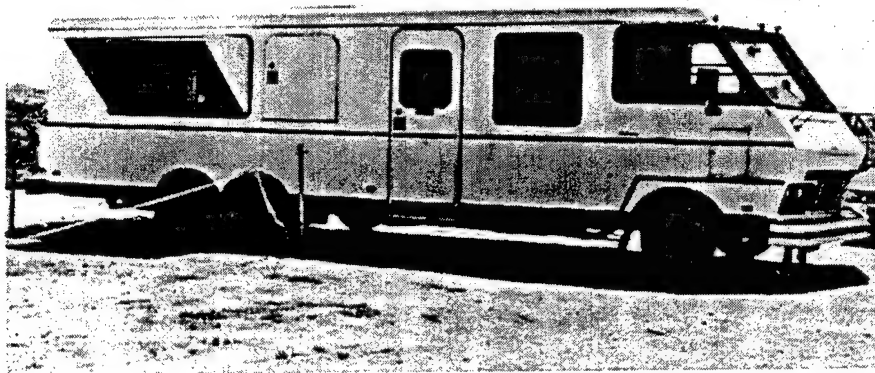

Figure 4-48. Field test van.

and was positioned just behind the open side window. Figure 4-49 shows two internal van views, (1) looking at the sensor and the side window and (2) looking from the sensor to the equipment rack. Ambient conditions within the van were controllable; but this control was not active at night, between test sessions, nor during transportation or storage.
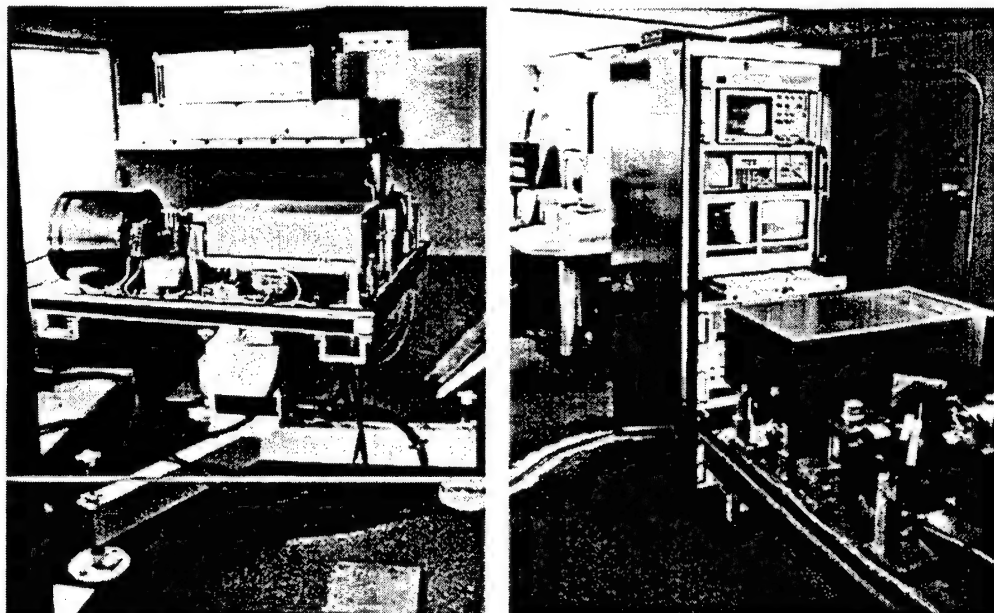
118

Figure 4-49. Sensor installation.

The daily test procedure included periodic measurement of solid target spectral reflectivity in the absence of chemicals and lidar measurement of atmospheric water vapor for comparison with local meteorological data. The target reflectivity measurements involved transmitting the standard burst mode of 16 lines at a burst rate of 1 Hz for about 10 min. In the case of water vapor measurement, a pattern of 16 wavelengths was transmitted which contained lines that matched the two major water absorption features in the 9 and 10 μm bands. The lines used for water vapor measurement were 9R12, 9R14*, 10R18, 10R20*, and 10R22, where the asterisk indicates the absorption peaks and all the other lines are at absorption minima. Three average values of water concentration were obtained by comparing 9R12 to 9R14*, 10R18 to 10R20*, and 10R20* to 10R22. Typically, values of water vapor content measured with the sensor were on the order of 5 mbar and were within 10% of values determined from meteorological data,

Tests were conducted with a vapor chamber and various solid targets shown in Figure 4-50. The vapor chamber had a 5 m x 5 m square aperture and the solid targets included sandblasted aluminum (shown), wood (not shown), and a dirt birm (not shown). The solid targets were typically located at a range of about 1 km; whereas, the chamber was located at a range of 400m with a solid target located 600m beyond, giving a propagation range of 1 km. At these ranges, it was required to use filters to reduce laser flux by about 40 dB in order to avoid detector saturation.

In one typical test, triethylene phosphate (TEP) was admitted into the chamber at 5 min intervals and in increasing quantities while the sensor fired through the chamber continuously. Typically, a test session would last 30 min with the sensor operating continuously at a 200 Hz repetition rate and 1-3 Hz burst rate. The absorption profile is shown for TEP in Figure 4-51(a) where the vertical lines indicate the laser wavelength pattern and the peak absorption coefficient is 10^{-3} m^2/mg. Typical data are shown in Figure 4-51(b) for lines that were chosen to coincide

119

with the maximum and minimum of the absorption profile. The data represents the ratio of receive to transmit pulse peak amplitude for an average of 100 bursts and the triangles signify the times of chemical injection. The absorption signature is clear in the 9P24 line and less so for 10R16. Based on the TEP concentration measured in the chamber with in situ diagnostics, it was determined that the sensor could detect concentration-path length product values of 30 mg/m^2 in the absence of algorithmic noise filters.
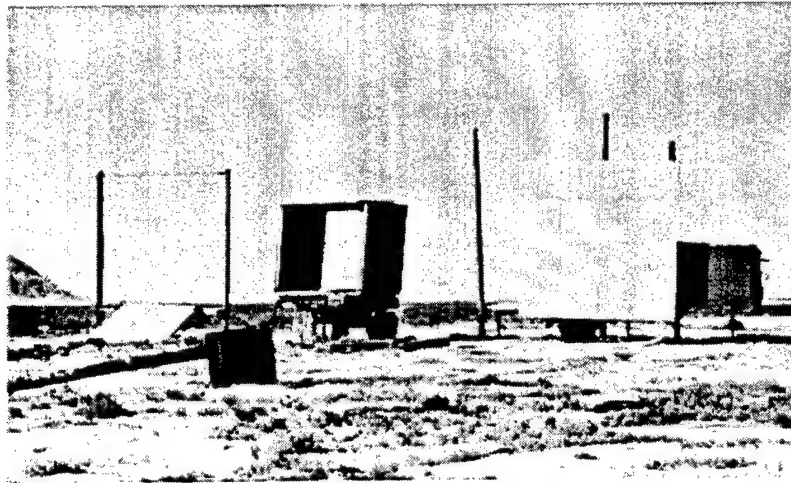

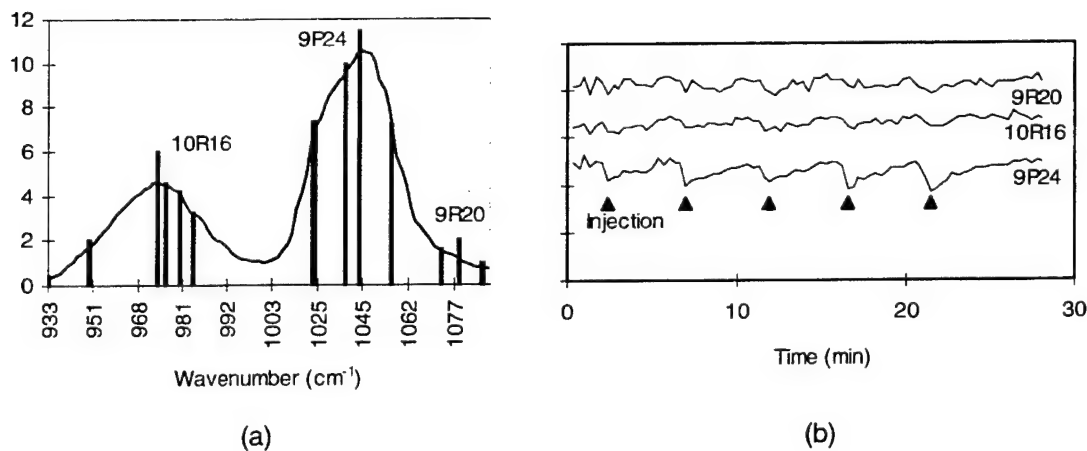Figure 4-50. Vapor chamber and solid target.

(a)

(b)

Figure 4-51. Typical absorption cell signatures.

A particulate dispenser was available for cloud generation as shown in Figure 4-52. In this case, the sensor was aligned with solid targets at a range of about 1 km and the cloud was carried by the wind across the line-of-sight. The sensor fired continuously through the cloud as it propagated and evolved. Typical results from data obtained with the digital oscilloscope are shown in Figure 4-53, where the return at a fixed wavelength is shown as a function of time after the dispenser started. The horizontal axis has been converted from time to range. At the start of the experiment ($\Delta t=0$) only the return from the solid target is clearly visible, although a very small return from the cloud leading edge can be discerned at a range of about 300 m. After an elapsed time of 33 sec, the return from the forming cloud at about 250 m is evident and the cloud has partially obscured the solid target. After another 13 sec interval, the cloud has completely

120

obscured the solid target and it is beginning to evolve into two sections as shown by the two-peaked return. In the next trace, the cloud is seen to form two distinct peaks and to begin dissipating, until it no longer obscures the return from the target in the last trace. Throughout the formation and dissipation phases, the data show that the cloud slowly drifts toward the sensor.

Figure 4-52. Dust dispenser .
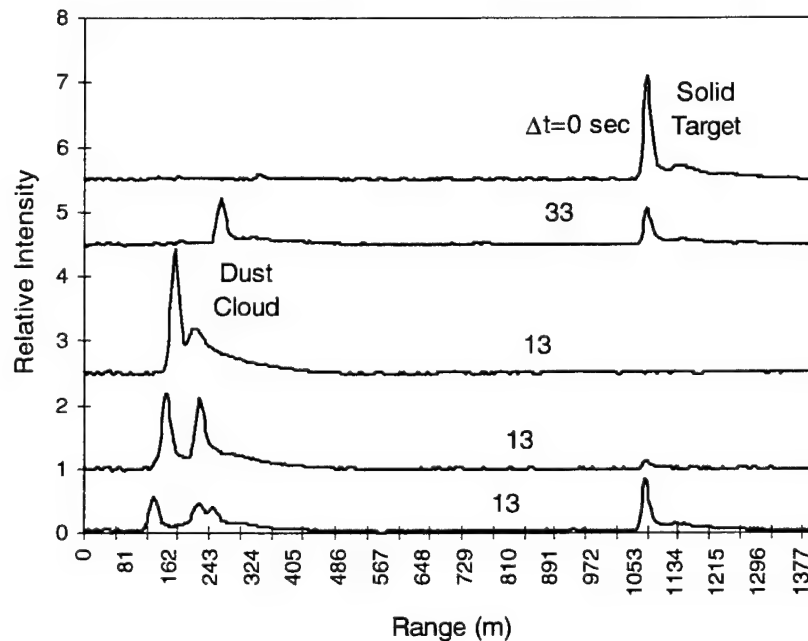
Figure 4-53. Cloud ranging test results.

A simple ranging test was performed by measuring the pulse returns from convenient topographic targets. In this case, the 9P18 line was used at a multimode energy level of 100 mJ (50 mJ in the spike) and only single pulse returns were used without any signal averaging or noise reduction. A typical oscilloscope trace is shown in Figure 4-54 for a pulse returned from a mountain at a range of 12 km. The return at 81 μsec has a single-pulse signal to noise ratio of about three. Extrapolation suggests that with averaging, ranging to 20 km would be possible.

Figure 4-54. Ranging pulse return.

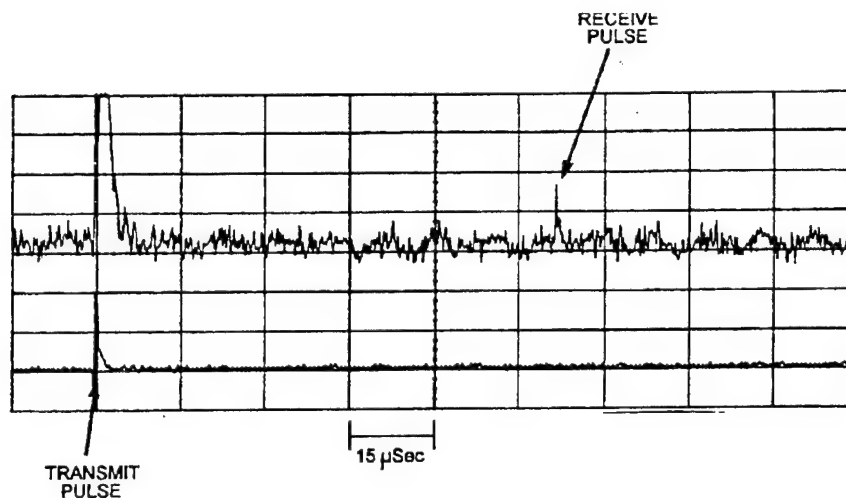As a result of the numerous field test events and sensor qualification tests at various ranges, the laser and sensor have shown several general characteristics with suggestions for improvement in some areas. First, the sensor has proven to be simple to set up. Even from a crated condition, it can take as little as two hours from uncrating through assembly and installation in the van to the point where data can be acquired. A very important contributing factor to this ease of use was the fact that no laser adjustment nor sensor optical realignment were required after transportation or storage.

It has been possible to achieve the low noise levels suggested by the results quoted above and with respect to the typical waveforms shown in Section 4.1.6 after a straightforward installation procedure. A number of power sources have been used with the sensor and occasionally modification of power cable routing has been required, but this has been easily accomplished.

Throughout the field events, the sensor has participated in 100% of the tests. Typically, a four week test period results in several million laser firings and collection of about 1 GB of data using the digital oscilloscope. With the digitizer card, the amount of data can increase to 5 GB. Although the number of data runs and the resulting amount of data can be prodigious, the sensor is easily operated by one person.

Several recommendations for improvement of the system have resulted from the field experience. The laser uses a high speed fan for cooling which produces high frequency noise. For this reason and others having to do with laser construction, water cooling is suggested. Furthermore, a reduction in the size and weight of the laser and sensor have been sought. Significant initial reductions can be achieved with modest effort having to do with removal of the laser total energy meter and spectrum analyzer to an auxiliary table and rearrangement of other components. In the area of functionality, certain software modifications have been recommended to further automate sensor setup and data acquisition. This will involve further integration of disparate pieces of code developed independently to operate the wavelength shifter, gimbal, and A-D card. Finally, sensor set up can be made more straightforward by redesigning the power and signal cable routing.

122

5. CONCLUSIONS

The results of laser testing detailed in Section 3.2 suggest that the present laser design is sound with respect to the program specifications. Most importantly, the goal of an integrated, compact and sealed transmitter has been realized. Design confidence has been achieved in the areas of optics, the optical bench, the wavelength shifter, the discharge module, the pulsed power section, the control electronics, the internal fan assembly, and the catalyst assembly. It was shown that critical optical alignment, including the wavelength shifter, could be maintained under the fairly aggressive environmental effects. In that regard, it is known that a 20 μrad shift in a resonator optic significantly reduces laser output energy; therefore, cavity alignment must be much better than this value judging by the stability of the laser output. Stability in the presence of environmental effects is also of great importance in the discharge module. Electrode misalignments of as little as 0.025 mm cause complete discharge collapse. The fact that the discharge stability did not suffer after the shock and vibration testing and during thermal cycling suggests that the design of this module is good. Also with respect to the discharge module, the key to long life operation is the elimination of high voltage breakdown through the preionizer dielectrics and across dielectric surfaces to the metallic walls in close proximity to the discharge. No failures of this type have been found in any of the three lasers and the original discharge modules have been used continuously without refurbishment.

The exception to complete success in the operational life test was failure of the output coupler and the Brewster windows due to laser flux damage. As detailed in Section 3.2, damage of the output coupler was eliminated in subsequent tests with an intracavity beam expander. It was also found in further testing that replacement of the ZnSe Brewster windows with NaCl greatly extended the life of the windows. However, use of this material introduced problems related to attachment because of material weakness and degradation of transmission due to hygroscopy. More work in this latter area is required.

The pulsed power section has been validated to a great extent in terms of operating characteristics for long runtimes. This includes the energy storage capacitors, thyratron switch, and high voltage potting technique. The important exception in this area is the high voltage power supply which transforms 28 Vdc to 25 kV in the command charge mode. This component was based on a unique design for FAL and experience with it has been mixed. It is clear that the design has merit because a single device operated for many millions of shots without incident. It is suspected that EMI effects and the lack of protection for the control circuit leads to failure of the input power transistors. The alternative of a somewhat larger, commercially available power supply operating from 208 Vac has proven to be very reliable.

The most important component for operation of a sealed, high repetition rate CO_2 laser is the catalyst. The FAL catalyst and its module appear to be proven under continuous operation and for long storage times. During the course of life testing, the laser was operated in a sealed condition, without gas replenishment for about one month with turn off at night and restart in the morning. Small leaks in each of the laser vessels, however, precluded long storage tests; but it was possible to keep a single vessel sealed and operable for six months during which laser

output characteristics were constant. It remains to test the laser under very long term storage conditions.

The results of sensor testing outlined in Section 4.2 show that its optical and detection characteristics are well established. This is based on the absolute reflectivity calibration measurements that were shown to be within experimental error and the measurements of short term noise. A percentage standard deviation noise level of 1-2% was measured after a 16 pulse average. This value of noise is within the state-of-the-art for such sensors. It was also found that the noise decreased as $1/N^{1/2}$ where N is the number of pulses averaged.

The success of the sensor in several field test events suggests that it is a very capable testbed device. Its design ruggedness and simplicity have meant that it is easy to set up and operate and that certain modifications dictated by changing experimental conditions are straightforward to make. The fact that the sensor can be transported to the field and maintain alignment throughout a four week test period has contributed greatly to the efficiency of the field campaigns. Nonetheless, modifications to the laser fire control and sensor data acquisition software could enhance its operation.

Throughout the numerous field tests with absorption cells and topographic targets a great deal of data has been taken. This data is being reduced by CBDC personnel and it is likely that additional comments about sensor capability can be made as a result. It was determined, however, in one field test that the FAL sensor was able to detect chemical concentrations roughly a factor of five lower than passive systems operating at the same time.

6. RECOMMENDATIONS

It has been documented in this report how the prototype laser was successful in meeting most of the program requirements. There were, however, operational shortcomings and insufficient testing in some areas. The laser did not meet the weight requirement, additional work is needed to develop a long life high voltage power supply, and further testing of materials suitable for Brewster windows is required. Finally, the critical area of catalyst shelf life requires further investigation.

A careful review of the laser component weights suggests that a significant decrease in laser weight to about 64 lb could be achieved with straightforward design changes including elimination of material, selective potting, and the use of lightweight alternative metals. These changes involve no technical risk and could be implemented through common design practices. Other studies have shown that more advanced modifications involving use of composite materials and advanced designs could reduce total weight to 30-40 lb. Such approaches would include redesigning the pressure vessel to serve as the optical bench, thereby eliminating the bench; use of stiff, lightweight composite materials for the pressure vessel and all structural members now made of aluminum; elimination of the Brewster window assemblies and hermetically sealing the intracavity beam expander and wavelength shifter with the pressure vessel; and general parts reduction by use of integrated modules. These advanced approaches involve technical risk and would require validation in laser functional and environmental testing before final implementation.

Laser high voltage power supply development is necessary if it is desired to operate only from a source of 28 Vdc. The present power supply has the correct functional characteristics, but it is not immune to the large EMI pulses generated by the laser discharge. Initial efforts to develop protection circuitry for the power supply controller have shown promise, but a great deal more has to be done before the power supply is qualified to the same operational lifetime level as the laser head. The alternative of a power supply operating from single phase 208 Vac or three phase, 40-400 Hz, 115 Vac may be suitable for many applications and it would seem that a 30% reduction in the size of commercially available units would be achievable.

In terms of operational lifetime of the laser head, the Brewster windows appear to be the major life-limiting component. Although NaCl windows have shown superior lifetimes compared to ZnSe, it has not been proven that NaCl windows will have a lifetime comparable to the rest of the laser head. NaCl windows also have serious drawbacks in that they are hygroscopic and fracture easily under sustained loads. These latter problems could be solved with a hermetically sealed and cushioned mount. Finally, other optical materials should be investigated, as for example KRS5 (thallium bromoiodide).

With respect to laser fabrication, It was found that the cross-flow, air-cooled heat exchanger could not be welded into the pressure vessel without vacuum leaks. A number of approaches to remedy the problem did not lead to a solution, except for the alternative of using a water-cooled heat exchanger that allowed for a different fabrication approach. This approach was

in fact used in the design and fabrication of the second generation FAL, but it was not assembled nor tested. These tasks need to be accomplished to verify the new, water-cooled design. Preliminary leak testing of the components have shown that they do not have vacuum leaks. Therefore, the second generation FAL would be the ideal device to test catalyst shelf life in a laser gas atmosphere with discharge. Finally, water cooling has the benefit of eliminating the noisy high speed cooling fan which was used in the air-cooled design.

The sensor was developed primarily as a testbed for demonstrating chemical detection in the field with the high repetition rate FAL transmitter. The design was guided by the need for easily modified components that presented low technical risk and the resulting sensor is therefore large. Reduction in the sensor size and weight, however, would be straightforward and significant reductions could be achieved with modest effort having to do with removal of the laser total energy meter and spectrum analyzer to an auxiliary table and rearrangement of other components. In the area of sensor functionality, certain software modifications have been recommended to further automate sensor setup and data acquisition. This would involve integration of disparate segments of code developed independently to operate the wavelength shifter, gimbal, and A-D card. Finally, sensor set up can be made more straightforward by redesigning the power and signal cable routing.

One component that has been at the center of discussions related to improving sensor functionality is the wavelength shifter. The issue is that due to the pseudo-resonant nature of the galvanometer, the laser repetition rates and burst rates are limited. In addition it is not possible to switch laser wavelength patterns on a burst-to-burst basis which is highly desirable with rapidly developing clouds. There are further problems related to the fact that the shifter performs the function of synchronizing the laser fire commands with wavelength selection. The result is that the shifter performs all timing functions for the laser and sensor, and the data acquisition software is slaved to it through the necessary trigger signals. It is desired to reverse the direction of the trigger pulses so that the system computer controls all functions. In order to solve these problems of wavelength shifter functionality, it would be necessary to develop a wavelength shifter using a non-resonant galvanometer. Such a system would provide truly random access to the spectral lines and at any firing rate on a pulse-to-pulse basis.

REFERENCES

1. Developed under a joint program with Laser Drive, Inc., Gibsonia, PA 15044. Partially funded by a Hughes Research and Development program.

2. Applied Laser Electronics, Inc., rack-mounted Model 302 and compact Model 152.

3. Ceramic capacitors supplied by TDK, Inc.

4. Thyratron CX1640 supplied by English Electric Valve, Inc. Crossatron supplied by Hughes Research Laboratories, Malibu, CA.

5. G. Hoflund, University of Florida and Hughes Technology Support Division, private communications.

6. Jean Claude Farcy, Societe de Telecommunications, France, private communication.

7. Wavelength selector supplied by Three Sigma, Inc. Gardnerville, NV.

8. Catalyst supplied by Phillips Petroleum, Bartlesville, OK. Alternative catalyst provided by T.P. Moser, Hughes Technology Support Division.

9. A.L.S. Smith, J.P. Sephton, and G. Scott, J. Phys E: Sci. Instrum. 17, 590, 1984.

10. T.P. Moser, Second International Conference on Low-Temperature CO-Oxidation Catalysts for Long-Life CO_2 Lasers, Langley Research Center, Hampton VA, NASA Conference Bulletin 3076, 1990.

11. D.S. Stark and M.R. Harris, J. Phys. E: Sci. Instrum. 16, 492, 1983.

12. Gimbal supplied by Rotating Precision Mechanisms, Inc., San Fernando, CA. 91324.

13. R.M. Schotland, J. Appl. Meteor. 13, 71, 1974.

14. W.B. Grant, Appl. Opt., 29, 451, 1990.